Analysis of Handling Stresses and Breakage of Thin Crystalline Silicon Wafers

A Thesis
Presented to
The Academic Faculty

by

Xavier F. Brun

In Partial Fulfillment
of the Requirements for the Degree
Doctor of Philosophy

George W. Woodruff School of Mechanical Engineering
Georgia Institute of Technology
December 2008

Analysis of Handling Stresses and Breakage of
Thin Crystalline Silicon Wafers

Approved by:

Dr. Shreyes N. Melkote, Advisor
School of Mechanical Engineering
Georgia Institute of Technology

Dr. W. Steven Johnson
School of Material Science and Engineering
Georgia Institute of Technology

Dr. Steven Danyluk
School of Mechanical Engineering
Georgia Institute of Technology

Dr. Paul M. Griffin
School of Industrial and Systems Engineering
Georgia Institute of Technology

Dr. Suresh K. Sitaraman
School of Mechanical Engineering
Georgia Institute of Technology

Dr. Juris Kalejs
American Solar Technologies

Date Approved: August 27, 2008

ACKNOWLEDGEMENTS

I would like to express my sincere gratitude to my advisor, Prof. S. N. Melkote for his mentorship, support, and encouragement throughout the course of my study here at Georgia Tech. I would like to extend my gratitude to Prof. S. Danyluk, Prof. P. Griffin, Prof. S. Johnson, Prof. S. Sitaraman, and Dr. J. Kalejs for serving on my committee and providing invaluable suggestions and recommendations.

My special thanks go to Ms. Theresa Keita, Ms. Glenda Johnson and Ms. Cosetta Williams at the Mechanical Engineering Department, and, Ms. Siri Melkote, Ms. Pam Rountree and Ms. Lisa Teasley in the Maufacturing Research Center. I would like also to thank Mr. Steven Sheffield, for training me on several machines and Mr. John Graham, for running a great machine shop.

My Special appreciation is extended to the National Renewable Energy Lab for their interest and support of this work, and to Manz Automation, OTB Solar and Schott Solar for their supply of equipment and materials.

I would like to acknowledge the input and help I received from my fellow co-workers in Prof. Melkote's group during this research work. They are Matt Breland, Vincent Dessoly, Haiyan Deng, Chris Golden, Sangil Han, Wu Hao, Rick Kalil, Mukund Kumar, Martin Kurnadi, Tommy Newton, Chee Keong Ng, Ramesh Singh, Sathyan Subbiah. In addition, I would like to thank Victoria Garcia, Fang Li and Joel Neff for their valuable discussions and inputs during the PV meetings. Special thanks to Lambros Samouris for helping me build my experimental setup.

Special thanks to Mukund and Ramesh for providing assistance with my thesis work in addition to being always willing to go for coffee or enjoying nice food. I would like to specially thank Umang Dua, Rebecca Li and Xavier Paglia for being great friends, the years spent at Riverbend would have never been the same without them. I would also like to thank my friends, Jacques and Michele Alain, Mahsa Allandet, Johanna Fernández de la Cruz, Hiromi Kondo, Emi Tajiri, and many more. They helped me sail smoothly through my graduate life in Atlanta and learn more about myself.

And finally, I am indebted to my family, my father Bernard Brun, mother Anne-Marie, brother Laurent and my sister Estelle. I would like to dedicate this thesis to them for their love, support, and encouragement throughout my Ph.D study.

TABLE OF CONTENTS

LIST OF TABLES

LIST OF FIGURES

LIST OF SYMBOLS

a_{st}	Direction cosine
A	Zener elastic-anisotropy index
c_p	Heat capacity at constant pressure, J/kg/K
c_{ij}	Independent cubic-symmetry elastic-stiffness coefficients
$C_{\varepsilon i}$	Convection term in the RSTE
$C_{\varepsilon i}$	Coefficient in the turbulent dissipation rate equation
C_{ijkl}	Elastic stiffness tensor
D_{ij}^{L}	Molecular diffusion term in the RSTE
D_{ij}^{T}	Turbulent diffusion term in the RSTE
E	Total energy, J
F	Lifting force, N
F_{ij}	Production by system rotation term in the RSTE
G_{ij}	Buoyancy production term in the RSTE
h_c	Cone mill height, mm
h_n	Nozzle height, mm
H	Stand-off distance, mm
K_c	Fracture toughness, Mpa.m$^{0.5}$
l	Crack length, mm
l_c	Critical crack length, mm

M	Mass flow rate, g/s
M_t	Turbulent Mach number
M_w	Molecular weight, kg/kgmol
n	Number of nodes
N	Number of cells
N_f	Number of cells per flow passage
p	Pressure, Pa
p_{op}	Operating pressure, Pa
P_{ij}	Stress production term in the RSTE
Pr_t	Prandtl number
r, z	Radial, transverse coordinates
r_i	Inlet radius, mm
r_n	Nozzle radius, mm
r_o	Oultet radius, mm
R	Universal gas constant, R =8.31447x103 J/kgmol-K
R_i	Rotation boundary condition around *i* axis
S_h	Heat source term, J.kg/m^3/s
S_{ijkl}	Elastic compliance tensor
T	Temperature, K
u_i	Velocity magnitude, m/s
u_i'	Fluctuating velocity component, m/s

$\overline{u_i' u_j'}$	Reynolds stresses, $(m/s)^2$
U_i	Displacement boundary condition along *i* axis
V	Volumetric flow rate, l/min
w	Specimen width, mm
Y	Shape factor

LIST OF ABBREVIATIONS

CFD	Computational Fluid Dynamics
Cz	Czochralski
EFG	Edge-defined Film-fed Growth
FE	Finite Element
IC	Integrated Circuit
LES	Large Eddy Simulation
mc-Si	multi-crystalline Silicon
PV	Photovoltaic
RANS	Reynolds Average Navier-Stokes
RSTE	Reynolds Stress Transport Equations
sc-Si	single crystal Silicon

SUMMARY

Photovoltaic manufacturing (PV) is material intensive with the cost of crystalline silicon wafer, used as the substrate, representing 40% to 60% of the solar cell cost. Consequently, there is a growing trend to reduce the silicon (Si) wafer thickness and to increase wafer size leading to new technical challenges related to manufacturing. Specifically, the breakage of thin Si wafers during handling and/or transfer is a significant issue. Therefore improved methods for breakage-free handling of thin and large Si wafers are needed to address this problem.

An important pre-requisite for realizing such methods is the need for fundamental understanding of the effect of handling device variables on the deformation, stresses, and fracture of mono- and multi- crystalline silicon wafers. This knowledge is lacking for thin wafer handling devices including the Bernoulli gripper, which is an air flow nozzle based device.

In this thesis, a computational fluid dynamics (CFD) model of the air flow generated by a Bernoulli gripper has been developed. This model predicts the air flow, pressure distribution and lifting force generated by the gripper. The model is experimentally verified for a rigid substrate through measurements of the air pressure distribution. For thin PV Si wafers (e.g. EFG and Cast silicon), the CFD model is combined with a finite element model (FE) of the wafer to analyze the effects of wafer flexibility on the equilibrium pressure distribution, lifting force and handling stresses. This model is also experimentally verified and shown to yield good results. Specifically, the effect of wafer flexibility on the air pressure distribution is found to be increasingly

significant at higher air flow rates. The model also yields considerable insight into the relative effects of air flow induced vacuum and the direct impingement of air on the wafer on the air pressure distribution, lifting force, and handling stress. The latter effect is found to be especially significant when the wafer deformation is large such as for the thin EFG wafer studied. In addition to silicon wafers, the model can also be used to determine the lifting force and handling stress produced in other flexible materials.

Finally, a systematic approach for the analysis of the total stress state (handling plus residual stresses) produced in crystalline Si wafers and its impact on wafer breakage during handling is presented. Results confirm the capability of the approach to predict wafer breakage during handling given the crack size, location and fracture toughness. This methodology is general and can be applied to other thin wafer handling devices besides the Bernoulli gripper.

CHAPTER I

INTRODUCTION

1.1 Photovoltaic Manufacturing

The crystalline silicon based photovoltaic (PV) solar cell manufacturing industry is experiencing rapid growth due to greater emphasis on the development of renewable energy sources. Of the available PV technologies, single- and multi-crystalline silicon based solar cells make up over 80% of the commercial solar cells produced today [1]. Since the cost of silicon wafer can represent as high as 50% of the solar cell cost [2], PV manufacturers are actively pursuing the development of solar cells made of thinner (less than 200 μm) and larger (up to 210 mm x 210 mm) crystalline silicon wafers [3]. Efforts to decrease wafer thickness from the current values of ~200 μm are aimed at reducing material costs while the increase in wafer size from ~125 mm x 125 mm to 210 mm x 210 mm targets reduction in solar panel/array assembly costs. However, given the inherent brittleness of silicon, reduction in wafer thickness has been found to significantly increase wafer/cell breakage rates, especially in the robotic handling and transfer steps used in solar cell processing, thereby significantly lowering solar cell yield and increasing material and manufacturing costs [4]. Figure 1.1 shows published data for the breakage rate of laser grooved buried grid solar cells as the wafer thickness is reduced from 270 μm to 250 μm [4]. Note that for proprietary reasons the units of the vertical axis are not specified. Analysis of the data shows that the fraction of cells that break during wafer/cell handling and/or transfer is approximately 26.6% and 28.9% for the 270 μm and 250 μm thick wafers, respectively. Assuming a 96% yield for the 270 μm wafer and

assuming conservatively that the breakage rate for each operation increases linearly with decrease in wafer thickness; the predicted yield for 150 μm thick wafers is ~73.6%. This is not an unreasonable number for very thin silicon wafers. The predicted fraction of breakage associated with wafer transfer/handling of 150 μm wafers is ~29.8%.

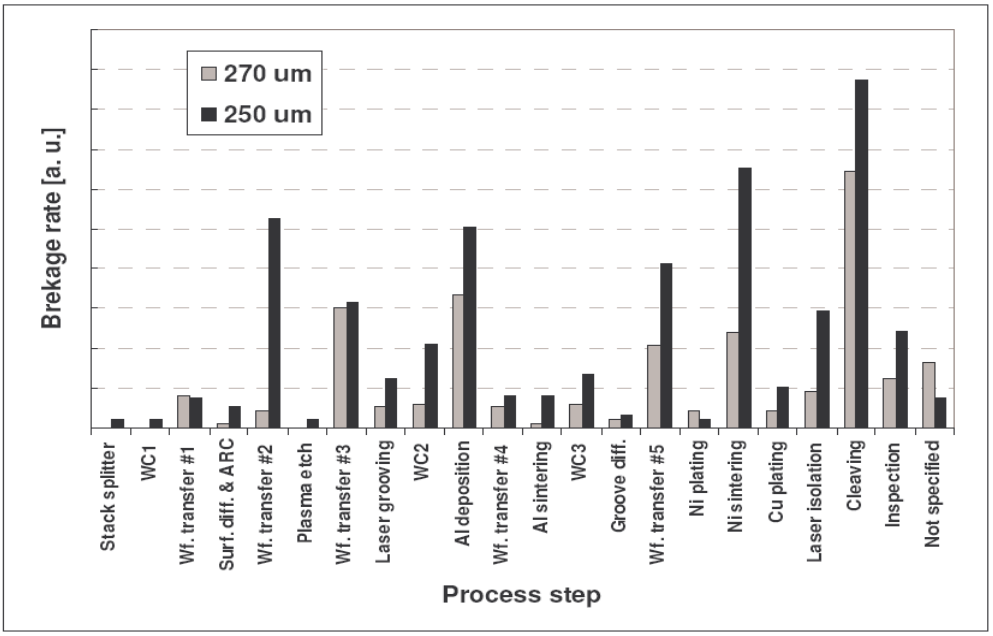

Figure 1.1: Breakage rate data for laser-grooved buried grid solar Cast Si solar cells [4]

Although considerable work has been done in the Integrated Circuit (IC) industry on handling silicon wafers, practical use of IC handling techniques is limited in the PV industry because of their different requirements [5]. For instance, IC production deals almost exclusively with *single crystal silicon* (sc-Si) wafers of starting thickness typically in the 600-800 μm range whereas majority of crystalline silicon solar cells are made from *significantly thinner* (≤ 220 μm) *multi-crystalline silicon* (mc-Si) wafers. In addition, PV

manufacturing is material intensive as opposed to IC fabrication, which is process intensive thus driving the need for low-cost and high volume handling methods. Therefore, improved methods for breakage-free handling of thin and large silicon wafers are needed to address this problem.

1.2 Limitations

An important pre-requisite for the development of breakage-free handling methods is the need for improved fundamental understanding of the causes of wafer breakage during thin wafer handling and/or transport. This requires knowledge of the stress distribution produced in different types, thicknesses and sizes of PV silicon wafers as a function of the handling device variables and a systematic methodology to evaluate and analyze them relative to structural defects such as cracks present in the wafers. A systematic scientifically-based investigation of these issues is lacking today for wafer handling methods commonly used in the PV industry. These methods include Bernoulli gripping - a pneumatic gripping method - that is commonly used. The Bernoulli gripper consists of an air flow nozzle shown schematically in Figure 1.2. In this device, a lifting force is created between the gripper face and the wafer by a radially-diverging decelerating air flow, which produces a low pressure region or partial vacuum between the gripper and the wafer. In the geometry shown in Figure 1.2, the wafer weight is balanced by the lifting force.

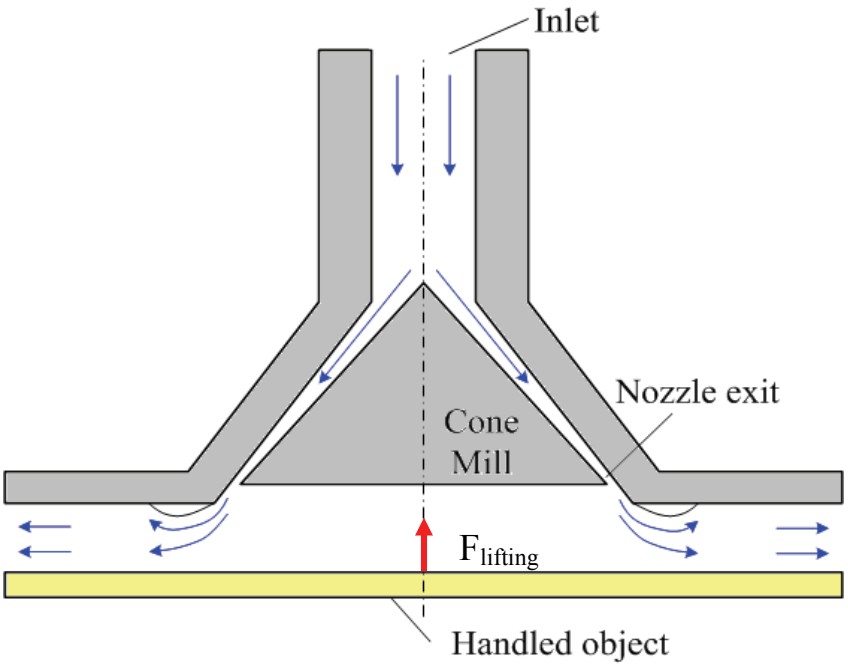

Figure 1.2: Schematic of a Bernoulli gripper

While Bernoulli grippers are widely used in handling silicon wafers and solar cells, their mechanics are not well understood, particularly for handling thin crystalline silicon wafers (< 200 μm) that are inherently flexible. Consequently, ad-hoc methods are often used in practice to adjust the control variables of the gripper to prevent wafer breakage. When handling a very thin wafer, the suction force deforms the wafer significantly and generates stresses in it. These stresses along with pre-existing residual stresses in the wafer due to crystal growth and wafering (laser cutting/wire sawing) processes can lead to wafer fracture. In this context, a clear understanding of the effects of Bernoulli gripping variables on thin mono- and multi- crystalline silicon wafer deformation, stresses, and breakage is lacking. In addition, a systematic and model-based approach for guiding the selection of thin wafer gripping/handling parameters is also not available.

1.3 Research Questions and Objectives

In light of the aforementioned limitations in the knowledge pertaining to handling-induced wafer breakage in PV manufacturing, the following specific research questions are addressed in this thesis:

- What is the distribution of stress produced in different types of thin crystalline silicon wafers during automated handling and how can it be determined?
- What are the effects of wafer handling device variables on the deformation and stress produced in thin crystalline silicon wafers?
- Can wafer breakage due to handling stresses be predicted and if so how?

These research questions are answered in this thesis through modeling, analysis and experimentation with a focus on Bernoulli gripping of different types and thicknesses of crystalline silicon wafers used in solar cell manufacture.

The specific research objectives formulated to address the research questions posed above are as follows:

- Develop and experimentally verify a computational fluid dynamic (CFD) model of the air flow generated by a Bernoulli handling device when handling a rigid thick substrate.
- Develop and experimentally verify an iterative fluid-structure interaction model of the Bernoulli *thin wafer* gripping process that accounts for the effects of wafer deformation on the lifting force and stress state produced in the wafer.

- Experimentally investigate the effects of wafer characteristics (type, thickness, size) and Bernoulli gripper variables on the deformation and total stress state produced in thin crystalline PV silicon wafers.
- Develop and verify a method to predict wafer breakage/fracture from the total stress state produced in the wafer during Bernoulli handling.

Realization of these research objectives will enable solar cell manufacturers to optimize their wafer handling methods to minimize wafer/cell breakage and associated material and manufacturing costs when using thinner (< 200 μm) wafers. In addition, this research will provide modeling tools for the optimization of the Bernoulli gripper design itself.

Although the results discussed in the thesis are specific to Bernoulli gripping, the methodology and basic understanding of the factors influencing the breakage of thin silicon wafers during handling are general and applicable to other handling devices that induce deformation and stresses in the wafers, e.g. low pressure grippers.

1.4 Thesis Outline

This thesis is divided into six main chapters including introduction. Chapter 2 reviews prior work that is relevant to the thesis topic and identifies its key contributions and limitations. Chapters 3 through 5 contain the main contributions of this thesis and are summarized in the flowchart shown in Figure 1.3.

Chapter 3 presents the modeling and prediction of the air flow, radial air pressure distribution and lifting force produced by a non-contact Bernoulli gripper on a rigid substrate. A Reynolds stress model is implemented in a finite volume based segregated

Reynolds-Averaged Navier-Stokes computational fluid dynamics (CFD) solver. In addition, an experimental set up is designed to validate the predicted pressure distribution acting on a rigid substrate.

Chapter 4 presents an iterative procedure that combines the CFD model of Bernoulli gripping developed in Chapter 3 with a non-linear finite element model of the thin silicon wafer to analyze the effect of wafer flexibility on the equilibrium wafer deformation, radial air pressure distribution and handling force. The distribution and magnitude of the handling stresses produced in two types of thin mc-Si PV wafers are also obtained and analyzed. The iterative approach is experimentally validated by comparing measured and predicted wafer deformation profiles.

Chapter 5 presents a systematic approach to breakage analysis of crystalline silicon wafers during handling via analysis of the total stress state produced in the wafer. The total stress state is determined using a combination of wafer deformation measurements and non-linear finite element analysis. In addition, knowledge of the total stress state combined with the crack size and location enables determination of wafer breakage and the associated fracture stress. The use of linear elastic fracture mechanics to predict wafer breakage during Bernoulli handling is experimentally verified through wafer breakage tests. In addition, critical crack lengths that can lead to wafer fracture are also identified.

Finally, the main conclusions of this thesis are drawn in Chapter 6 and suggestions for future work are given.

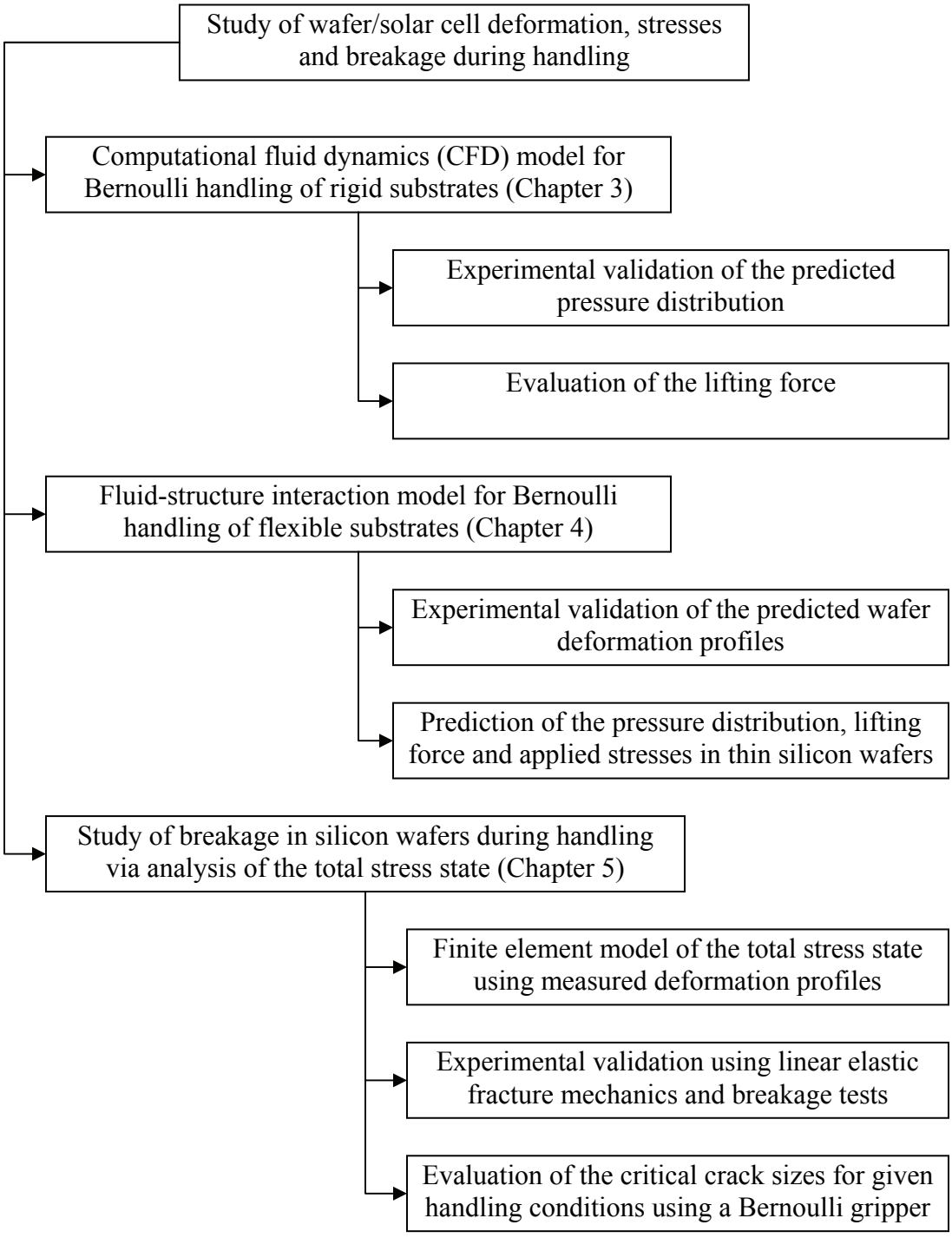

Figure 1.3: Flowchart of the key thesis topics

CHAPTER II

LITERATURE REVIEW

Automated handling of non-rigid parts is a challenging field of industrial automation. Research has been quite exhaustive in the development of handling devices for addressing the handling of compliant materials, especially for limp sheets such as fabrics [6-11]. Different gripping principles can be used to handle non-rigid materials as shown in Figure 2.1. Although silicon wafers were initially considered to be rigid, with the reduction in wafer thickness this assumption needs to be reconsidered for gripper design and operation. Handling needs to be more precisely controlled to avoid wafer breakage. Hence, this section reviews past work in the relevant areas of wafer handling, specifically those related to the Bernoulli gripper and finally the different silicon wafer types and their mechanical properties.

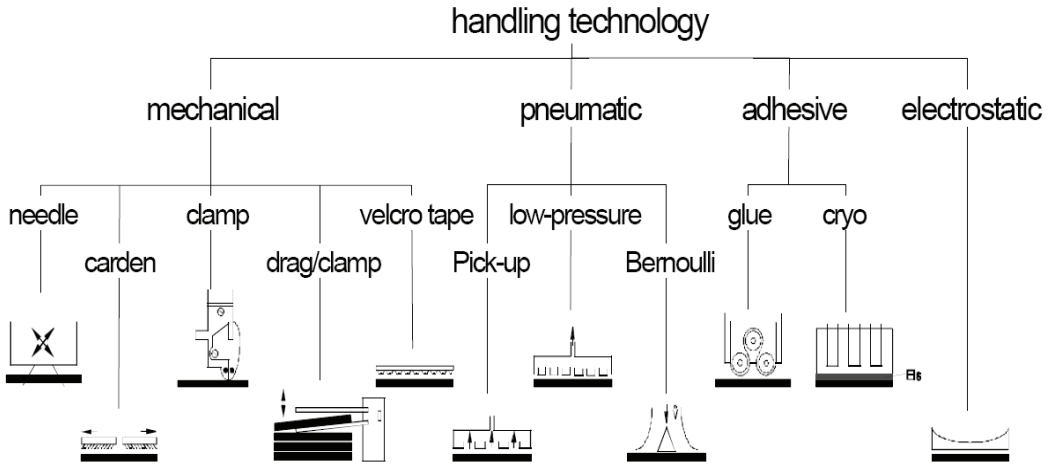

Figure 2.1: Technological principles for handling of non-rigid materials [9]

2.1 Wafer Handling

Wafer handling was investigated first in the semiconductor (IC) industry particularly with the use of air bearings or air tracks to handle silicon wafers in the 1970's [12-16]. These devices were developed to limit the contamination of the wafer by any contacting surface. In the 1980's, an extension of the air track idea to robotic grippers was developed in [17-19]. In 1993, Tokisue and Inoue [20] designed and tested several handling devices: a non-contact handler (or Bernoulli gripper), a non-contact gas levitation track, a liquid levitation track for wet processes and finally an electrostatic chuck. Extensive work has been done on electrostatic grippers for wafer handling from 1993 to 2000 [21-23]. Since then, with reduction in wafer thickness, automated handling was faced with new challenges [24] and novel technologies such as electrostatic grippers and bonding techniques were developed to address these challenges. Bonding techniques simplify the handling of thin silicon wafers by temporarily increasing the thickness with the use of a thicker substrate or carrier [25-30]. Finally, a simultaneous vacuum-Bernoulli gripper was developed in allowing the handling of very thin wafers (100 μm minimum thickness for 200 mm round wafers) and avoiding the use of tape/bonding [31, 32]. However, key differences between PV and IC applications limit the usefulness of the aforementioned techniques, particularly electrostatic grippers and bonding methods, in solar cell production.

For instance, IC production deals almost exclusively with round single crystal silicon wafers of starting thickness in the ~600-800 μm range whereas majority of crystalline silicon solar cells are made from significantly thinner (≤ 200~250 μm) multi-

crystalline silicon square wafers or single crystal pseudo-square Czochralski (Cz) wafers. Very thin wafers tend to bow easily during certain process steps (e.g. metallization) and are prone to failure when held in electrostatic chucks or vacuum gripper in the bowed state [31]. Additionally, the high cost of electrostatic chucks cannot be justified in solar cell production. Certain types of mc-Si wafers used in solar cell manufacture (e.g. Edge-defined Film Growth or EFG) are quite non-uniform in thickness and are therefore not well-suited for handling by the wafer-to-substrate bonding method. Further, the bonding method is an expensive solution for the solar industry because of the need for one carrier per solar cell and the added cost of a de-bonding step. For these reasons, wafer handling methods used in the IC industry are not prevalent in solar cell manufacture.

2.2 Radially Diverging Outflow Air Nozzle or Bernoulli Gripper

Bernoulli gripper or radial air outflow nozzle was first patented and certified in 1969 for lifting rigid circular semiconductor wafers [33, 34]. In this handling device, an axially directed air flow is diverged in the radial direction under proper flow and design conditions, creating a low pressure (vacuum) region between the gripper surface and the planar object (see Figure 2.1). This technique enables automated handling of many types of materials ranging from silicon wafers to woven fabrics. In the 1980s, Paivanas and Hassan [12, 17] extensively studied radially diverging air flow for contactless handling of *rigid* semiconductors wafers. Modifications of the initial design included the use of an end mill cone to avoid direct impingement of the wafer surface by the radial air flow [35]. Grutzeck and Kiesewetter [36] analyzed the use of the Bernoulli effect in micro-part handling. Erzincanli et al. [37, 38] extended the use of the Bernoulli gripper to other non-

rigid materials such as food. Ozcelik et al. [8, 9, 39] did experimental work on handling woven fabrics and other materials using this type of non-contact end-effector.

To the best of the author's knowledge, analysis of applied stresses and relating it to wafer breakage during a handling step has not been studied in the literature thus far. Prediction of wafer breakage for a specified set of handling control parameters is also not available. In addition, the influence of flexibility of the handled object on the flow, pressure distribution and lifting force produced by a Bernoulli gripper has not been reported.

2.3 Mechanical Properties of Silicon Wafers

The majority of commercial solar cells are made from crystalline silicon. Either mono- or multi-crystalline silicon is used in the manufacture of solar cells. Multicrystalline silicon is grown by either ingot (cast wafers) or ribbon (e.g. Edge-defined Film-fed Growth or EFG wafers) techniques leading to different material properties [2]. Figure 2.2 shows a schematic of the EFG growth process. In this case, wafers are laser cut from the tube; such cutting process usually induces cracks at the edges of the wafer, requiring some etching to reduce the laser cutting damage.

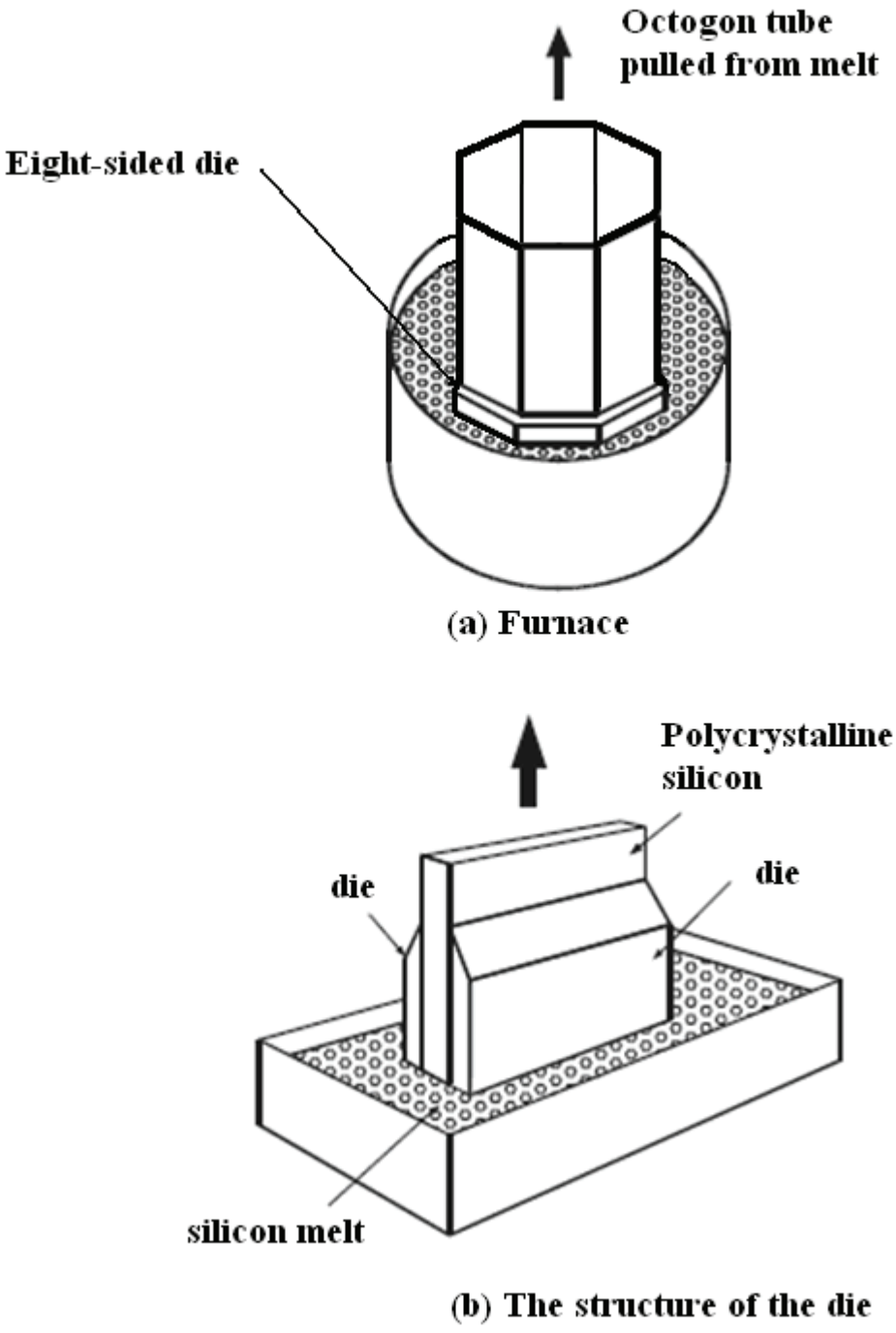

Figure 2.2: Schematic of EFG growth process (edited from [40])

2.3.1 Fracture Strength of Silicon Wafer

At room temperature, silicon is a brittle material. When the applied stress exceeds a critical level (the fracture strength), breakage will occur [41]. The critical stress level depends on the size of cracks or defects present in the silicon. When using small wafers compared to full size wafers, larger wafer strengths are obtained since the probability of encountering a large defect in a small area is reduced [42]. In [43, 44], strengths in the range of 2-4 GPa for small plates (around 5 mm in diameter) of single crystal polished Si wafers have been measured using a ball-on-ring device. On the contrary, tests on full size polished single-crystal silicon revealed smaller strengths on the order of 120 MPa using a ring-on-ring test [45]. As wafers were thinned from as-sawn to etched and finally polished wafers, the fracture strength increased since the depth of damage was reduced [45]. A similar trend was noticed from biaxial flexure tests on small (111) Si wafers. An observed increase in the depth of damage led to a decrease in the fracture strength [46]. In all cases the Weibull statistical theory [47] is used to determine the probability of wafer failure at a given stress level. The influence of the thickness on failure stress was experimentally studied on small dies [48]. It was found that for thickness above a critical value, a decrease in thickness led to an increase in the failure stress. The trend was reversed for thicknesses below the critical value.

In the PV industry, considerable variation in fracture strength as a function of manufacturing process steps was found for Gallium Arsenide (GaAs) substrates [49]. Different bending tests have been reported to measure the fracture strength of silicon wafers and are summarized in Table 2.1. The resulting fracture strength is seen to vary significantly. Note that the cast wafers are wire-sawn while EFG wafers are laser cut.

Table 2.1: Fracture strength of m_c-Si wafers

Type	Size (mm)	Thickness (μm)	Surface	σ_{max} (MPa)	Method	Ref.
Cast m_c-Si	100x100 mm	330	As-sawn	83	Biaxial	[50]
Cast m_c-Si	100x100 mm	310	Etch 10μm/side	234	Biaxial	[50]
Cast m_c-Si	100x100 mm	290	Etch 20μm/side	299	Biaxial	[50]
Cast m_c-Si	100x100 mm	290	Etch 20μm/side	520	Biaxial	[50]
Cast m_c-Si	100x100 mm	290	Etch 20μm/side	363	Biaxial	[50]
Cast m_c-Si	125x125 mm	195	As-sawn	560	Ring-on-ring	[51]
Cast m_c-Si	125x125 mm	168	Saw damage etch	1500	Ring-on-ring	[51]
Cast m_c-Si	125x125 mm	147	Polish etch	2400	Ring-on-ring	[51]
Cast m_c-Si	156x156 mm	Unspecified	As-sawn	120	4 point bending	[52]
EFG m_c-Si	100x100 mm	330	As-cut	404	Biaxial	[50]
EFG m_c-Si	100x100 mm	Unspecified	As-cut	50	Twist test	[53]

In determining the wafer strength, the distribution of applied stresses, the distribution of residual stresses and the location of flaws will influence the fracture stress. The applied stress distribution for the twist test was evaluated using Finite Element (FE) simulations by Chao et al. [53]. When modeling thin wafers they found that geometric non-linearities were significant and needed to be accounted for in the simulations. Behnken et al. [54] reported on the applied stress distributions produced in different bending tests. . It is often assumed that wafers break at the location of the maximum tensile stress [2]. To avoid such an assumption, Sun et al. [55] considered the uniformity

of the stress field in the defect region in order to optimally select the test configuration. For example, a ground die sample resulted in randomly distributed flaws on the surface. The test configuration that generates a uniform stress field on the largest area of the tensile surface will be best since the location of the flaws is not known a priori. Finally, edge cracks and surface cracks can be separated using both ring-on-ring and four point bending tests [56] or using a ball-on-edge test [57].

In light of the above work, it is evident that there is a significant variation in the fracture strength of the m_c-silicon wafers reported in the literature. Fracture strength being too dependent on the wafer type and structural defects, Weibull statistics are usually required to evaluate wafer breakage.

2.3.2 Breakage of Silicon Wafers

Fundamentally, breakage of Si wafers during processing or handling is due to the propagation of cracks present in the wafer. Knowledge of crack locations and sizes is therefore needed to predict wafer breakage. A few techniques have been developed to detect and quantify cracks in wafers [58-60]. A crack will propagate if a sufficiently large in-plane tensile stress is applied normal to the crack plane (assuming Mode I fracture). Thus, it is necessary to analyze the nature, magnitude and distribution of the total stress state generated in the wafer/cell during handling or processing. This includes the residual stress generated in a prior process step and stresses applied to the wafer/cell by the current process, and handling and/or transport methods used in solar cell manufacture.

Different techniques can be used to evaluate the residual stresses present in the wafer. Of particular interest to the PV industry, non-destructive full-field techniques have been developed such as Shadow-Moiré [61] and near-infrared polariscope [40]. For the

Shadow-Moiré technique, the residual stresses are extracted from the out-of-plane deformation profile obtained after applying a concentrated load to the sample. The influence of the in-plane residual stress is captured by the measured out-of-plane deformation. This approach being not sensitive to local stress concentrations a near-infrared polariscope technique was developed by He [40]. This technique measures the change in the polarization state of the transmitted light and allows characterization of the full-field through-thickness residual in-plane shear stress but not the complete residual stress state in the wafer. Hence, it is not yet possible to superpose the residual stresses on the handling stresses to evaluate the total stress state generated in the wafer for wafer breakage prediction.

2.3.3 Elastic Properties of Silicon Wafers

The generalized Hooke's law gives the relationship between the stress and strain tensors as:

$$\sigma_{ij} = C_{ijkl}\,\varepsilon_{kl} \qquad (i,j,k,l = x,y,z) \tag{2.1}$$

where x, y, z is an arbitrary rectangular coordinate system, C_{ijkl} is the tensor of elastic coefficients (also called elastic stiffness tensor). The Hooke's law can also be written as:

$$\varepsilon_{ij} = S_{ijkl}\,\sigma_{kl} \tag{2.2}$$

where S_{ijkl} is the compliance tensor.

$$C_{ijkl} = C_{jikl} = C_{ijlk} \tag{2.3}$$

The tensor of elastic coefficients or the compliance tensor has at most 81 components but due to the symmetry in the stress tensor and strain tensor, as shown in

Equation 2.3, the number of distinct components reduces to 36 and can be written as a 6 x 6 matrix when using index notation. Using this notation, the Generalized Hooke's law defined by Equations (2.1) and (2.2) can be written as:

$$\begin{aligned} &\sigma_\alpha = C_{\alpha\beta}\,\varepsilon_\beta \qquad (\alpha,\beta = 1,2,\ldots,6) \\ &or \\ &\varepsilon_\beta = S_{\alpha\beta}\,\sigma_\alpha \end{aligned} \tag{2.4}$$

It can be shown that $C_{\alpha\beta} = C_{\beta\alpha}$ (i.e. the stiffness matrix is symmetric) consequently, the number of independent terms is reduced to at most 21. The same conclusion can be drawn for the compliance matrix. Note that the stiffness matrix is simply the inverse of the compliance matrix.

A particular crystal symmetry or atomic arrangement can further reduce the number of independent constants. For a cubic crystal like silicon, when the crystal-axis coordinate system is used, the compliance matrix reduces to [62]:

$$S_{\alpha\beta}' = \begin{pmatrix} s_{11} & s_{12} & s_{12} & 0 & 0 & 0 \\ & s_{11} & s_{12} & 0 & 0 & 0 \\ & & s_{11} & 0 & 0 & 0 \\ & & & s_{44} & 0 & 0 \\ & & & & s_{44} & 0 \\ sym & & & & & s_{44} \end{pmatrix} \tag{2.5}$$

A similar matrix can be written for the stiffness matrix, $C_{\beta\alpha}'$. The presence of the prime indicates the use of the crystal coordinate system. The three independent components of the stiffness matrix and compliance matrix can be experimentally measured and are listed in Table 2.1.

Table 2.2: Stiffness and compliance coefficients for silicon [63]

s_{11}	s_{12}	s_{44}	c_{11}	c_{12}	c_{44}
	$(10^{11}\ \text{Pa})^{-1}$			$(10^{11}\ \text{Pa})$	
0.7691	-0.2142	1.2577	1.6564	0.6394	0.7951

The degree of anisotropy for cubic crystals can be measured via the Zener elastic-anisotropy index defined as [61]:

$$A = \frac{2c_{44}}{c_{11} - c_{12}} \tag{2.6}$$

where c_{ij} denote the three independent cubic-symmetry elastic-stiffness coefficients. The closer the index is to one the lower the degree of anisotropy. An isotropic material will have a Zener elastic-anisotropy index of 1. Silicon elastic anisotropy index being greater than 1, $A_{Si} = 1.56$, the Young's modulus, shear modulus and Poisson's ratio are direction dependent.

The influence of the direction on the Young's modulus can be represented in 3-D plots. Figure 2.3 shows the anisotropic behavior of the Young's modulus for silicon. For an isotropic material the shape will be a sphere. The greater the degree of anisotropy, the more distorted the shape will be.

A tensor transformation is needed to define the compliance matrix (or stiffness matrix) in an arbitrary coordinate system from the known values defined in the crystal coordinate system. The transformation rule for a fourth-order Cartesian tensor is given by [64, 65]:

$$S'_{ijkl} = a_{im}\, a_{jn}\, a_{kp}\, a_{tq}\, S_{mnpq} \tag{2.7}$$

where the indices of the direction cosines, a_{st}, run over 1,2,3.

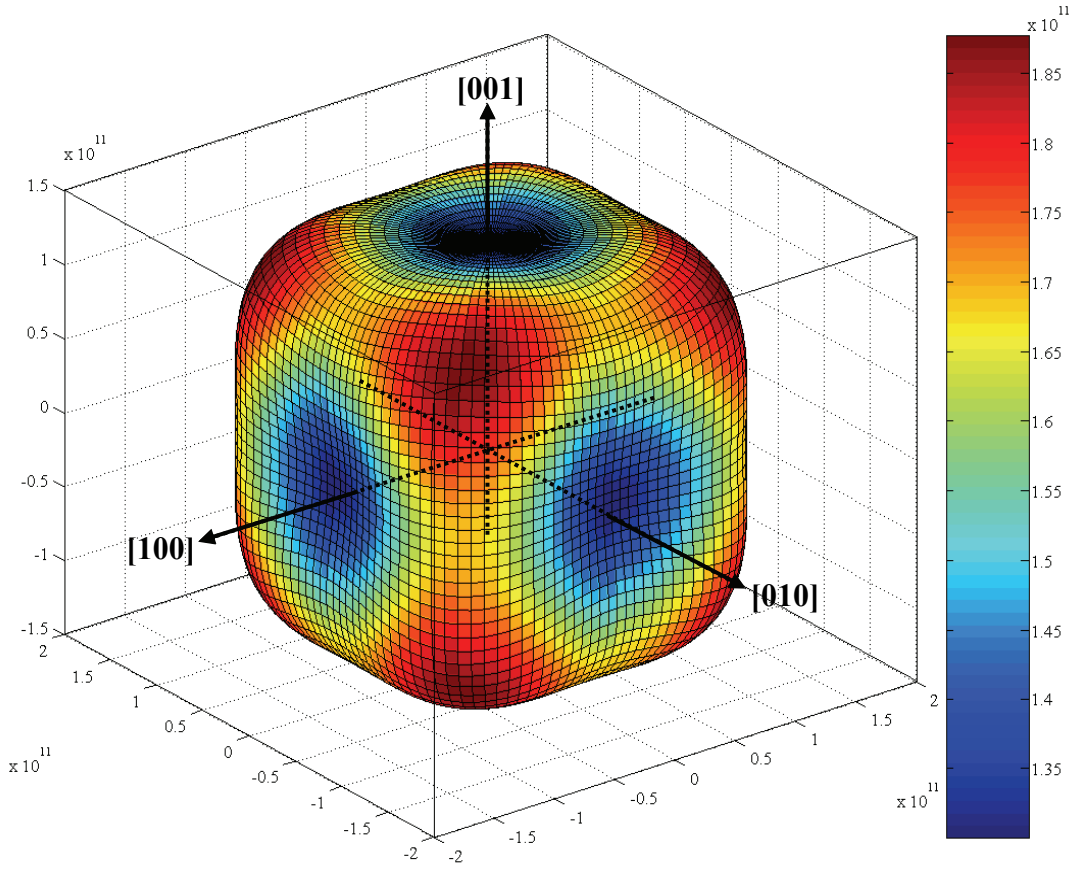

Figure 2.3: Young's modulus (in Pa) as a function of direction for silicon

As an example, the anisotropic material properties can be specified for EFG silicon wafers using the stiffness matrix defined in the wafer coordinate system (x, y, z), where x and y are the in-plane coordinates and z is the out-of-plane coordinate. The stiffness coefficients are obtained from the known stiffness coefficients for single cubic Si crystal with respect to the crystal coordinate system (x', y', z'). Although EFG wafers

are multi-crystalline wafers, there are known to have predominant grain orientation due to the growth process. Specifically, EFG wafers are characterized by a {110} surface and a <112> growth direction [66]. Stiffness is specified using the (110) single crystal properties taking $[1\bar{1}2]$, $[\bar{1}11]$ and [110] orientations as the x, y and z axes. For the EFG wafer, using the transformation defined in Equation 2.7, the elastic stiffness matrix obtained is given by (GPa):

$$C_{ijkl}^{EFG} = \begin{pmatrix} 203.85 & 44.83 & 44.83 & 0 & 0 & 0 \\ & 194.30 & 54.38 & -13.51 & 0 & 0 \\ & & 194.30 & 13.51 & 0 & 0 \\ & & & 60.40 & 0 & 0 \\ & & & & 60.40 & 13.51 \\ sym & & & & & 69.96 \end{pmatrix} \tag{2.8}$$

In light of the above work, it is evident that for crystalline silicon wafers, mechanical properties can be direction dependent. In this work, anisotropy of cubic single crystal silicon will be used when modeling Cz silicon wafers and EFG silicon wafers. For cast silicon wafers, isotropic mechanical properties will be assumed.

2.4 Summary

It is clear from this literature survey that:

- Very limited modeling and experimental work has been carried out on thin wafer handling. Particularly, knowledge of the handling stresses generated by different handling devices including the Bernoulli gripper for given handling control variables have not been reported in the literature.
- When handling thin substrates with the Bernoulli gripper, the analysis of the influence of substrate flexibility on the equilibrium lifting force, pressure distribution and stresses is lacking.
- A systematic approach to breakage analysis of crystalline silicon wafers during handling via analysis of the total stress state produced in the wafer is also not available in the literature.

Therefore the rest of this thesis describes work aimed at the fundamental understanding and characterization of thin wafer handling with a particular focus on Bernoulli gripping and the analysis of wafer breakage during handling through both modeling and experimental approaches.

CHAPTER III

MODELING OF THE PRESSURE AND LIFTING FORCE GENERATED BY A BERNOULLI GRIPPER ON A RIGID SUBSTRATE

This chapter presents the modeling and prediction of the air flow, pressure and lifting force produced by a non-contact Bernoulli gripper on a rigid planar substrate. Previous studies have demonstrated the turbulent behavior of the flow and the presence of a flow separation region at the nozzle of the gripper. Here, a Reynolds stress model has been implemented in a finite volume based segregated Reynolds-Averaged Navier-Stokes solver. Compressible air is modeled to capture the effect of the high flow velocities generated by the nozzle. In addition an experimental set up is designed to validate the model. This model could be used to understand the influence of handling variables such as the stand-off distance and air flow rate on the suction pressure distribution and lifting force acting on the rigid planar object.

3.1 Introduction

This chapter focuses on a commonly used non-contact handling device, namely the Bernoulli gripper. Bernoulli gripper (also known as a radial air outflow nozzle) was first patented and certified for lifting rigid circular semiconductor wafers [33, 34]. In this handling device, an axially directed air flow is diverged in the radial direction under appropriate flow and design conditions, creating a low pressure (vacuum) region between the gripper surface and a planar object (see Figure 3.1). This technique enables automated

handling of many types of materials ranging from thin silicon wafers to woven fabrics. Paivanas and Hassan [12] studied the radially diverging air flow nozzle for contactless handling of rigid semiconductors wafers. Modifications of the initial design included the use of an end mill cone to avoid direct impingement of the wafer surface by the radial air flow [35]. Grutzeck and Kiesewetter [36] analyzed the use of the Bernoulli effect in micro-part handling. Erzincanli et al. [37, 38] extended the use of the Bernoulli gripper to other non-rigid materials such as food. Ozcelik et al. [9, 38, 39] did experimental work on handling woven fabrics and other materials using this type of non-contact end-effector. Brun and Melkote [67] evaluated the stresses from measured deformation profiles when handling thin silicon wafers used in the Photovoltaic (PV) industry.

Modeling of the air pressure acting on the handled object due to radial air flow has been reported by Paivanas and Hassan [12, 17] for the initial Bernoulli gripper design without a mill cone. Their work assumes steady, laminar and incompressible flow conditions in order to solve the problem analytically. For their specific gripper geometry, they found that their model agreed reasonably well with their experimental pressure measurements results but was unable to capture the flow separation behavior near the nozzle opening due to the laminar assumption. A more accurate analysis requires that this assumption and others such as air incompressibility be relaxed. Furthermore, analysis of the flow generated by a Bernoulli gripper with a mill cone and the prediction of the pressure distribution and lifting force on the handled object has not been reported in the literature thus far. A model capable of such analysis is needed in order to understand the influence of different gripper variables on the pressure distribution and part handling force as well as for gripper design and handling process optimization.

This chapter addresses the aforementioned limitations of prior work on modeling and analysis of the Bernoulli handling device. Specifically, detailed computational fluid dynamics (CFD) modeling of the air pressure distribution and lifting force acting on a planar object is presented and experimentally verified. The model is used to study the influence of gripper variables such as air flow rate and stand-off distance on the pressure and force. The results obtained from this study can be used to optimize the gripper design.

3.2 Modeling

3.2.1 General Methodology

The model described in this chapter is a steady state representation of the turbulent flow generated by the Bernoulli gripper involving one species (dry air). Due to the flow separation region (see Figure 3.1), an appropriate turbulent flow model needs to be used. A Reynolds Average Navier-Stokes (RANS) approach as opposed to a Large Eddy Simulation (LES) will be used to approximately solve the Navier Stokes equations for practical reasons and avoid lengthy and expensive calculations.

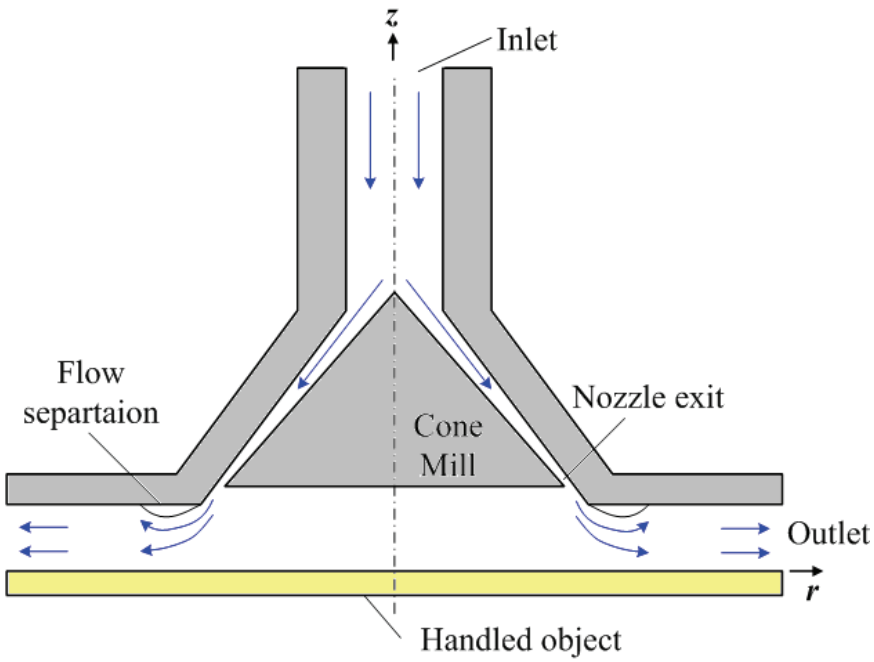

Figure 3.1: Schematic of a Bernoulli gripper with end mill cone

3.2.2 Governing Equations

The governing equations of the fluid motion are derived from the three basic physical laws of conservation: mass conservation, momentum conservation and energy conservation. These laws yield the continuity equation, the Navier-Stokes equation and the energy equation, respectively. In the case of the RANS approach, those equations are ensemble averaged. In Cartesian tensor form, the continuity equation is given by [68]:

$$\frac{\partial \rho}{\partial t} + \frac{\partial}{\partial x_i}\left(\rho u_i\right) = 0 \tag{3.1}$$

The Reynolds-averaged-Navier-Stokes equation is:

$$\frac{\partial \rho}{\partial t}(\rho u_i) + \frac{\partial}{\partial x_j}(\rho u_i u_j) = -\frac{\partial p}{\partial x_i} + \frac{\partial}{\partial x_j}\left[\mu\left(\frac{\partial u_i}{\partial x_j} + \frac{\partial u_j}{\partial x_i} - \frac{2}{3}\delta_{ij}\frac{\partial u_l}{\partial x_l}\right)\right] + \frac{\partial}{\partial x_j}\left(-\rho\overline{u_i' u_j'}\right) \tag{3.2}$$

In order to solve these equations the Reynolds stress term $\overline{u_i' u_j'}$, needs to be appropriately modeled. In order to capture accurately the flow separation region the Reynolds Stress Model (RSM) [69-71] approach was preferred to the isotropic dynamic viscosity assumption of the Bousinessq approach employed in the Spalart-Allmaras model, the k-ε models, and the k-ω models [72]. The RSM model closes the Reynolds-averaged-Navier-Stokes equation by solving transport equations for each of the terms in the Reynolds stress tensor, together with an equation for the dissipation rate. This means that five additional transport equations are required in 2D flows [72]. The exact transport equations for the transport of the Reynolds stresses may be written as follows [72]:

$$\frac{\partial}{\partial t}\left(\rho\overline{u_i' u_j'}\right) + C_{ij} = D_{ij}^T + D_{ij}^L + P_{ij} + G_{ij} + \phi_{ij} + \varepsilon_{ij} + F_{ij} \tag{3.3}$$

Of the various terms in these exact equations, C_{ij}, D_{ij}^L and P_{ij} do not require any modeling. However, D_{ij}^T, ϕ_{ij}, ε_{ij} and F_{ij} need to be modeled to obtain closure.

The turbulent kinetic energy, k, and its rate of dissipation, ε, are obtained from the following transport equations:

$$\frac{\partial}{\partial t}(\rho k) + \frac{\partial}{\partial x_i}(\rho k u_i) = \frac{\partial}{\partial x_j}\left[\left(\mu + \frac{\mu_t}{\sigma_k}\right)\frac{\partial k}{\partial x_j}\right] + \frac{1}{2}(P_{ii} + G_{ii}) - \rho\varepsilon\left(1 + 2M_t^2\right) \tag{3.4}$$

$$\frac{\partial}{\partial t}(\rho\varepsilon)+\frac{\partial}{\partial x_i}(\rho\varepsilon u_i)=\frac{\partial}{\partial x_j}\left[\left(\mu+\frac{\mu_t}{\sigma_k}\right)\frac{\partial\varepsilon}{\partial x_j}\right]+C_{\varepsilon 1}\frac{1}{2}[P_{ii}+C_{\varepsilon 3}G_{ii}]\frac{\varepsilon}{k}-C_{\varepsilon 2}\rho\frac{\varepsilon^2}{k} \qquad (3.5)$$

The turbulent heat transport is modeled using the concept of Reynolds' analogy to turbulent momentum transfer [72]. The energy equation is then:

$$\frac{\partial}{\partial t}(\rho E)+\frac{\partial}{\partial x_i}[u_i(\rho E+p)]=\frac{\partial}{\partial x_j}\left[\left(k+\frac{c_p\mu_t}{\mathrm{Pr}_t}\right)\frac{\partial T}{\partial x_j}+u_i(\tau_{ij})_{eff}\right]+S_h \qquad (3.6)$$

where E is the total energy and $(\tau_{ij})_{eff}$ is the deviatoric stress tensor defined as [72]:

$$(\tau_{ij})_{eff}=\mu_{eff}\left(\frac{\partial u_i}{\partial x_j}+\frac{\partial u_j}{\partial x_i}\right)-\frac{2}{3}\mu_{eff}\frac{\partial u_i}{\partial x_i}\delta_{ij} \qquad (3.7)$$

To solve these equations, initial and boundary conditions must be specified. These partial differential equations are highly non-linear and cannot be solved by explicit, closed-form analytical methods. A control volume approach is used to convert the governing equations to algebraic equations that can then be solved numerically. The model described above was implemented in the FLUENT® code, a general purpose commercial CFD software. The modeled fluid flow domain was divided into quadrilateral control volumes.

3.2.3 Model Geometry

Due to the axial symmetry of the gripper geometry, a 2D axi-symmetric model has been developed to reduce computing time. The domain geometry was simplified and is shown in Figure 3.2. Note that the handled object is assumed to be flat and rigid only for the ease of experimental validation. This assumption will be relaxed in the next chapter to account for elastic deformation effects of a non-rigid object (e.g. thin flexible

semiconductor wafer). The dimensions were determined from a commercially available gripper used for thin wafer handling in the photovoltaic Industry and are listed in Table 3.1. The stand-off distance, H, is either fixed by equilibrium or mechanically imposed. In the current gripper there are four rubber pads (mechanical stops) located radially around the gripper that are used as locators, thereby fixing the stand-off distance. Two grid geometries were developed to analyze the influence of the stand-off distance on flow characteristics.

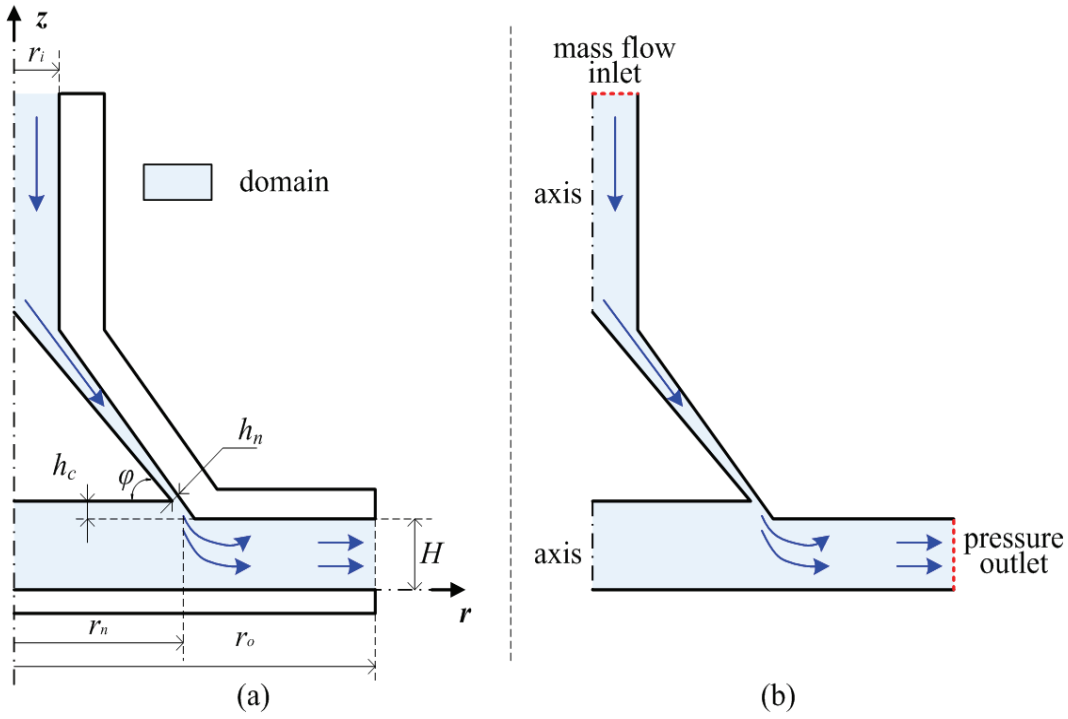

Figure 3.2: (a) Simplified model geometry, (b) Fluid domain with boundary conditions

Table 3.1: Geometric dimensions of the modeled gripper

Gripper Geometry	Value
Inlet radius, r_i	2.0 mm
Nozzle radius, r_n	18.0 mm
Oultet radius, r_o	40.0 mm
Nozzle flow height, h_n	0.1 mm
Cone mill height, h_c	1.4 mm
Stand-off distance, H	2 mm, 3 mm
Cone mill angle, φ	45 º

3.2.4 Boundary Conditions

Figure 3.2 shows the circulation of air through the Bernoulli gripper. The boundary conditions are shown in Figure 3.2b. A mass flow inlet boundary condition is used to prescribe a mass flow rate and temperature of the air at the inlet. At the outlet, the pressure outlet boundary condition was preferred to the outflow boundary condition since it often results in a better rate of convergence when backflow occurs during iterations. The pressure outlet boundary condition was used to prescribe the static pressure at the flow outlet. An axis boundary condition was used to define the axis of symmetry of the model. All other boundary conditions consisted of wall boundary conditions with no heat flux. The prescribed values of the boundaries conditions are listed in Table 3.2.

Table 3.2: Boundary conditions specification

Boundary type	Value
Mass flow inlet	• Mass flow rates: 1 g/s, 1.5 g/s, 2 g/s, 2.5 g/s, 3 g/s • Temperature: 300 K
Pressure outlet	• Gauge pressure: 0 Pa
Wall	• Heat flux: 0 W/m^2

3.2.5 Material

The single fluid material modeled is air. Except for the density, default properties of air from the FLUENT® Database have been used. The density of air is modeled with the ideal gas law for compressible flows as [72]:

$$\rho = \frac{p_{op} + p}{\frac{R}{M_w}T} \tag{3.8}$$

where, p is the gauge pressure predicted and pop the operating pressure (p_{op}=101325 Pa).

At Mach numbers much less than 1.0, compressibility effects are negligible and the variation of the gas density with pressure can be safely ignored. The variation of the Mach number at the nozzle inlet as a function of the mass flow rate is shown in Figure 3.3 and indicates that compressibility effects are important and need to be considered in the model.

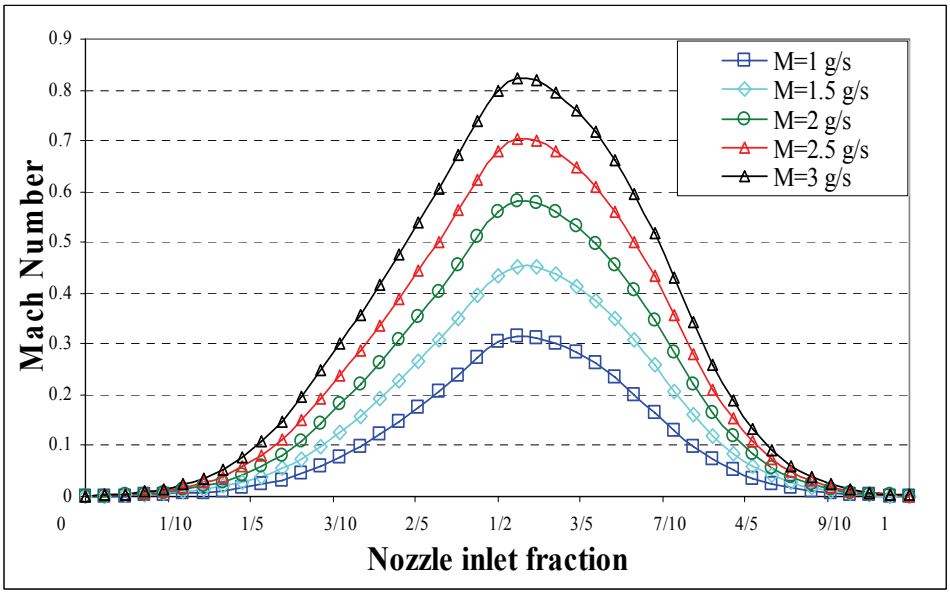

Figure 3.3: Mach number variation at the nozzle inlet as a function of the mass flow rate, M

3.2.6 Solution Method

The governing equations in the present study are solved using the finite volume method. The governing equations include the continuity, momentum, energy, and the RSM equations. The steady segregated implicit scheme solver was used to numerically solve these equations for the axi-symmetric geometry case. In addition, the SIMPLE (Semi-Implicit Method for Pressure-Linked Equations) algorithm was chosen for the pressure velocity coupling. It uses a relationship between velocity and pressure corrections to enforce mass conservation and to obtain the pressure field [72].

When using a control volume based technique approach, the governing equations are integrated about each control volume yielding equations that conserve each quantity on a control volume basis. These quantities (e.g. density, pressure…) are stored at the cell centers. However the face values are needed for the convection terms and must be interpolated from the cell center values. This is accomplished using an upwind scheme in which the face value of a quantity is derived from quantities in the cell upstream, or "upwind" relative to the direction of the normal velocity. Several upwind schemes are available in FLUENT®. In this work, first order accuracy upwind schemes were chosen for density, momentum and turbulence kinetic energy. All the other variables were discretized using second order upwind schemes for high accuracy. For stability reasons, first order scheme solutions were first obtained before switching to a higher order scheme.

Convergence was declared when the overall lifting force generated by the gripper was not changing between successive iterations. The lifting force was calculated as the surface integral of the gauge pressure acting on the handled object and is shown in Figure

3.4. In addition, as illustrated in Figure 3.5, the maximum scaled residuals were checked to be less than 10^{-4} for the continuity, velocity and temperature equations and less than 10^{-5} for the turbulent kinetic energy, dissipation rate and all Reynolds stresses. The under relaxation factors for pressure and momentum were set to 0.4. These ensured numerical stability and faster convergence of the solution.

3.2.7 Mesh and Grid Independence

The mesh employed for the model solution is shown in Fig. 3.6. As seen, four node quadrilateral cells were used to define the 2D structured grid. The skewness of the cells was checked and was found to be less than 0.5. The grid resolution is very important to produce reasonable results. The grid should be especially fine along the air flow path.

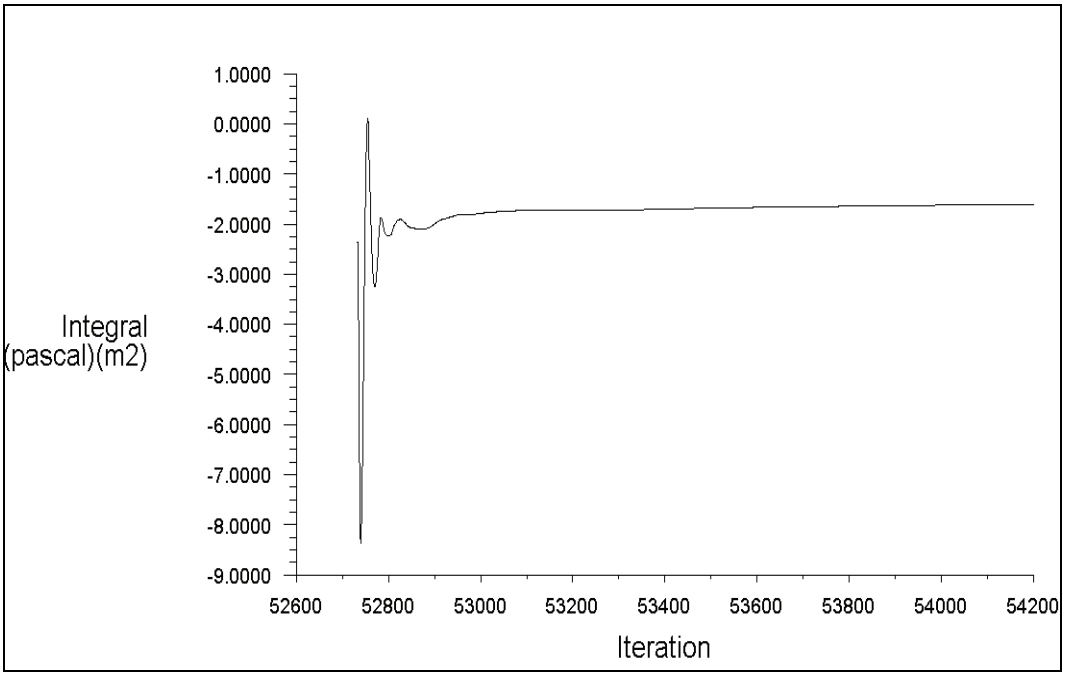

Figure 3.4: Lifting force convergence monitoring (*M*=2 g/s, *H*=2 mm)

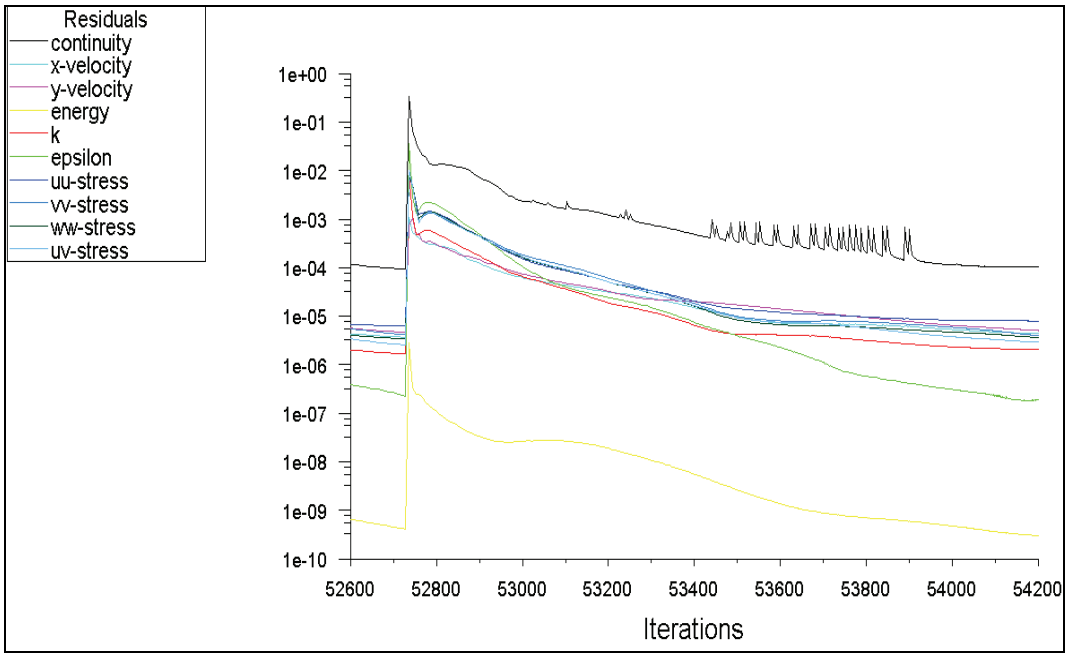

Figure 3.5: Residuals convergence monitoring (M=2 g/s, H=2 mm)

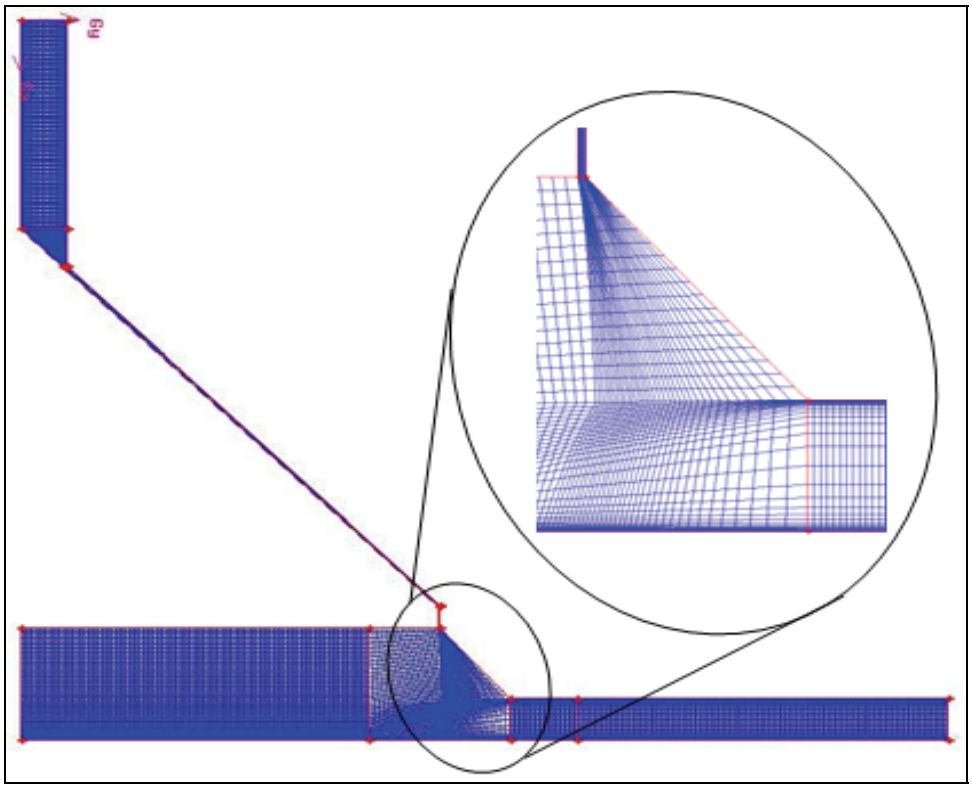

Figure 3.6: Actual grid used in the model

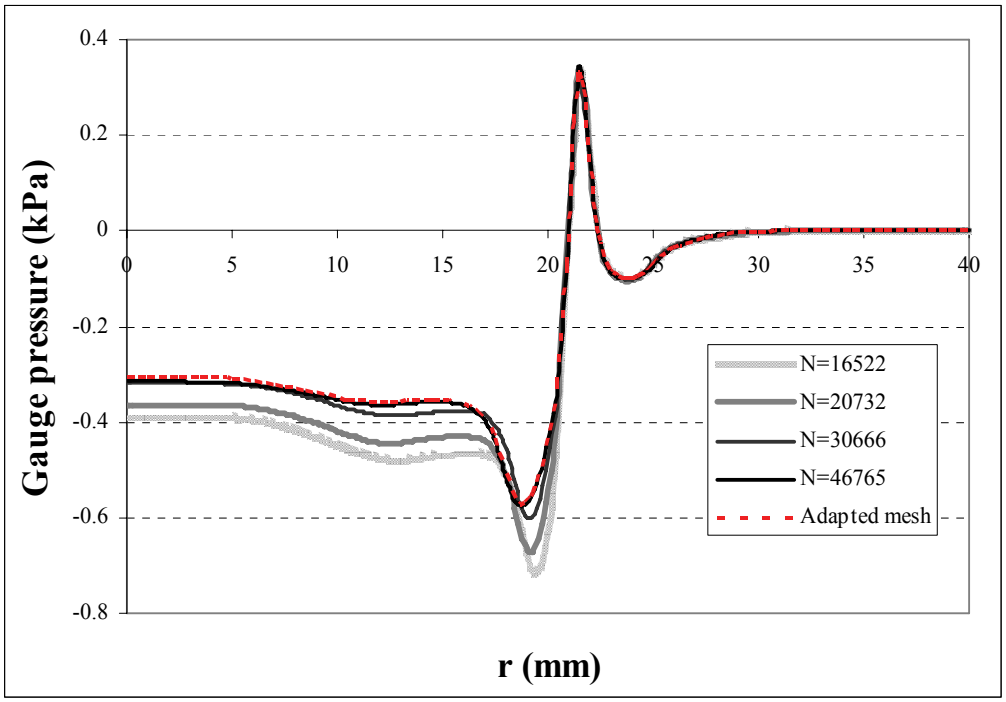

Figure 3.7: Influence of the number of cells on the predicted radial gauge pressure generated by a Bernoulli gripper on the surface of the handled object

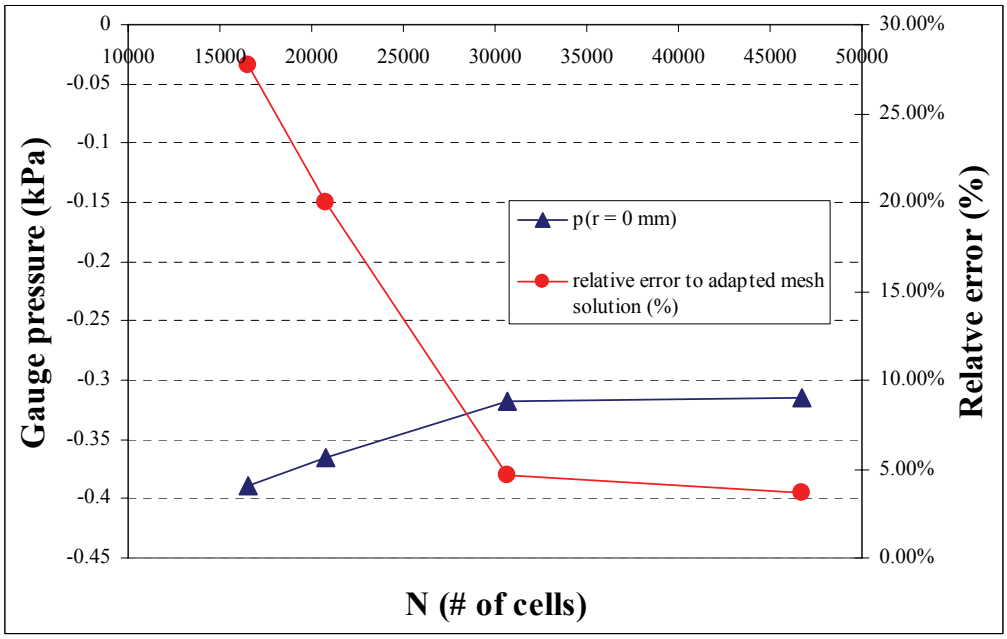

Figure 3.8: Influence of the number of cells on the predicted lifting force and relative error compared to the dynamic adaptive grid solution

An important factor related to the quality of CFD simulations is the quality of the computational grid. Analysis of grid independence was performed. The sensitivity of the results to the grid resolution was tested for the computed radial pressure distribution and lifting force predicted for four different grids. The number of cells per flow passage N_f, was refined iteratively to obtain reliable results. Table 3.3 shows the number of quadrilateral cells, N, with respect to the number of elements per flow passage. The different computational grids were compared to a dynamic adaptive mesh solution (a feature available in FLUENT®). The predicted radial gauge pressure distribution generated by the gripper on the handled planar object is shown in Figure 3.7. As the number of quadrilateral cells is increased, the solution tends to converge to the adaptive mesh solution. In addition, Figure 3.8 shows the predicted lifting force generated by the gripper for the different meshes from which similar conclusions can be drawn; the predicted lifting force approaches the solution obtained for the adaptive mesh. The relative error of the predicted lifting force compared to the adapted mesh solution is also plotted as a function of the number of cells used and is seen to be less than 1.5% for the finest mesh. It is also important to note that the relative change in the predicted lifting force between the two finest grid models is small. Since the simulation time of these models is reasonable (2-4 hours on a single Pentium 2.8 GHz processor machine) the finest mesh with $N_f = 42$ is taken to be adequate to produce grid independent results.

Table 3.3: Different grids used for the grid independence check and corresponding number of cells

Number of cells per flow passage, N_f	24	28	34	42
Total number of quadrilateral cells, N	16522	20732	30666	46765
Number of nodes, n	17167	21434	31521	47821

3.3. Experimental Validation

3.3.1 Experimental Procedure

An experimental setup used to measure the pressure distribution imposed on the surface of the handled object by the Bernoulli gripper has been designed. It consists of a 4-axis Adept® SCARA robot equipped with a Bernoulli gripper. Figure 3.9 shows a picture of the setup. An air flow sensor plus controller is used to monitor and adjust the air flow rate while pressure sensors mounted on a circuit board enable direct measurement of the air pressure between the gripper and the substrate surface representing the handled object.

The air flow controller (OMEGA FMA-2610A) is mounted on the robot inline with the air flow as close to the gripper as possible to minimize the effect of pressure losses in the pipe from the controller to the gripper. The air flow controller allows precise measurement and control of the volumetric air flow rate. In addition, the mass flow rate, gage pressure and temperature are measured by the air flow sensor. The pressure sensor (Honeywell ASDX001D4) is used to measure the differential pressure. The sensor is connected to a flat rigid polymer substrate, representing the handled object. A small hole in the rigid substrate allows the gauge pressure on the top surface of the handled object to be measured. Note that the hole has been made as small as possible (0.5 mm) to make the

measurement less intrusive. The pressure sensor is connected to the robot controller via an analog I/O DeviceNet module (OMRON DRT2-AD04H) allowing simultaneous acquisition of the instantaneous robot location and the corresponding gauge pressure.

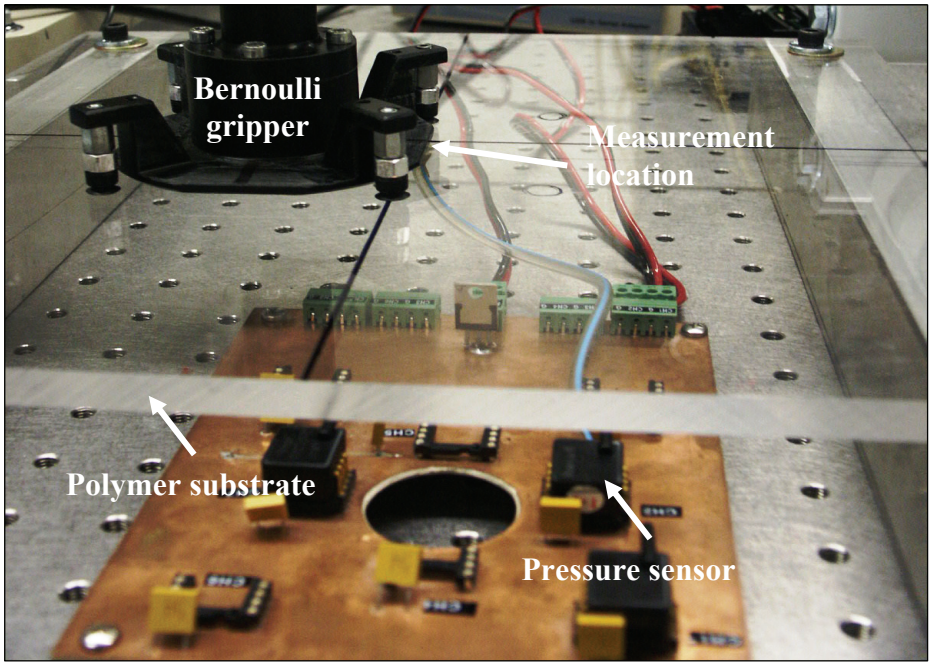

Figure 3.9: Experimental set-up

The following measurement procedure is used. After stabilizing the air flow at a given rate, the robot moves the gripper along a programmed scanning path above the rigid instrumented substrate at the specified stand-off distance and continuously records the robot location and gauge pressure. In order to measure both positive and negative gauges pressures the scanning procedure needs to be repeated twice since the sensor is capable of measuring gauge pressure relative to the ambient pressure. Figure 3.10 shows a typical example of the measured gauge pressure distributions for the vacuum and positive pressure regions. The data is then collected and combined to generate the total

gauge pressure distribution contour maps for each test condition. Note that the air flow characteristics are measured during the scanning cycle and used to account for the variability of the flow during the measurement.

A full factorial design of experiment was carried out. The factors studied are the stand-off distance and the volumetric air flow rate. The stand-off distance was set to two different levels, 2 mm and 3 mm. The volumetric air flow rate, V, was set to five different levels ranging from 30 to 40 l/min. The choice of this range for V is based on the fact that below 30 l/min the lifting force is too small to pick-up and transport the wafer. The 40 l/min value is close to the maximum air flow rate for the Bernoulli gripper used in this study.

3.3.2 Experimental Results

Table 3.4 lists the volumetric air flow rate, temperature, inlet pressure and mass flow rate measured by the air flow controller for the different test cases. The influence of the volumetric air flow rate and stand-off distance on the pressure acting on the surface of the substrate is shown in Figure 3.11. As expected, the experimental result shows negative gauge pressure in the center of the gripper and positive pressure around the nozzle location. Also, for a given stand-off distance, the vacuum level (and therefore the resulting lifting force) is higher at higher values of the volumetric air flow rate. Similarly, for a given volumetric air flow rate, the vacuum level (and lifting force) is lower at higher stand-off distances. It is important to notice that the pressure distribution is not perfectly axi-symmetric, especially when looking at the positive gauge pressure regions. The positioning error of the mill cone in the gripper was adjusted in order to minimize the variation in the nozzle height h_n and thus the non-symmetric behavior of the flow.

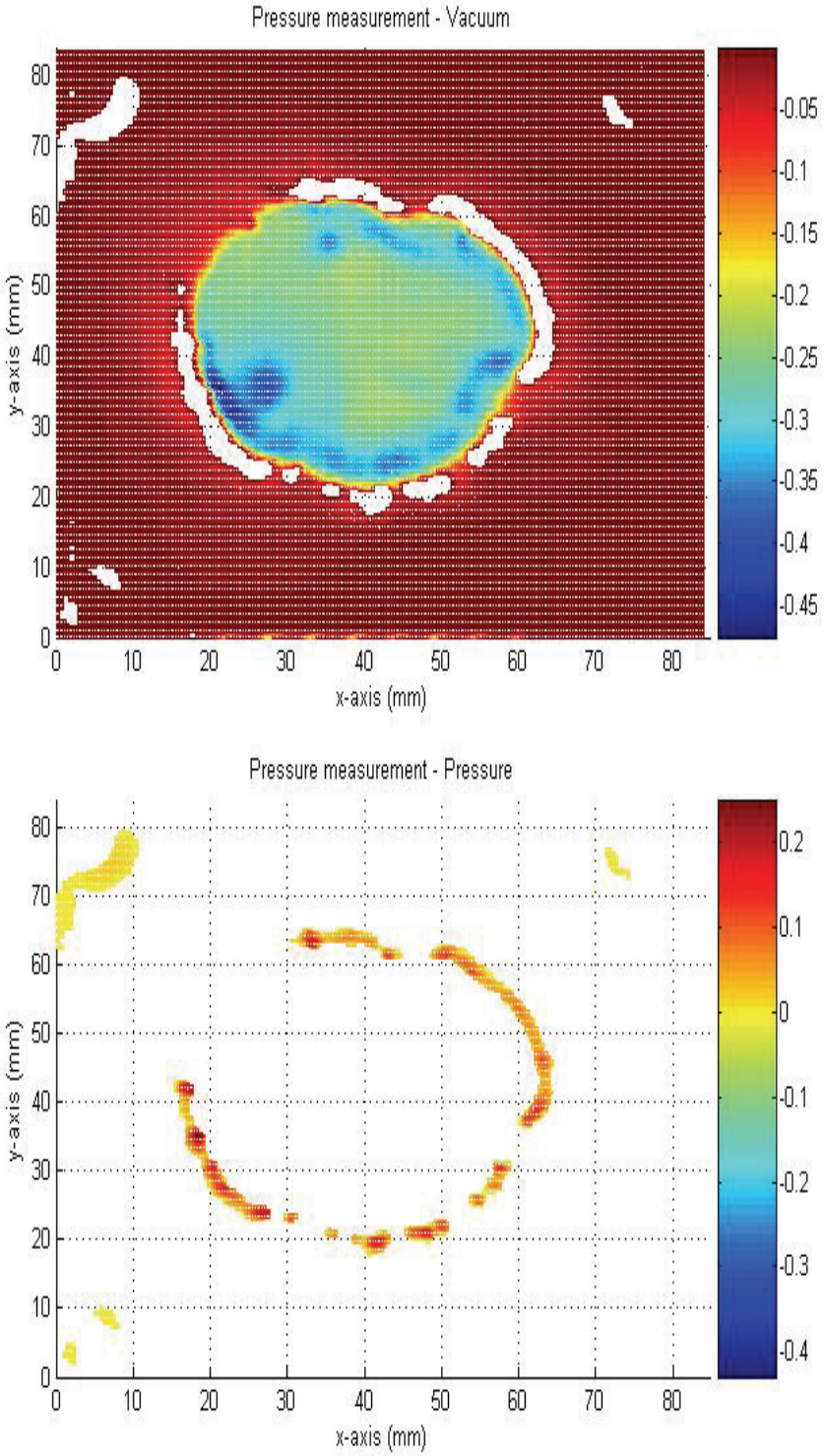

Figure 3.10: Measured gauge vacuum distribution and corresponding gauge pressure distribution (kPa) (V=30 l/min, H=2mm)

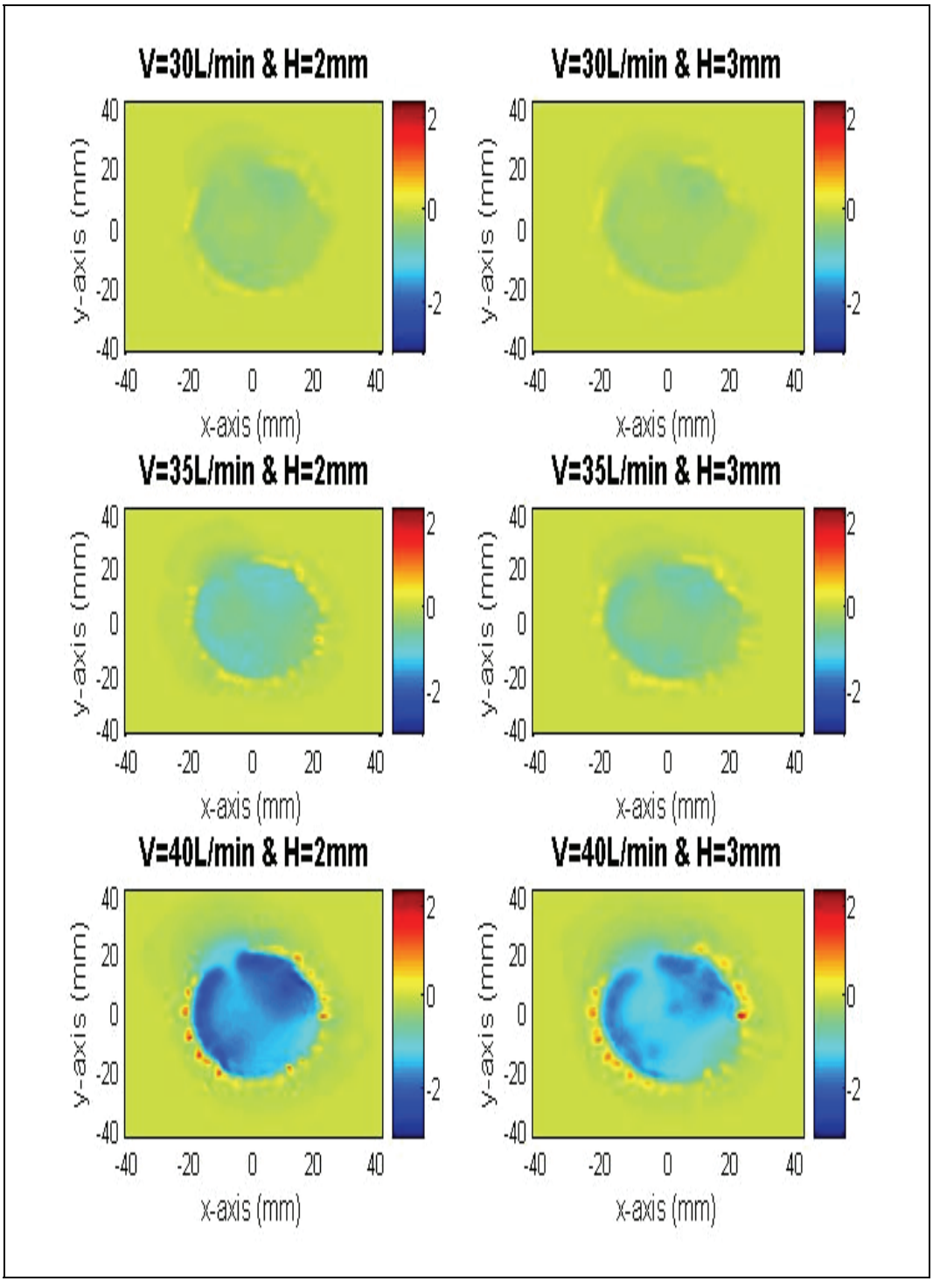

Figure 3.11: Gauge pressure distribution maps (kPa) for specific volumetric flow rate (*V*) and stand-off distance (*H*) pairs

Table 3.4: Average measured air flow characteristics for given volumetric flow rates and stand-off distances

H (mm)	V_{set} (L/min)	T_{ave} (ºC)	p_{ave} (kPa)	M_{ave} (g/s)
2	30.0	28.3	196.6	1.14
	32.5	27.6	219.7	1.38
	35.0	27.0	257.2	1.74
	37.5	26.5	298.3	2.16
	40.0	25.6	352.9	2.74
3	30.0	28.0	195.7	1.13
	32.5	27.9	219.8	1.38
	35.0	27.1	260.0	1.76
	37.5	26.4	297.0	2.16
	40.0	25.7	357.7	2.78

3.3.3 Model Validation

Figure 3.12 shows the contour plot of the radial velocity at M=3 g/s and H=2mm. The flow behavior reveals interesting features such as the flow separation region and the recirculation around the nozzle exit. These features are also represented in Figure 3.13 where path lines of the flow are plotted from the nozzle exit. Using the mean velocity of flow, the Reynolds number has been calculated for different radial locations and is indicated in the Figure 3.12 at three different locations. The Reynolds number ranges from around 7200 to 1300 suggesting a turbulent-to-laminar transition from the nozzle exit to the outer edge of the gripper. Similar trends were noted by Paivanas and Hassan [12] in their analysis of the direct impingement Bernoulli nozzle (which differs from the cone mill gripper modeled in this study). This confirms the necessity for a turbulent flow model in the simulations.

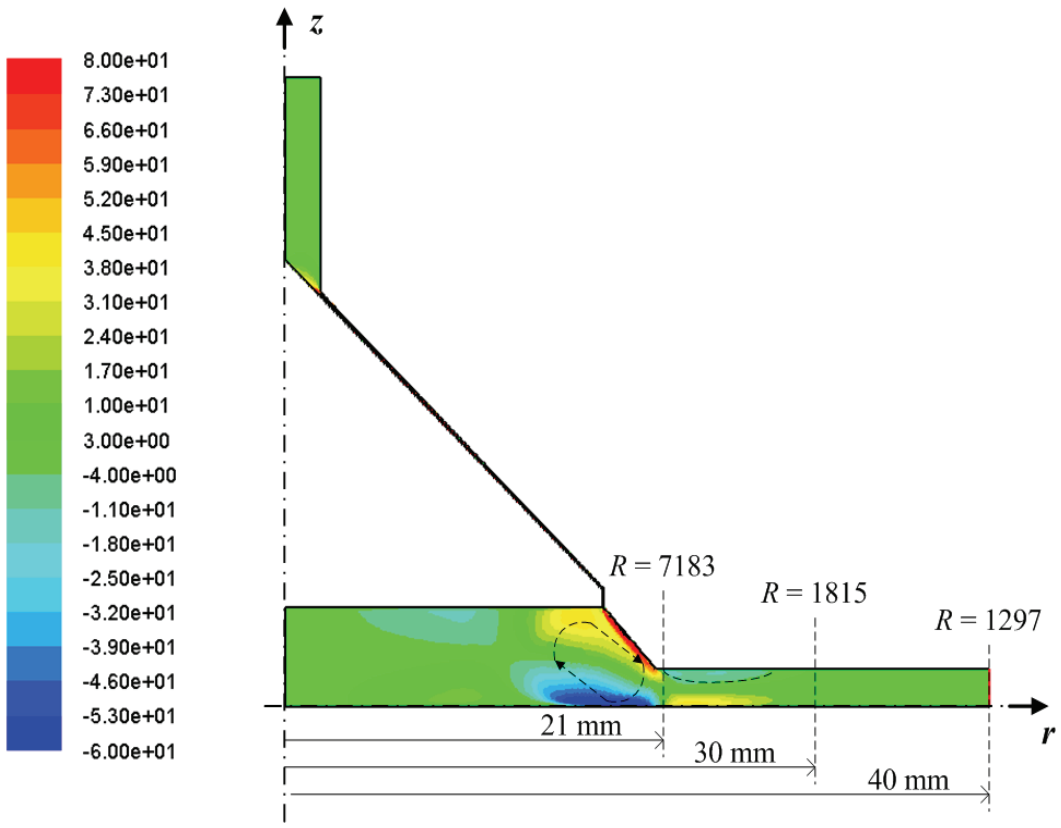

Figure 3.12: Contour plot of the radial velocity and Reynolds number values (M=3 g/s, H=2 mm)

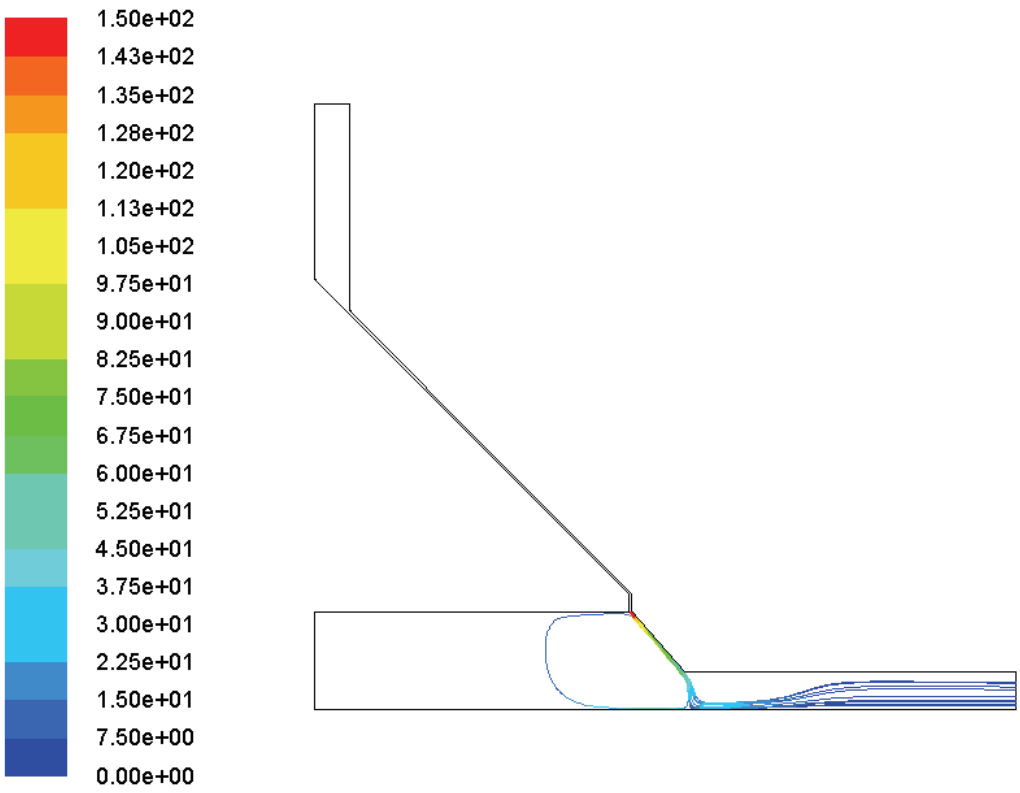

Figure 3.13: Path lines of the flow colored by the magnitude of the velocity (m/s) (M=3 g/s, H=2 mm)

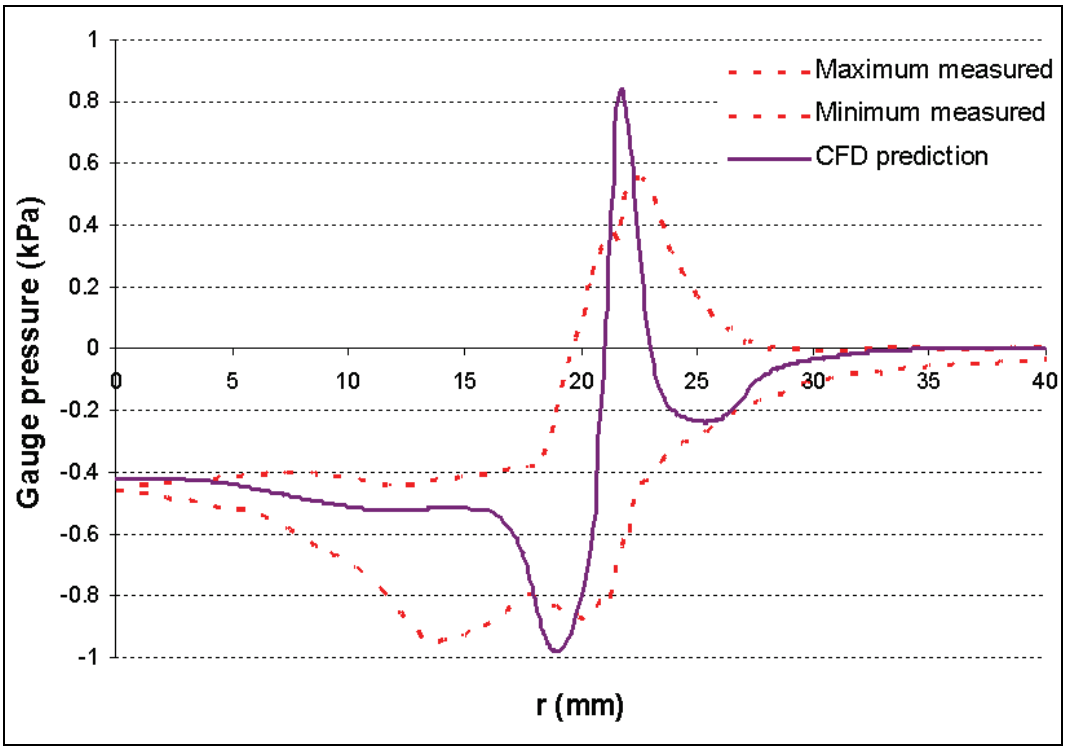

Figure 3.14: Measured vs. predicted radial gauge pressure on the surface of the handled object (V=35 l/min, H=3 mm)

Figure 3.14 shows the comparison of the measured and the predicted radial gauge pressure on the surface of the substrate for H=3 mm and V=30 l/min. Since, unlike the model, the actual gripper is not perfectly axi-symmetric, the simulated radial pressure cannot be compared directly with the gauge pressure distribution maps obtained experimentally (cf. Figure 3.11). Due to imperfections in the gripper geometry, the measured gauge pressure distribution is not perfectly symmetric and is characterized by different gauge pressure values at a given radius. Consequently, the min-max envelope of the measured radial gauge pressure distribution is extracted and compared with the simulated pressure distribution as shown in Figure 3.14. It can be seen from Figure 3.14

that the model prediction falls mostly within the min-max envelope except in the vicinity of the nozzle exit. Note that the comparison is very good at the center of the gripper i.e. $r = 0$, where most of the lifting force is generated.

A comparison of the experimental data and model simulations as a function of the mass flow rate is shown in Figure 3.15. The experimental lifting force was obtained by numerical integration of the measured gauge pressure distribution and compared to the lifting force predicted by the FLUENT® simulation. The variation in mass flow rate during measurement is indicated by the horizontal error bars. The model simulations for the two stand-off distances considered here are seen to predict the lifting force as a function of the mass flow rate reasonably well. The average relative errors are 8% and 6% for the two stand-off distances, H=2 mm and H=3 mm, respectively. Note that the maximum relative error (18%) occurs at the maximum air flow rate and at the minimum stand-off distance. This is thought to be due to the intrusive nature of the pressure sensor used, which, when placed very close to the impinging flow can affect the air flow behavior.

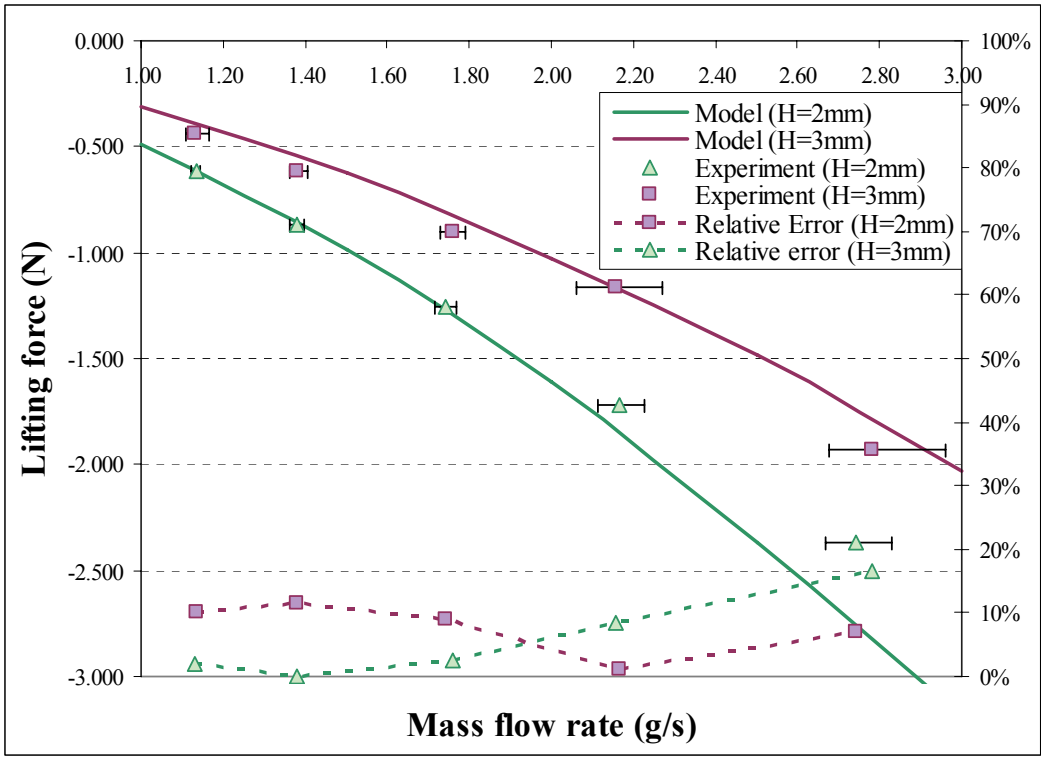

Figure 3.15: Predicted vs. calculated lifting force at two stand-off distances (*H*=2 mm and *H*=3 mm)

3.4 Summary

This chapter presented a computational fluid dynamics model of a non-contact Bernoulli gripper used for low-force handling of small and large rigid and non-rigid materials. The model was used to compute and predict the air flow, pressure distribution and lifting force generated by the gripper. The handled object was assumed to be flat in order to experimentally validate the model. A turbulent Reynolds stress model was used in a finite volume Reynolds-Averaged Navier-Stokes solver implemented in the general purpose CFD software FLUENT®. The model explicitly considers the non-steady characteristics of the air flow generated in the gripper and represents an enhancement over prior work in this area.

Comparison with experimental results showed that the model predictions of the pressure and lifting force agree favorably for the conditions examined. Specifically, the lifting force generated by the gripper was generally predicted within 12% of the measured values for most cases. The error was highest (18%) at the minimum stand-off distance and maximum flow rate.

The results obtained from this study can be used to evaluate the lifting force and pressure distribution on the handled object as a function of gripper variables such has the volumetric air flow rate and stand-off distance. When handling thin brittle wafers for example, the output of this model could be used as an input to a wafer deformation/stress model to calculate the wafer handling stresses generated by the gripper. This approach is presented in the next chapter.

CHAPTER IV

EFFECT OF SUBSTRATE FLEXIBILITY ON THE PRESSURE DISTRIBUTION AND LIFTING FORCE

This chapter presents the modeling and analysis of the pressure distribution and lifting force generated by a Bernoulli gripper when handling flexible substrates such as thin silicon wafers. A Bernoulli gripper is essentially a radial airflow nozzle used to handle large and small, rigid and non-rigid materials by creating a low-pressure region or vacuum between the gripper and material. The previous chapter analyzed the pressure distribution and lifting force generated by a Bernoulli gripper for handling thick substrates that undergo negligible deformation. Since the lifting force produced by the gripper is a function of the gap between the handled object and the gripper, any deformation of the substrate will influence the gap and consequently the pressure distribution and lifting force. In this chapter, the effect of substrate (thin silicon wafer) flexibility on the equilibrium wafer deformation, radial pressure distribution and lifting force is modeled and analyzed using a combination of computational fluid dynamics (CFD) modeling and finite element analysis. The equilibrium wafer deformation for different air flow rates is compared with experimental data and is shown to be in good agreement. In addition, the effect of wafer deformation on the pressure and lifting force are shown to be significant at higher volumetric airflow rates. The modeling and analysis approach presented in this chapter is particularly useful for evaluating the effect of gripper variables on the handling stresses generated in thin silicon wafers.

4.1. Introduction

Breakage-free handling of flexible substrates such as thin large area silicon wafers is becoming increasingly important in semiconductor and photovoltaic (PV) manufacturing. This problem is particularly significant in the PV industry, which is trying to lower the cost of solar energy via the use of thin, and large area silicon substrates without compromising production yield [5]. Of the various wafer-handling methods used in the PV industry, the Bernoulli gripper, also known as a radial airflow nozzle, is of particular interest because of its ability to handle both rigid and non-rigid objects with low force application.

This type of gripper was first patented and certified for handling thick rigid circular semiconductor wafers [33, 34]. In this handling device, an axially directed airflow is diverged in the radial direction under appropriate flow and design conditions, creating a low pressure region or partial vacuum between the gripper surface and the held object (see Figure 4.1). Paivanas and Hassan [12] studied the radially diverging airflow nozzle for contactless handling of thick semiconductor wafers. Note that the gripper design shown in Figure 4.1 has mechanical stops (rubber pads) to prevent lateral motion of the handled object. These stops are characteristic of the gripper design used in PV applications but are absent in the version considered by Paivanas and Hassan [4]. Modifications of the initial gripper design analyzed by Paivanas and Hassan included the use of a cone mill to avoid direct impingement of the wafer surface by the radial airflow [35]. Grutzeck and Kiesewetter [36] analyzed the use of the Bernoulli principle for micro-part handling. Erzincanli et al. [37, 38] extended the use of the Bernoulli gripper to other non-rigid materials such as food while Ozcelik et al. [8, 9, 11] reported experimental work on handling woven fabrics and other materials.

In their work, Paivanas and Hassan [12, 17] modeled the air pressure generated by a Bernoulli gripper without a cone mill. They assumed steady, laminar and incompressible airflow conditions in order to solve the problem analytically. Their model agreed reasonably well with their pressure measurements but was unable to capture the flow separation region near the nozzle opening due to the laminar flow assumption. More recently, Brun and Melkote [73] presented a computational fluid dynamics (CFD) model of the pressure distribution and lifting force generated by a Bernoulli gripper with a cone mill. Although the assumptions of laminar flow and incompressibility were relaxed in this work, the model did not consider the influence of substrate flexibility (deformation) on the resulting pressure and lifting force. When handling a flexible object such as a thin silicon wafer (thickness $\leq$ 250 μm), the low pressure created by the radially diverging airflow tends to deform the wafer as illustrated schematically in Figure 4.1 The deformation of the wafer in turn alters the air gap between the gripper and wafer, which in turn affects the airflow and the resulting air pressure distribution and handling force. It is of interest to model and analyze this effect of substrate flexure on the equilibrium wafer, radial air pressure distribution and lifting force generated by the Bernoulli gripper when handling thin flexible materials such as silicon wafers.

Therefore, this chapter makes use of an iterative fluid-structure modeling approach to analyze the effect of substrate deformation on the resulting equilibrium air pressure distribution and lifting force. The modeling approach uses a combination of computational fluid dynamics (CFD) modeling and finite element (FE) analysis. The model is used to study the influence of gripper variables such as volumetric airflow rate on the equilibrium wafer deformation, radial air pressure distribution and lifting force. Note that although the analysis presented in this chapter is for a thin silicon wafer, the

approach is applicable to any air impermeable flexible substrate. For a given substrate material, the model can be used to optimize the Bernoulli gripper design and, in the case of thin silicon wafers, to minimize their breakage due to excessive deformation (and hence stresses) imposed on the wafer during handling.

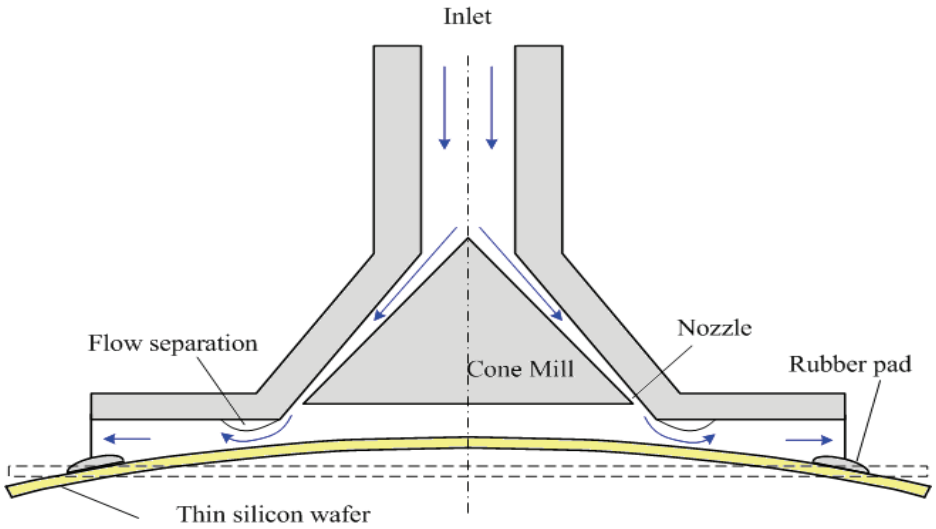

Figure 4.1: Schematic of a Bernoulli gripper used for high-throughput handling of silicon wafers in the PV industry

4.2 Modeling

4.2.1 Approach

Figure 4.2 shows a flowchart of the modeling and analysis approach used in this work. For a given wafer material and gripper geometry, the radial air pressure distribution acting on the initially undeformed wafer surface is determined from the solution of a CFD model of the Bernoulli gripper. This pressure distribution is then imposed as a boundary condition on a non-linear finite element model (FE) of the undeformed and stress-free wafer to obtain the wafer deformation due to the imposed

pressure. Since the air pressure between the gripper and wafer is a function of the gap and this gap is affected by the wafer deformation, an iterative process is necessary to obtain the equilibrium wafer deformation and the corresponding radial air pressure distribution. Convergence of the solution is declared when the difference between the wafer deformation profiles obtained in two consecutive iterations steps is less than a specified tolerance (ε). The equilibrium lifting force acting on the deformed wafer can be easily obtained by integrating the converged air pressure distribution.

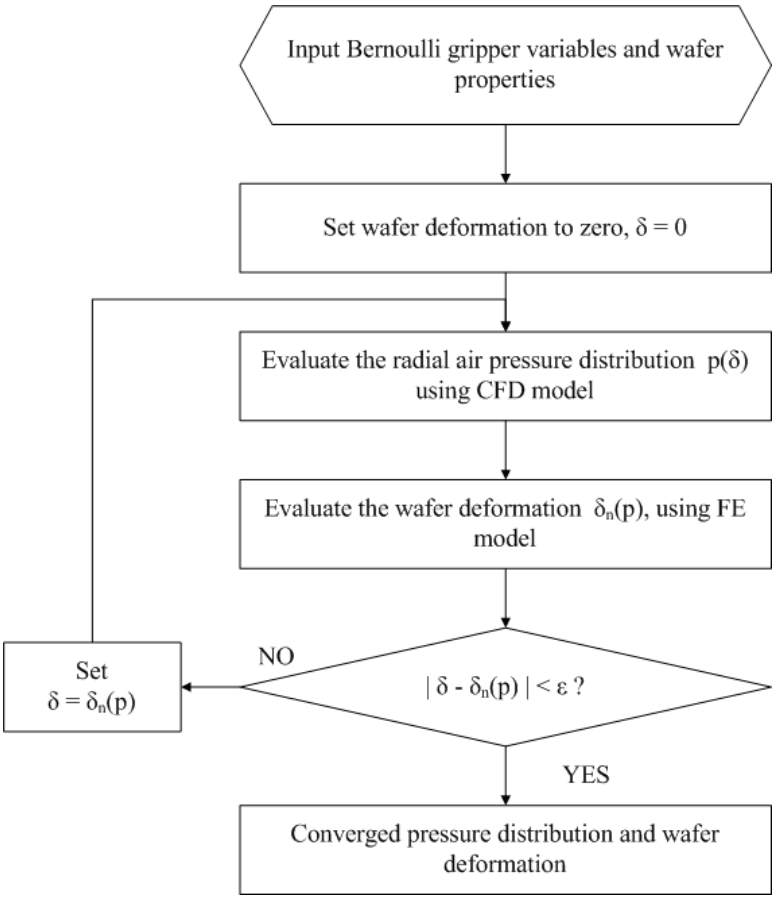

Figure 4.2: Flowchart of the iterative approach used to analyze the effect of substrate deformation on the pressure distribution generated by a Bernoulli gripper

4.2.2 Pressure Distribution Modeling

A detailed description of CFD modeling of the Bernoulli gripper to obtain the radial air pressure distribution was presented in the previous chapter. However, a few aspects of this model are briefly discussed here. Unlike the work of Paivanas and Hassan [17], the CFD model employed in this chapter considers the effects of turbulent and compressible flow. A turbulent Reynolds stress model is used in a finite volume Reynolds-Averaged Navier-Stokes solver implemented in the general purpose CFD software FLUENT®. As shown in Figure 3.12, this model is able to capture the flow separation region present in the gripper (see Figure 4.1) in addition to the predicted radial air pressure distribution being in good agreement with experimental results for a rigid substrate. A key difference between the earlier CFD model and the one used in this chapter is the use of a moving boundary to represent the wafer deformation as shown in Figure 4.3. Consequently, the influence of substrate flexure on the radial air pressure distribution is accounted for in the model. Note also that the gripper is assumed to be perfectly axi-symmetric. Although not entirely true, this assumption allows significant savings in computation time by not requiring a full 3-D model of the gripper. Additionally, as shown in the previous chapter, the radial pressure distribution and lifting force predictions obtained using this assumption are in good agreement with experimental results and consequently the assumption is retained here.

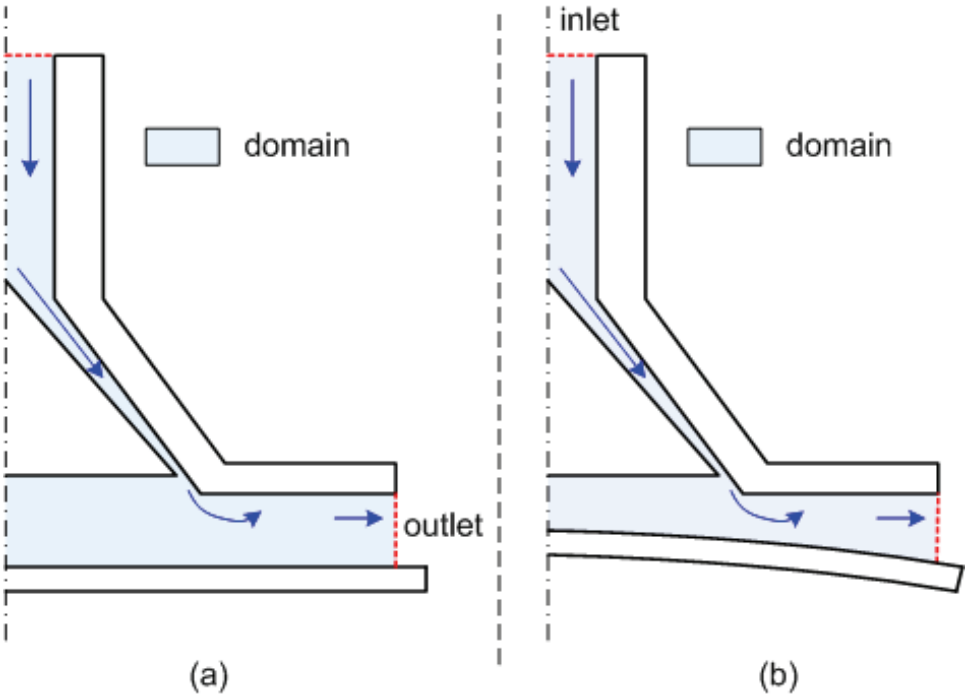

Figure 4.3: Fluid domain used in the CFD simulations: (a) rigid substrate (b) flexible substrate

4.2.3 Wafer Deformation Modeling

The deformation of the silicon wafer due to the radial air pressure distribution exerted by the Bernoulli gripper is obtained by solving a finite element model of the thin wafer created in the ABAQUS® Standard software.

4.2.3.1 Model Geometry

The following two types of multi-crystalline PV silicon wafers are considered here: 125 mm x 125 mm 256 μm cast silicon wafers and 100 mm x 100 mm 180 μm Edge-defined Film-fed Growth (EFG) silicon wafers [2]. Each wafer is modeled as a plate of uniform thickness free of any residual stress. Thin shell elements (S4, 4-node general purpose shell element for finite strains) are used to capture the effects of the large deformation exhibited by the thin wafer. Because of the large deformation, a nonlinear

analysis is necessary to obtain accurate results since membrane effects cause some of the load to be carried by membrane action rather than by pure bending alone. Consequently, the wafer tends to stiffen. In addition, the pressure loading, which is always normal to the undeformed wafer surface, starts to have a component in the in-plane directions as the wafer deforms. The nonlinear analysis includes the effects of wafer stiffening and the changing direction of the pressure relative to the wafer surface while neither of these effects is included in a linear analysis. As plotted in Figure 4.4, the difference between the linear and nonlinear analyses is sufficiently large to indicate that a linear simulation is not adequate for these wafers under the loading conditions considered here. As far as model symmetry is concerned, even if the loading and wafer geometry could lead to a ¼ symmetric model, a full 3-D wafer deformation model is necessary because of the non-symmetry in material properties (e.g. anisotropy of the EFG silicon wafers) and because of the geometric errors in the actual locations of the rubber pads in the gripper.

4.2.3.2 Material Properties

Both PV wafer types are assumed to be linearly elastic. The multi-crystalline silicon cast wafer is assumed to be isotropic and the following material properties reported in the literature [50] are used to model it: Young's modulus, E=162.5 GPa, and Poisson ratio, υ=0.223. Although multi-crystalline in nature, the EFG silicon wafer is known to have a predominant grain orientation due to the wafer growth process. Specifically, it is mostly characterized by a {110} surface and a <112> growth direction [65]. Consequently, anisotropic material properties are specified for this wafer by using the stiffness matrix defined in the wafer coordinate system (x, y, z) [64]. The stiffness coefficients are obtained from the known compliance coefficients for a single cubic silicon crystal with respect to the crystal coordinate system (x', y', z'). Stiffness is

specified using the (110) single crystal properties taking $[1\bar{1}2]$, $[\bar{1}11]$ and [110] orientations as the *x*, *y* and *z* axes. The resulting elastic stiffness matrix for the EFG wafer (in GPa) is given as:

$$C_{ijkl}^{EFG} = \begin{pmatrix} 203.85 & 44.83 & 44.83 & 0 & 0 & 0 \\ & 194.30 & 54.38 & -13.51 & 0 & 0 \\ & & 194.30 & 13.51 & 0 & 0 \\ & & & 60.40 & 0 & 0 \\ & & & & 60.40 & 13.51 \\ & sym & & & & 69.96 \end{pmatrix} \tag{4.1}$$

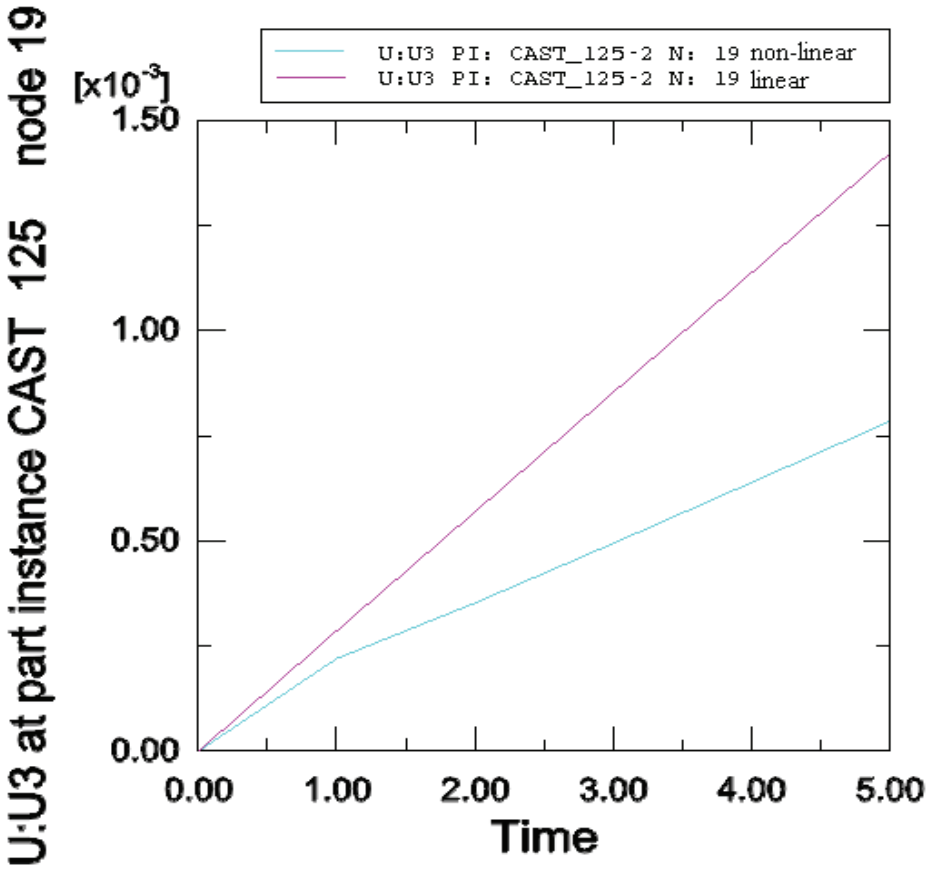

Figure 4.4: Influence of geometric non-linearity on the out-of-plane displacement (cast silicon wafer, *V*=40 l/min, converged solution)

4.2.3.3 Loading and Boundary Conditions

The boundary conditions consist of zero out-of-plane displacements (U_z=0) at the points where the wafer contacts the rubber pads on the gripper. These locations were measured experimentally and are listed in Table 4.1 with respect to the center of the gripper in the *x*, *y*, *z* coordinate system. Also, in-plane wafer displacements were not restrained except for the center node of the wafer that was pinned (U_x=U_y=0) to prevent rigid body motion of the wafer. Note that there are no frictional constraints imposed at these contacts in the current model. The force acting on the wafer is modeled using the radial air pressure distribution obtained from the CFD model presented earlier. A Fortran® subroutine (DLOAD) was used to input the magnitudes of the radial non-uniform air pressure distribution imposed on the top surface of the wafer at the center of all shell elements. For ease of implementation, a piecewise polynomial regression fit was made to the radial air pressure distribution predicted by the CFD model to obtain a smooth, continuous and well-defined curve. A good fit (R-squared ~ 1) was obtained using a third order polynomial as shown in Figure 4.5. Using the polynomial fit also allowed easy determination of the pressure loads imposed on the finite element nodes. The pressure load was ramped linearly in five increments of 20% each.

Table 4.1: Boundary conditions specification (mm)

Boundary conditions	**Location (*x*, *y*)**	**Value**
Locators	(-33.80, 34.66), (34.40, 34.95), (34.05, -34.15), (-34.70, -34.10)	• $U_z = 0$
Center	(0,0)	• $U_x = U_y = 0$

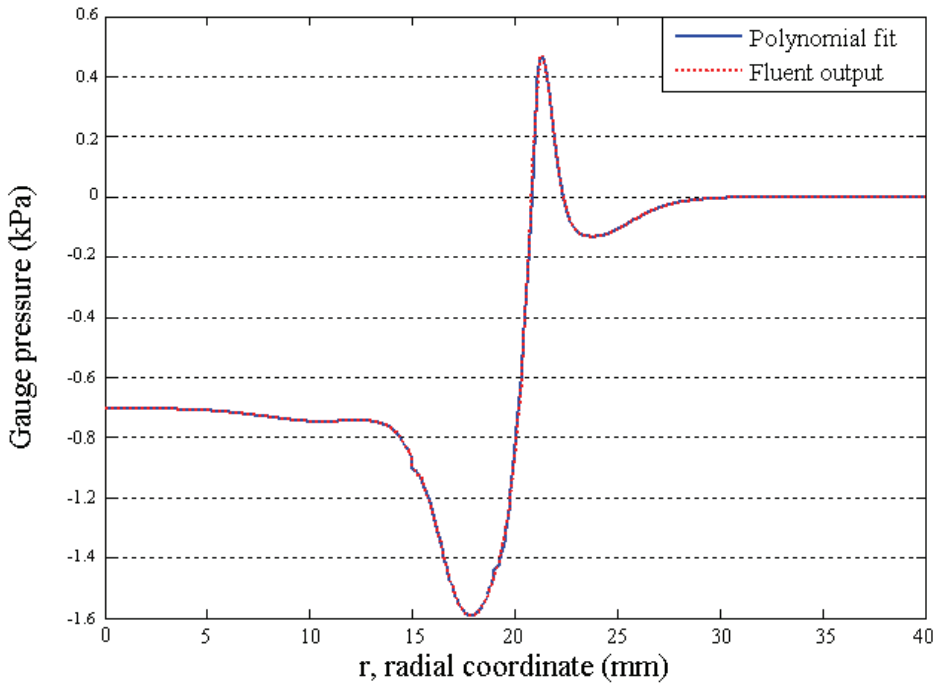

Figure 4.5: Predicted radial air pressure distribution and corresponding polynomial fit

4.2.3.4 Mesh Convergence

The finite element meshes employed for the different wafer types are shown in Figure 4.6. Four node quadrilateral shells elements were used to define the 2-D structured grid. Due to the simple geometry, the aspect ratio of the elements was checked and was found to be adequate. An important factor related to the quality of finite element simulations is the quality of the computational grid. In the actual model, the accuracy of the pressure loading depends on the grid size. The pressure being fixed at every shell center, the resolution of the grid needs to be fine enough to account for the variation in pressure on the wafer surface. Consequently, an analysis of grid independence was performed. The sensitivity of the results to the grid resolution was tested for the computed displacements and stresses for ten different grids per wafer type. The number

of shell elements was refined iteratively by reducing the seed size to obtain reliable results. Table 4.2 shows the number of quadrilateral shell elements, *N*, with respect to the seed size. The different computational grids were compared to the finest mesh solution. The predicted out-of-plane displacement and the stress in the y direction (vertical direction) generated by the gripper on the top surface at the center node of the handled wafer are plotted as a function of the number of shell elements used in the models in Figure 4.7 and Figure 4.8, respectively. The relative error of the predicted values compared to the finest mesh solution is also plotted as a function of the number of shell elements. It can be seen that the relative change in the predicted stress between the three finest grid models is less than 0.2 %. Therefore, a mesh corresponding to 2.5 mm seed size is considered adequate to obtain grid independent results with less than 1% variation compared to the finest grid. The simulation times for these models are reasonable (less than 1 hour on a single Pentium 2.8 GHz processor machine).

Table 4.2: Computational grids used for grid independence check and corresponding number of elements (*N*)

Seed Size (mm)	0.5	0.75	1	1.5	2	2.5	3	4	5	6
N (EFG wafer)	40000	17556	10000	4422	2500	1600	1122	576	400	256
N (Cast wafer)	62500	27556	15500	6972	3844	2500	1764	992	576	400

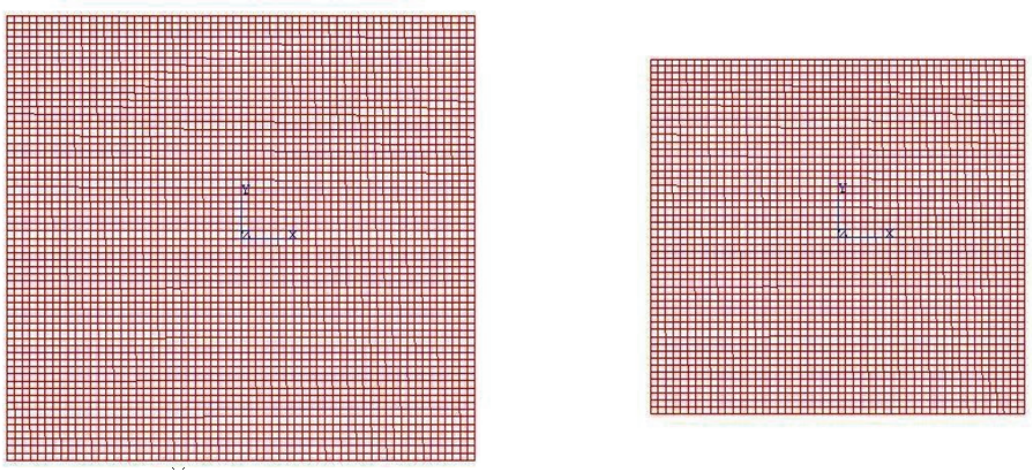

Figure 4.6: Mesh for the different wafer types with 2mm seed size: (a) Cast wafer, (b) EFG wafer

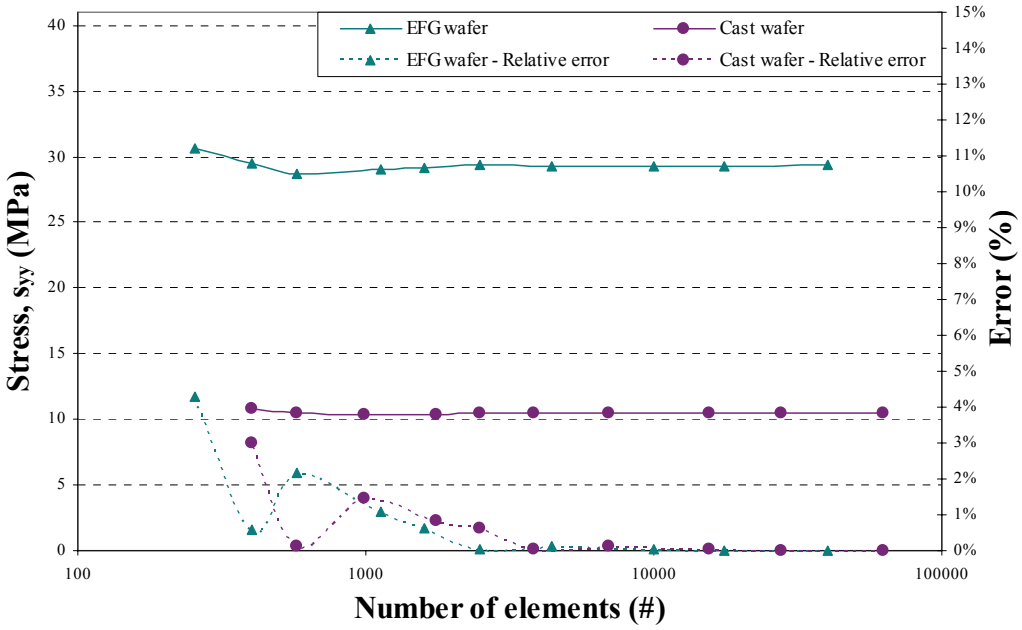

Figure 4.7: Center node displacement, $\delta(0,0)$ as a function of the number of shell elements used in the different models (M=2 g/s)

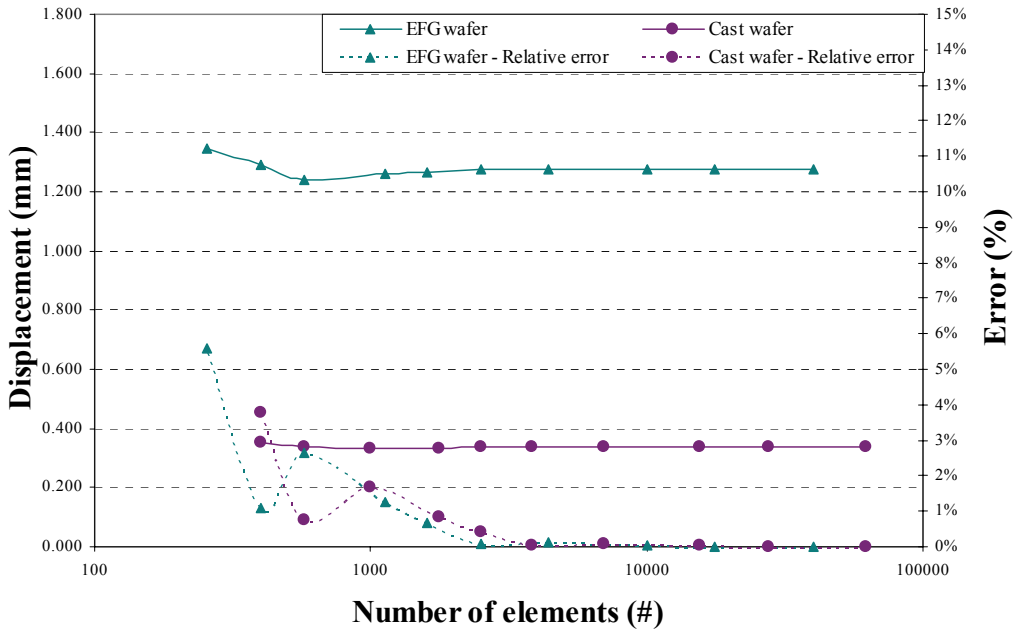

Figure 4.8: Total stress value, s_{yy}, at the center on the top surface of the wafer as a function of the number of shell elements used in the different models (M=2 g/s)

4.3 Model Validation

4.3.1 Experimental Procedure

The experimental setup used to validate the foregoing modeling and analysis approach consists of a 4-axis Adept® SCARA robot equipped with a Bernoulli gripper. The setup has an airflow controller (OMEGA FMA-2610A) to enable precise monitoring and control of the volumetric flow rates, mass flow rates and temperature of the air going into the gripper. The setup also has a laser displacement sensor (Micro-Epsilon OptoNCDT 1700) to measure the shape of the deformed wafer held in the gripper.

The full-field wafer deformation measurement procedure using the laser-based sensor is as follows. For a specified airflow rate and nominal wafer stand-off distance (determined by the height of the rubber pads), the robot scans the gripped wafer along a

specified grid path while the laser sensor measures the wafer deformation. Both the robot location and wafer deformation are recorded simultaneously at each point in the measurement grid. Once the scanning is complete, the heights of the four rubber pads on the Bernoulli gripper are measured and a least-squares reference plane is calculated using the pad heights. Thereafter, the full-field wafer deformation with respect to the least-squares plane is obtained from the laser scanned data. The scanning procedure described above was applied to the two silicon wafer types referred to earlier. The wafer characteristics, number of wafers, and scan grid size used are listed in Table 4.3. Note that the average wafer thickness was estimated from weight measurements. The wafers used in the tests were as supplied by the wafer manufacturers and included some etching to remove surface damage resulting from wire sawing/laser cutting operations. The volumetric airflow rate in each test was varied from 30 to 40 liters/min similar to the tests reported in the previous chapter. The wafer stand-off distance between the gripper and the wafer, H, was initially fixed at 2 mm by adjusting the heights of the rubber pads at 40 l/min. Due to the compliance of the rubber pads, these heights decrease with increasing air flow rate. Up to 10% variation of the stand-off distance was found in the experiments. Consequently, the actual stand-off distance was measured for every run by comparing the heights of the rubber pads to a least-squares plane fit to the gripper surface. The measured response consisted of the full-field wafer deformation from which the maximum wafer deformation could be easily extracted. For every run, the actual stand-off distance at the location of the rubber pads was determined from the laser scans. Table 4.4 lists the average temperature, T_{ave}, and mass flow rate, M_{ave}, measured by the air flow controller for the different volumetric air flow rates, V_{set}.

Table 4.3: Wafer characteristics and scan grid spacing specification

Wafer Type	Size	Average Thickness (μm)	# Samples	Grid Spacing (mm)
Cast wafer	125 mm x 125 mm	256.5 ± 0.5	5	1.5
EFG wafer	100 mm x 100 mm	179.6 ± 1.9	5	1.5

Table 4.4: Average measured air flow characteristics at different air flow rates

V_{set} (l/min)	T_{ave} (ºC)	M_{ave} (g/s)
30	28.3	1.14
35	27.0	1.74
40	25.6	2.74

4.3.2 Experimental Results

Table 4.5 summarizes the experimental results of wafer deformation obtained for each wafer type and airflow rate used. The average measured stand-off distances, H_{ave}, are also listed in Table 4.5 and were used in the CFD fluid simulations. As expected, due to the flexibility of the rubber pads, the stand-off distance decreases with an increase in the air flow rate.

Table 4.5: Average measured stand-off distances and average (δ_{ave}), minimum (δ_{min}) and maximum (δ_{max}) out-of-plane deformation at the center of the wafer as a function of volumetric air flow rate

	V (l/min)	H_{ave} (mm)	$\delta_{ave}(0,0)$ (mm)	$\delta_{min}(0,0)$ (mm)	$\delta_{max}(0,0)$ (mm)
Cast wafer	30	2.131	0.177	0.165	0.203
	35	2.034	0.335	0.312	0.372
	40	1.930	0.799	0.727	0.859
EFG wafer	30	2.259	0.428	0.368	0.521
	35	2.162	1.251	1.077	1.393
	40	2.058	1.769	1.713	1.839

The influence of volumetric airflow rate, V, on the deformation at the wafer center is plotted in Figure 4.9. It is clear from the figure that the maximum deformation increases with airflow rate and, for a given airflow rate, is greatest for the thin EFG wafer. When comparing the error bars for both wafer types, the influence of wafer thickness variation on the wafer deformation is seen to be larger for the EFG wafers than for the cast wafers. Also, the maximum deformation for the EFG wafer appears to be leveling off with increase in airflow rate in contrast to the cast wafer. This is largely a result of the wafer deformation approaching the maximum displacement permitted by the gripper geometry and is a function of the stand-off distance defined by the rubber pads. Another factor that contributes to the leveling of wafer deformation, especially at high air flow rates when the top surface of the deformed wafer approaches the gripper surface, is the effect of direct air impingement on the wafer around the cone mill (see Figure 4.1) This positive pressure on the wafer surface moderates the effect of the negative gauge air pressure (or vacuum) created by the radially diverging air flow.

Figures 4.10 and 4.11 show the influence of volumetric airflow rate on the full-field wafer deformation contours for the cast and EFG wafers, respectively. The

deformation contours in these figures yield similar conclusions to those derived from Figure 8. In addition, one can see that for both wafer types there is a preferred orientation of deformation (bending about the horizontal axis) as the airflow rate is increased. Material anisotropy cannot explain this preferred orientation since it appears to be the more or less the same for both wafer types, which are inherently different in their mechanical properties. Careful analysis of the gripper geometry shows that the preferred orientation is due to small errors in the actual location of the rubber pads. If the rubber pads were symmetrically located around the center of the gripper, a more or less symmetric deformation profile would be obtained (perfectly symmetric deformation profile would be obtained only if the wafer is round and is isotropic). The errors in the pad locations lead to differences in the moment arms and consequently a reversed U-shape deformation pattern is obtained at high flow rates. For this reason, the actual location of the rubber pads was included in the finite element model. Note that although wafer deformation is not axi-symmetric in all the cases analyzed, for computational efficiency of the CFD model it was assumed that the wafer deformation is indeed axi-symmetric and that the moving boundary condition representing the wafer deformation can be modeled using the average wafer deformation along the *y*-axis. The deformation along the *y*-direction was used because it is more axi-symmetric than along the *x*-direction. In addition, the wafer deformation along the *x*-axis is generally greater than along any other direction. Consequently, the actual air gap between the deformed wafer and the gripper is smallest along the *x*-axis, which implies that the air from the nozzle will have a natural tendency to flow away from the *x*-axis toward the *y*-direction. .

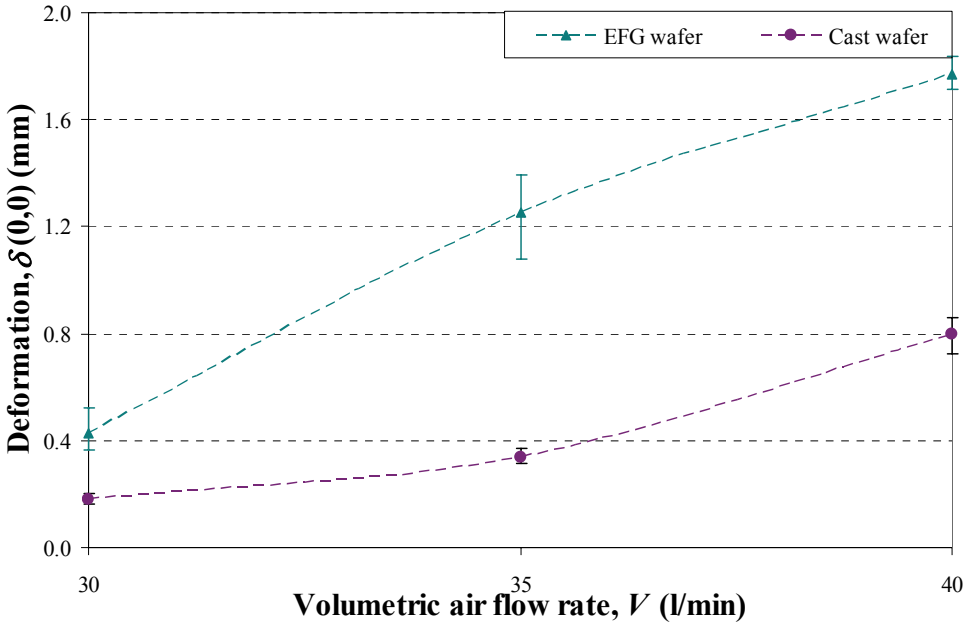

Figure 4.9: Influence of volumetric airflow rate on the out-of-plane deformation at the center of the wafer; the error bars represent the data range (for 5 samples)

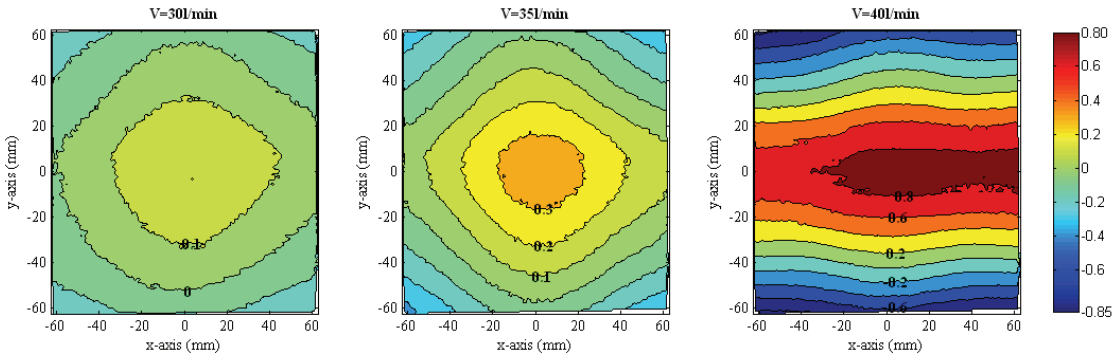

Figure 4.10: Full-field measured out-of-plane deformation (in mm) as a function of airflow rate for cast silicon wafer

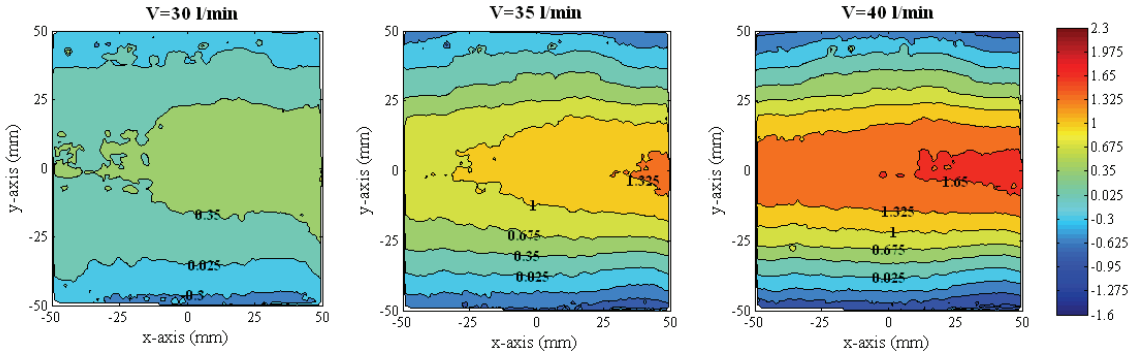

Figure 4.11: Full-field measured out-of-plane deformation (in mm) as a function of airflow rate for EFG silicon wafer

4.3.3 Modeling Results and Validation

The iterative procedure outlined in Figure 4.2 was found to typically converge in a few iterations. Figure 4.12 shows the convergence of the maximum out-of-plane wafer deformation for the cast silicon wafer. Only four iterations were needed for the iterations to converge with less than 1% difference.

Comparing the measured wafer deformation for each wafer type and airflow rate with the predicted equilibrium wafer deformation enables the validation of the iterative

modeling procedure presented in Figure 4.2. Note that, unlike the rigid wafer case [17, 72] it is not feasible to measure the radial air pressure distribution between the wafer and gripper in the presence of wafer deformation and consequently model validation requires comparison of predicted and measured wafer deformations.

Table 4.7 presents a comparison of the model predicted versus experimental results. The measured average out-of plane displacement at the center of the wafer, $\delta_{ave}(0,0)$, is compared with the predicted deformation at the wafer center obtained in the first ($\delta_{initial}(0,0)$) and final ($\delta_{final}(0,0)$) iterations, where the result for the final iteration step is the predicted equilibrium wafer deformation. Note that the wafer deformations are referenced to the mid-plane of the wafer. In addition, the number of iterations, Niter, needed to obtain less than 2% variation is specified.

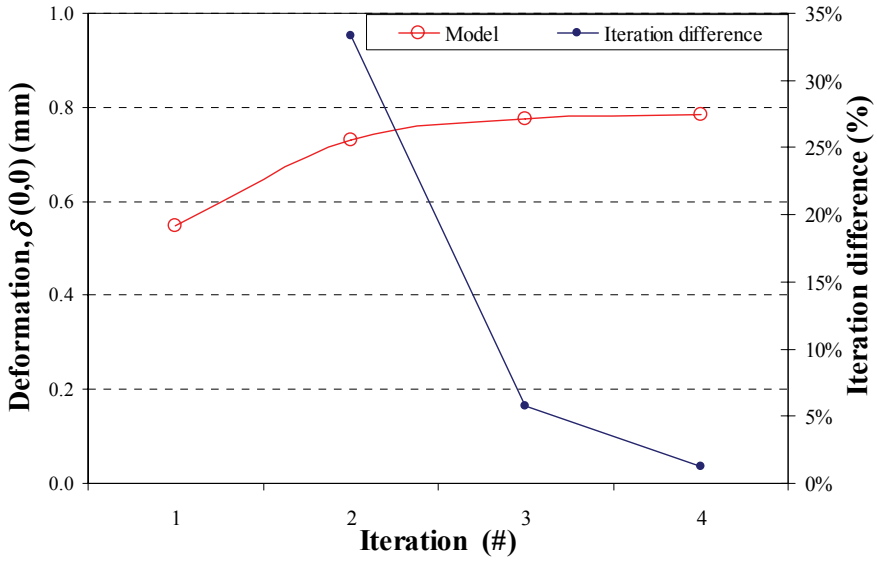

Figure 4.12: Convergence of the iterative approach (cast silicon wafer at V=40 l/min)

Table 4.6: Comparison of measured and predicted average out-of-plane deformations at the center of the wafer as a function of the volumetric air flow rate (result obtained in the first iteration is denoted as $\delta_{initial}$)

	V (l/min)	$\delta_{ave}(0,0)$ (mm)	$\delta_{initial}(0,0)$ (mm)	$\delta_{final}(0,0)$ (mm)	N_{iter} (#)
Cast wafer	30	0.177	0.169	0.169	2
	35	0.335	0.298	0.314	3
	40	0.799	0.549	0.784	5
EFG wafer	30	0.428	0.433	0.477	3
	35	1.251	0.916	1.480	5
	40	1.769	1.945	2.023	3

Figure 4.13 shows a comparison of the measured and predicted out-of plane deformations at the center of the wafer for the cast silicon wafer. Note that for the results for the initial iteration and the converged solution are both shown in the figure. It is clear that the iterative solution for the cast wafer is in very good agreement with the measured deformation at all airflow rates (relative errors < 7%). It can be seen from the figure (and table) that the effect of substrate flexibility on the equilibrium wafer deformation is significant at higher airflow rates while it is small at low airflow rates. The results for the cast silicon wafer also show that even though wafer deformation is not symmetric at high flow rates, the assumption of symmetry of the wafer deformation profile in the CFD model still yields good results.

Similarly, Figure 4.14 shows a comparison of the measured and predicted maximum out-of plane deformations for the EFG wafers. Although the iterative solution for the EFG silicon wafer is seen to over-predict the deformation, the model captures the experimentally observed trends. Specifically, the experimental data reveals a leveling tendency with increase in the airflow rate, which is captured in the model predictions.

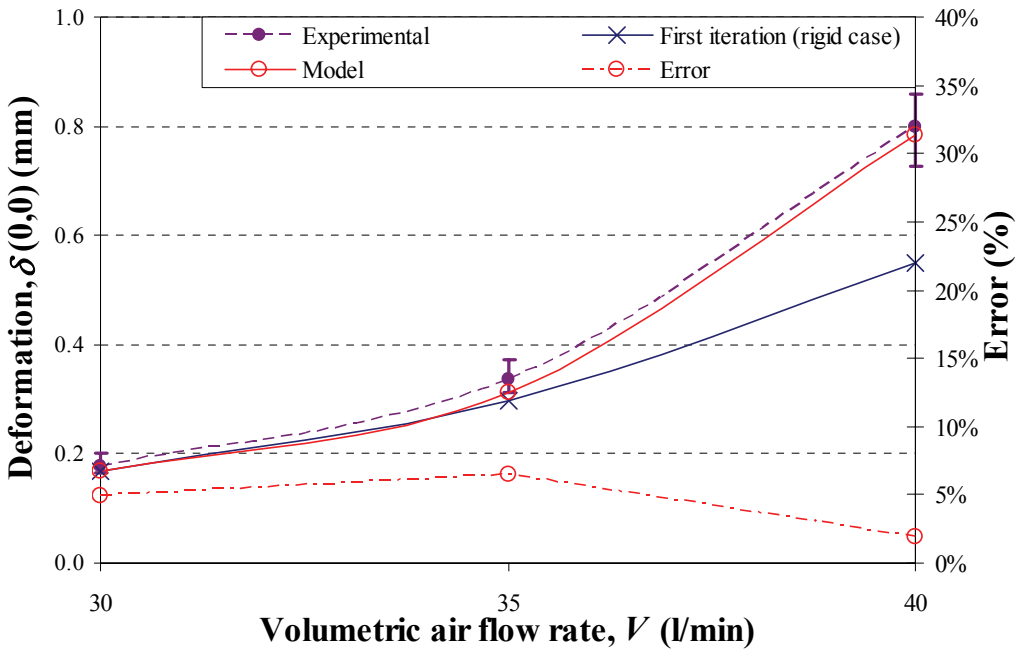

Figure 4.13: Predicted vs. measured out-of-plane deformation at the center of the wafer, $\delta(0,0)$, for cast silicon wafer as a function of airflow rate

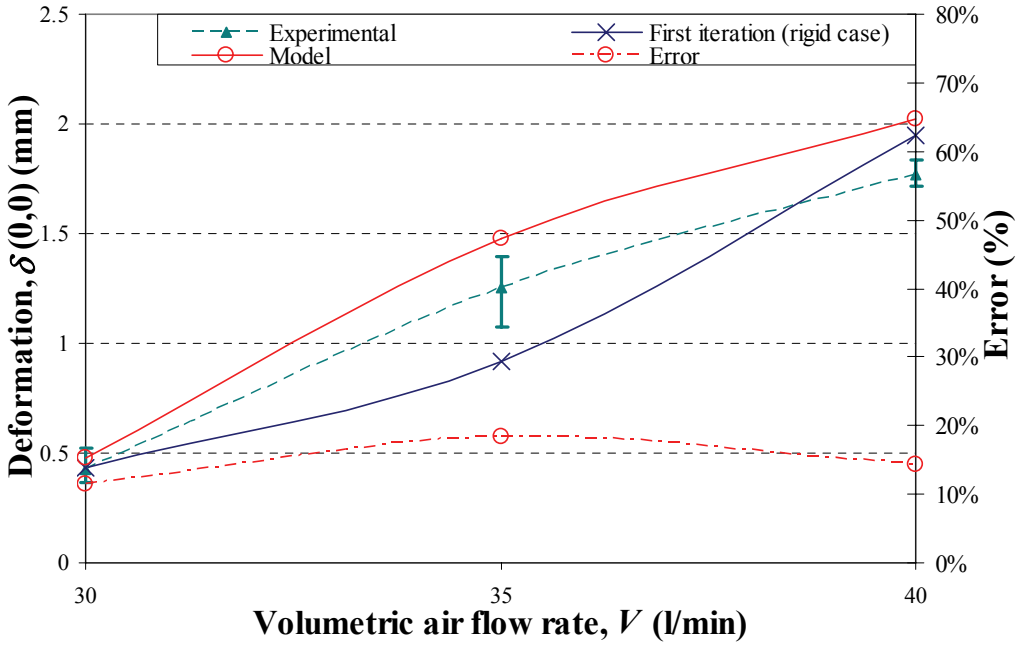

Figure 4.14: Predicted vs. measured out-of-plane deformations at the center of the wafer, $\delta(0,0)$, for EFG silicon wafers as a function of airflow rate

Note that this leveling tendency was earlier attributed to the constraints imposed on the maximum wafer deformation by the gripper geometry and the influence of positive air pressure on the top surface of the wafer due to direct air impingement. It is evident from the figure that not accounting for the effect of wafer deformation on the pressure distribution does not result in the leveling trend observed in the test data (see curve for "first iteration" in Figure 4.14). As the out-of-plane displacement at the center of the wafer approaches the set stand-off distance with increasing airflow rate, the influence of wafer deformation on the pressure is reduced due to the direct impingement of air on the wafer and this causes the leveling-off effect.

It is believed that over-prediction of the iterative model for EFG wafers is due to the assumed axis-symmetry of wafer deformation in the CFD model. Since the EFG wafer deformation profile along the y-axis is used in the CFD model and it is evident from Figure 4.11 that the variation in wafer deformation along the x-direction is far less than in the y-direction, the effect of direct air impingement on wafer deformation is actually more than the model accounts for. Consequently, the model predicts a higher deformation than observed in the experiment. Note that this was not observed in the cast silicon wafer case because the maximum deformation of the cast wafer was only about 0.8 mm compared to the 2 mm stand-off distance set by the rubber pads. Whereas the EFG wafer deforms much more and is a lot closer to the gripper surface thereby enhancing the effect of air impingement and moderating the resulting wafer deformation. Accounting for the non-symmetric behavior of wafer deformation in the CFD model would require a computationally intensive 3-D model due to the fact that actual gripper used in this work has some inherent geometric imperfections. Nevertheless, the worst-case prediction errors for the EFG silicon wafer are less than 20%.

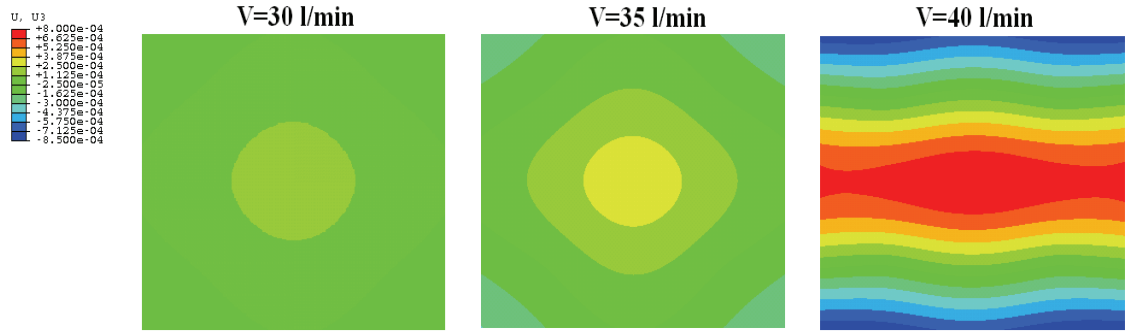

Figure 4.15: Full-field predicted out-of-plane deformation, δ, (m) as a function of volumetric air flow rate for cast silicon wafer

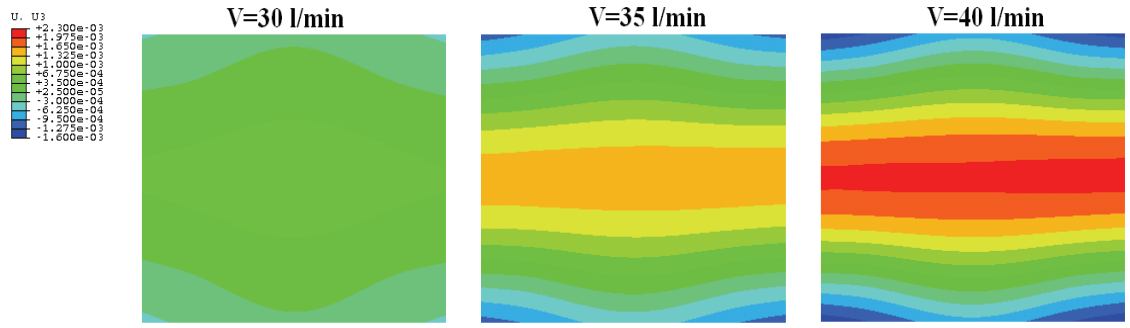

Figure 4.16: Full-field predicted out-of-plane deformation, δ, (m) as a function of volumetric air flow rate for EFG silicon wafer

Figures 4.15 and 4.16 show the influence of volumetric air flow rate on the predicted full-field wafer deformation obtained from the iterative approach for the cast and EFG silicon wafers, respectively. When compared to the measured full-field deformations shown in Figures 4.10 and 4.11, a fairly good agreement is observed in the deformation patterns as far as the overall trends are concerned. In particular, almost symmetric deformation behavior is observed at 30 l/min and 35 l/min airflow rates for the cast wafer. In addition, the reversed U-shape pattern evident in the measured contours at higher airflow rates is also captured in the predictions. This confirms that the errors in the

location of the rubber pads (accounted for in the finite element model) are the primary cause of the non-symmetric deformation patterns.

4.3.4 Effect on Radial Air Pressure Distribution

After validating the iterative modeling procedure presented in Figure 4.2 by comparing the predicted equilibrium wafer deformation with the measured wafer deformation, the influence of substrate flexibility on the radial air pressure distribution generated by the gripper can be analyzed. Figures 4.17 and 4.18 show the predicted radial distribution profiles obtained at 40 l/min for the cast and EFG wafers, respectively. It can be seen in both figures that accounting for substrate deformation lead to a higher vacuum level in the center region of the gripper/wafer. This is explained by the reduction in airflow gap between the gripper surface and wafer when wafer deformation is accounted for in the model. Both figures also reveal a small region of positive pressure due to the direct impingement of air on the wafer surface as the air exits the vertical section of the nozzle near the cone mill. Note also that for the cast wafer (Figure 4.17), which experiences smaller deformation compared to the thinner EFG wafer, the angle of impingement of air exiting the nozzle near the cone mill, measured relative to the wafer surface normal, increases as the wafer deforms and this yields a lower force component normal to the wafer surface. In contrast, for the EFG wafer, which undergoes much larger deformation and therefore is closer to the gripper surface at equilibrium, the angle of impingement of air on the wafer surface is greater leading to a higher positive pressure peak relative to the cast wafer as well as to the EFG wafer when not considering the influence of wafer deformation (see Figure 4.18). In addition, notice that there is a shift in the location of the positive air pressure toward the center of the gripper when the effect of

wafer deformation is included. This radial shift is not captured when substrate flexibility is not accounted for in the model.

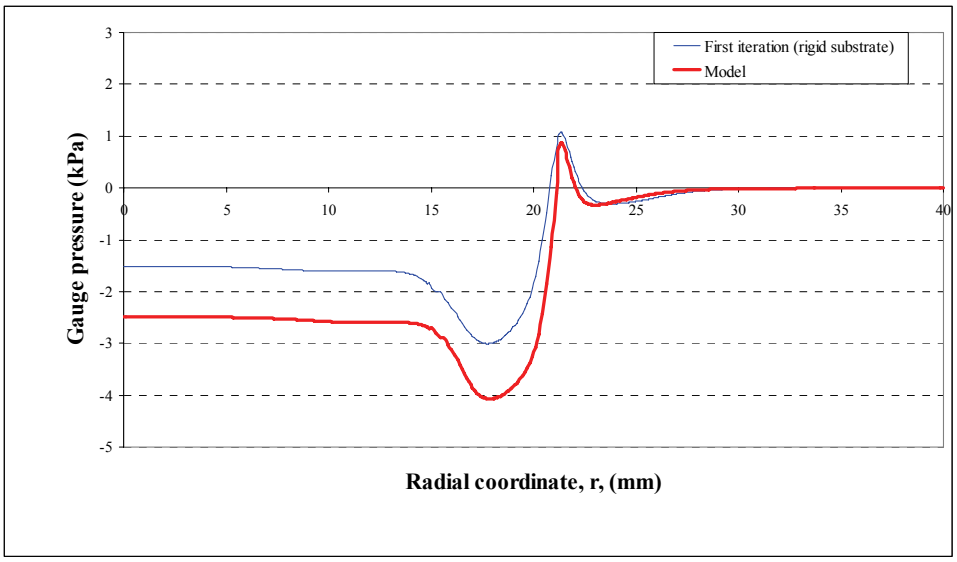

Figure 4.17: Effect of wafer deformation on the predicted air pressure distribution for cast silicon wafer at V=40 l/min

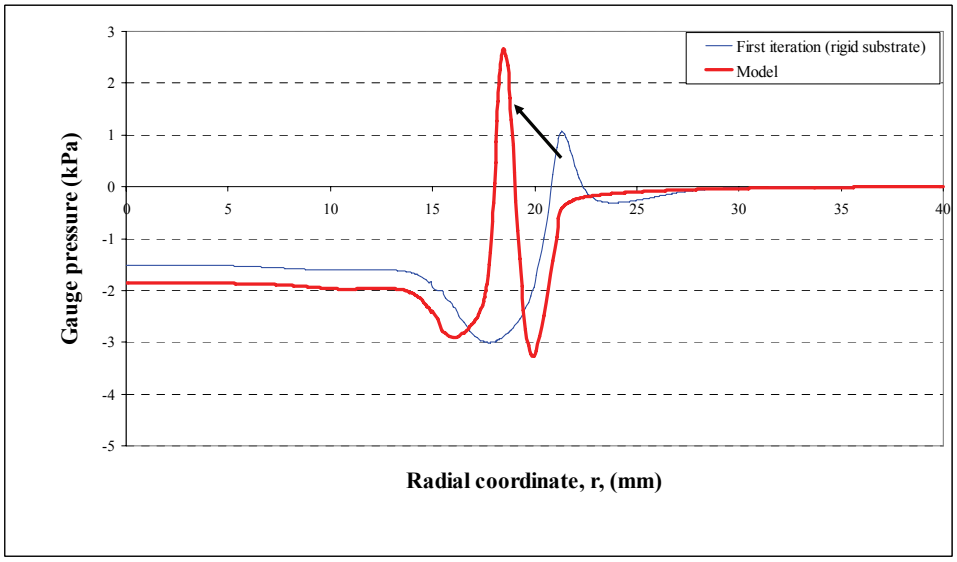

Figure 4.18: Effect of wafer deformation on the predicted pressure distribution for EFG silicon wafer at V=40 l/min

4.3.5 Effect on the Lifting Force

The influence of wafer flexibility on the lifting force can also be evaluated by comparing the rigid substrate solution, represented by the first iteration solution, and the final equilibrium solution. Table 4.8 lists the lifting force obtained as a function of the volumetric airflow rate. These results are also plotted in Figures 4.19 and 4.20 for the cast and EFG wafers, respectively. For all cases, accounting for wafer flexibility leads to an increase in the lifting force. As mentioned earlier, the reduction in the airflow height due to wafer deformation generates higher vacuum levels and consequently an increase in the lifting force. For the cast silicon wafer (Figure 4.19), the effect of wafer deformation on the lifting force is absent at the lowest airflow rate of 30 l/min but increases with airflow rate to become quite significant at 40 l/min. In contrast, for the thinner EFG silicon wafer (see Figure 4.20), the effect of wafer deformation on the lifting force increases significantly with an increase in the airflow rate from 30 to 35 l/min and then decreases significantly at 40 l/min. This is due to the greater counteracting influence of the direct air impingement on the wafer surface, which is higher for the EFG wafer because it undergoes much larger deformation than the cast wafer and is closer to the nozzle exit near the cone mill. This is confirmed by looking at the results for the radial air pressure distribution in Figure 4.18.

Table 4.7: Predicted lifting force as a function of the volumetric air flow rate (the rigid substrate solution is denoted by $F_{initial}$)

	V (l/min)	$F_{initial}$ (N)	F_{final} (N)	Flexibility influence (%)
Cast wafer	30	0.56	0.56	0
	35	1.25	1.36	8
	40	2.74	4.01	32
EFG wafer	30	0.56	0.62	11
	35	1.25	2.05	39
	40	2.74	2.79	2

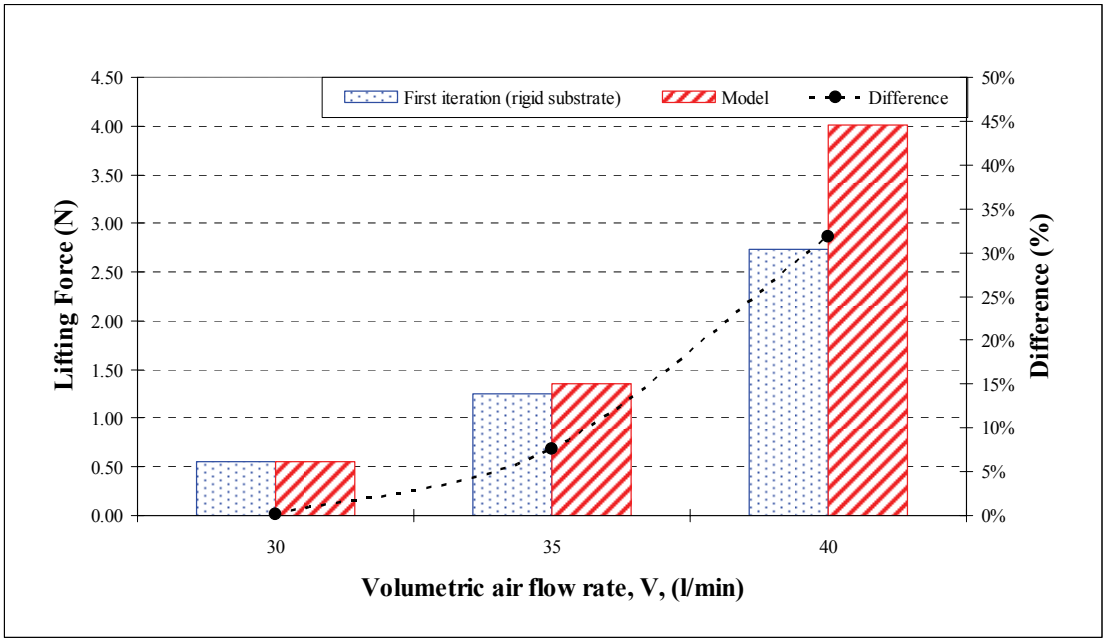

Figure 4.19: Predicted lifting force as a function of the volumetric air flow rate for cast silicon wafer

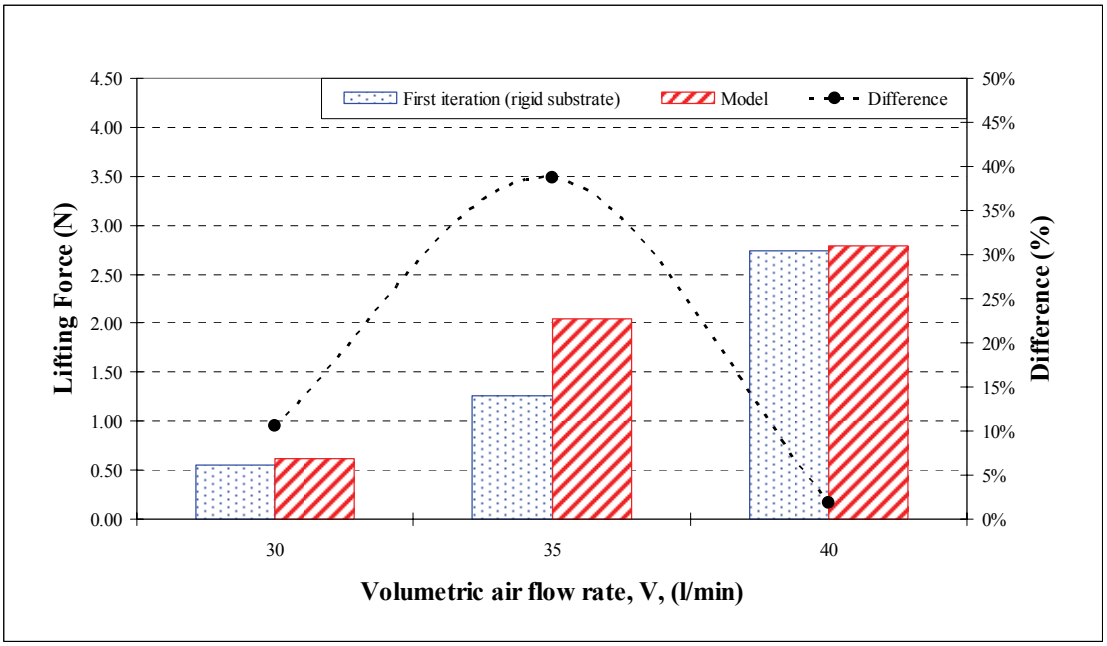

Figure 4.20: Predicted lifting force as a function of the volumetric air flow rate for EFG silicon wafer

4.3.6 Effect on the Handling Stresses

The influence of wafer flexibility on the handling stresses can also be evaluated by comparing the rigid substrate solution, represented by the first iteration solution, and the final equilibrium solution. The stresses are obtained from the finite element model. In particular, it is the tensile stress generated in the wafer during handling that is of interest from a standpoint of wafer breakage. Since the maximum tensile stress is produced in the top surface of the wafer during Bernoulli gripping, the handling stresses on this surface of the wafer are analyzed here. Table 4.9 lists the maximum in-plane principal stress, which is tensile, is obtained from the center of the top surface of the wafer as a function of the volumetric airflow rate. These results are also plotted in Figures 4.21 and 4.22 for the cast and EFG wafers, respectively. For all cases, accounting for wafer flexibility leads to an

increase in the maximum in-plane principal stress. As expected, there is an increase in the magnitude of the stress with increasing wafer deformation. But at the highest airflow rate the counteracting influence of direct impingement of air on the wafer reduces the effect of wafer deformation on the handling stress. This is especially evident for the thin EFG wafer as seen in Figure 4.22

Table 4.8: Predicted maximum in-plane stress at the center of the wafer as a function of the volumetric air flow rate

	V (l/min)	$\sigma_{initial}(0,0)$ (mm)	$\sigma_{final}(0,0)$ (mm)	Flexibility influence (%)
Cast wafer	30	7.0	7.1	1%
	35	12.9	13.7	6%
	40	27.6	40.2	31%
EFG wafer	30	11.9	13.5	11%
	35	26.6	43.7	39%
	40	53.2	60.2	12%

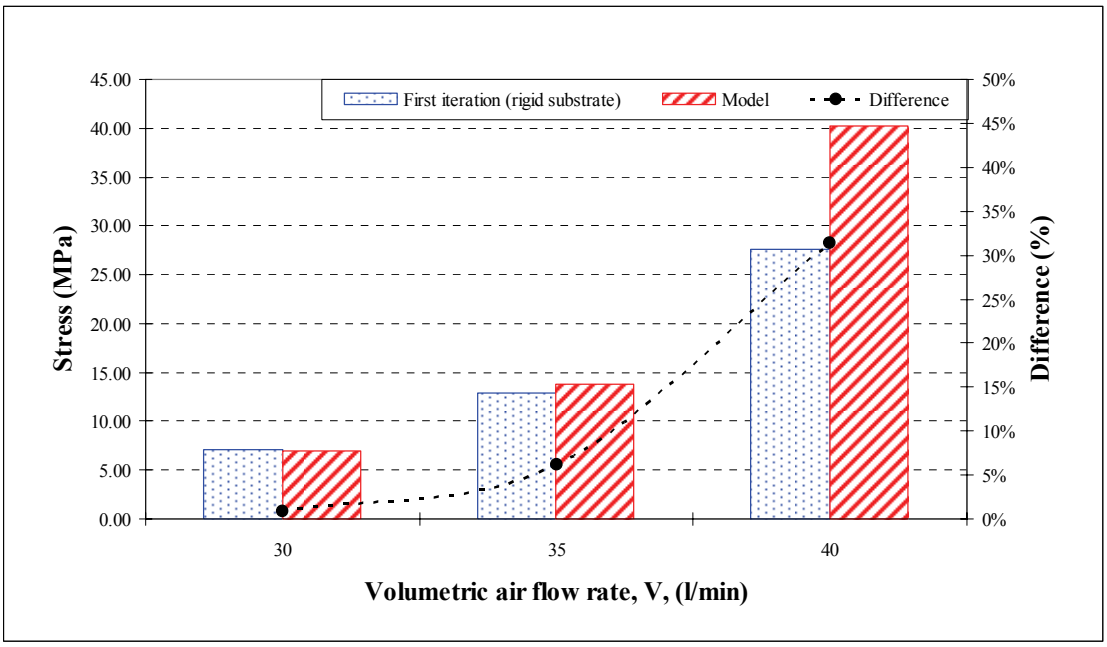

Figure 4.21: Predicted maximum in-plane principal stress for cast silicon wafer at the center of the wafer top surface as a function of the volumetric airflow rate

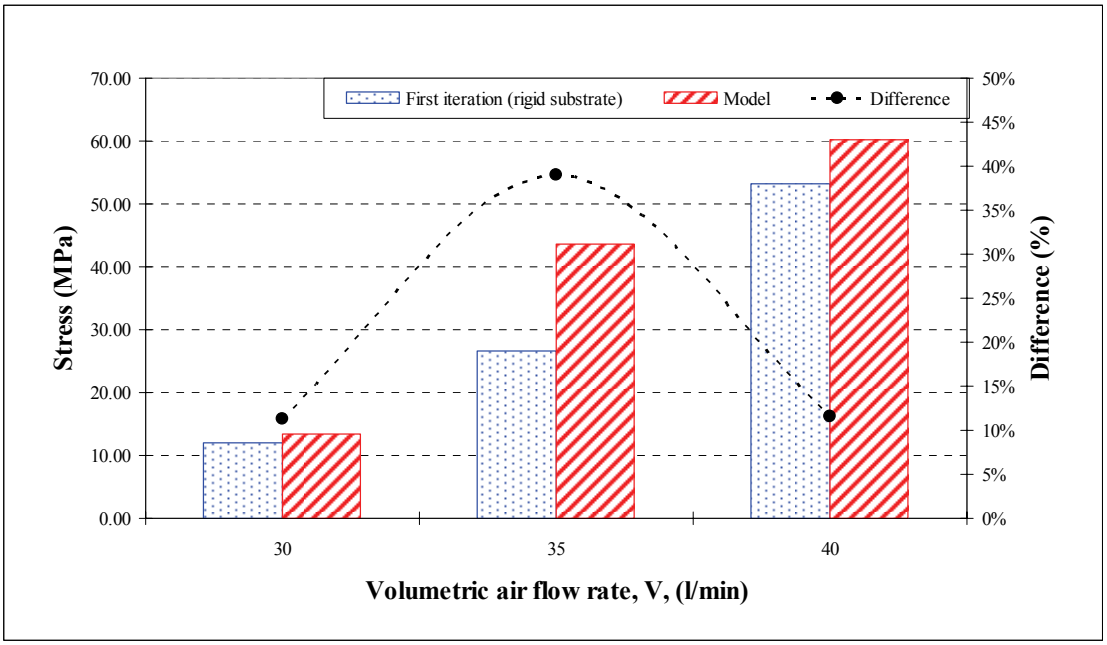

Figure 4.22: Predicted maximum in-plane principal stress for EFG silicon wafer at the center of the wafer top surface as a function of the volumetric airflow rate

Figures 4.23 and 4.24 show the maximum in-plane principal stress distribution as a function of the volumetric airflow rate for the cast and EFG wafers, respectively. It can be clearly seen from the figures that an increase in the airflow rate leads to an overall increase in the magnitude of the stresses everywhere. In addition, the location of the maximum in-plane principal tensile stress tends to shifts from the center of the wafer to the edge with an increase in the airflow rate. This change in location is due to the preferred orientation of wafer deformation resulting from the imperfections in the gripper geometry and more specifically to the differences in the location of the rubber pads. Note the presence of compressive stresses at the locations of the rubber pads. It is likely that the magnitude of these compressive stresses is somewhat over-predicted because of the boundary conditions used to model the locators (see Table 4.1). A more accurate model of the contact between the rubber pads and the wafer would require accounting for

friction at the interface. However, it is argued here that the effect of the boundary conditions used here is localized and does not influence the overall stress distribution significantly. Alternatively, the obtained wafer deformation profile could be used as a boundary condition to predict the stresses. This approach is presented in the next chapter, albeit using the measured wafer deformation profile instead of the predicted deformation profile to evaluate the total stress state generated in the wafer during handling. A comparison of the stress distributions shown in Figures 4.23 and 4.24 with the corresponding *total stress states* obtained in the next chapter (Figures 5.9 and 5.10) reveals several similarities. Note that an exact comparison cannot be made because the influence of the residual stress that is included in the total stress state.

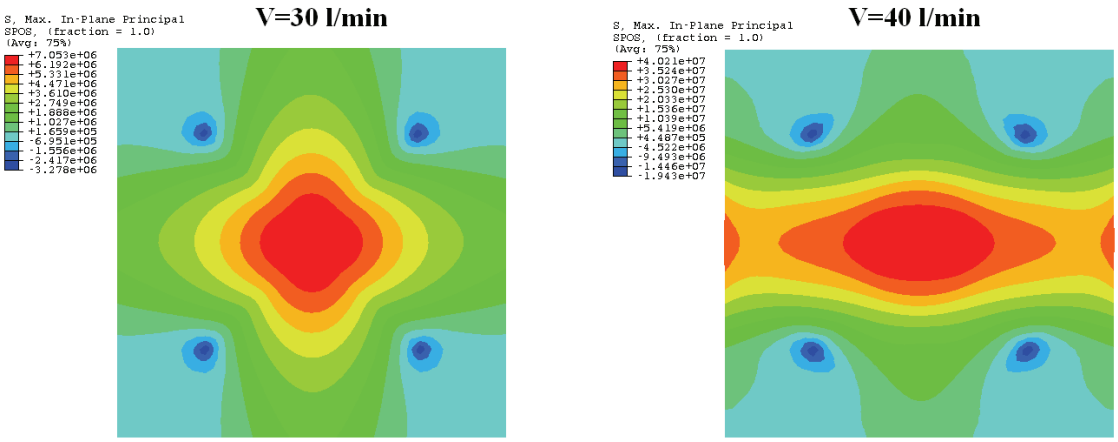

Figure 4.23: Influence of the airflow rate on the predicted maximum in-plane principal stress distribution on the top surface for cast silicon wafer

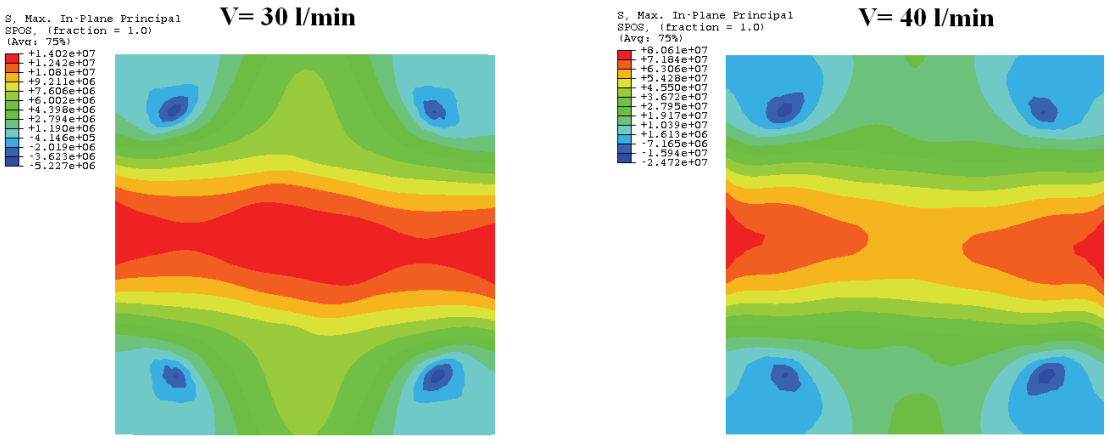

Figure 4.24: Influence of the airflow rate on the predicted maximum in-plane principal stress distribution on the top surface for the EFG silicon wafer

4.4 Summary

This chapter presented the modeling and analysis of the effect of substrate flexibility, and hence deformation, on the equilibrium radial air pressure distribution and lifting force generated by a Bernoulli gripper with a cone mill. An iterative fluid-structure interaction model developed using CFD and the finite element method was solved in order to elucidate the effects of substrate deformation. The model was analyzed and experimentally verified for Bernoulli handling of thin crystalline silicon wafers used as substrates in PV solar cell manufacture. The following specific conclusions are derived from this work:

- The modeling approach is shown to yield predictions that are in good agreement with the measured equilibrium wafer deformations for both cast and EFG silicon wafers over a range of volumetric airflow rates. Specifically, prediction errors smaller than 7% were obtained for the cast silicon wafers while a larger average error of around 15% was obtained for the EFG wafers.

- At high airflow rates with the thin EFG wafer, the model was shown to accurately capture the leveling-off trend in the maximum wafer deformation due to the competing effects of low air pressure created by the radially diverging airflow and the direct impingement of air on the wafer surface in the vicinity of the cone mill.
- The effect of substrate/wafer flexibility on the radial air pressure distribution and lifting force was found to be significant at higher volumetric airflow rates for both wafer types. Specifically, up to 32% difference in the predicted lifting force compared to the rigid substrate solution was found for the cast wafers at 40 l/min airflow rate. For the EFG wafers, the maximum influence of wafer flexibility on the lifting force was 39% at 35 l/min. Overall, the effect of wafer deformation on the air pressure is to increase the vacuum level in the center region for both wafer types. For the thinner EFG wafer, the counteracting effect of direct air impingement is significant at the higher airflow rates. A similar effect is predicted for the lifting force and handling stresses.
- It is shown that the airflow rate has a significant effect on the magnitude and distribution of the handling stresses. The magnitude of the maximum in-plane principal stress at the center of the wafer increases by 5.7 times and 4.5 times when going from 30 l/min to 40 l/min airflow rate for the cast wafer and EFG wafers, respectively.
- In addition, a transition in the maximum in-plane principal tensile stress location from the center to the wafer edge is predicted by the model with increase in the air flow rate.

The results obtained from this study can be used to evaluate the lifting force acting on any air impermeable flexible substrate as a function of the gripper variables such as the volumetric airflow rate and stand-off distance. Also, optimization of the gripper design and especially the location of the rubber pads can be carried out to minimize wafer deformation and consequently the handling stresses when handling thin brittle materials such as silicon wafers. This optimization can help to reduce incidents of wafer breakage during wafer handling operations. In the next chapter, an approach to investigate why breakage occurs during handling is presented.

CHAPTER V

ANALYSIS OF STRESSES AND BREAKAGE DURING HANDLING

A significant challenge in using thinner and larger crystalline silicon wafers for solar cell manufacture is the reduced yield due to higher wafer breakage rates. At a given process step, wafer/cell breakage depends on the stresses produced in the wafer/cell due to prior processing, handling and/or transport and on the presence of structural defects such as cracks. Specifically, analysis of wafer breakage requires knowledge of the total in-plane stress state produced in the wafer due to handling and residual stresses from prior processing. The previous chapter presented a modeling approach to evaluate the handling stresses from the handling control variables in the case of a Bernoulli gripper. This chapter presents a systematic approach to breakage analysis of crystalline silicon wafers during handling via analysis of the total stress state produced in the wafer. The total stress state is determined using a combination of wafer deformation measurements and non-linear finite element analysis. This includes the residual stress generated in a prior process step and stresses applied to the wafer/cell by the current process, and handling and/or transport methods used in solar cell manufacture. Knowledge of the total stress state in conjunction with the crack size and location enables the determination of wafer breakage and the associated fracture stress. This approach is experimentally validated through breakage tests performed on EFG wafers with cracks introduced via indentation. The results show that the wafer breakage stress during handling is proportional to the inverse of the square root of the crack length, which is consistent with linear elastic fracture mechanics theory. The work also confirms the capability of the

proposed approach to determine the handling conditions under which wafer breakage will occur.

5.1 Introduction

The recent rise in the cost of silicon (Si) combined with the need to lower the cost of crystalline silicon based solar cells is contributing to the increasing use of thinner and larger wafers. However, a few studies have shown that the use of thinner wafers can lead to unacceptable yields arising from wafer breakage during handling, transport and/or processing [52]. Consequently, it is critical to understand the basics mechanics of wafer breakage [74]. Fundamentally, breakage of Si wafers during processing or handling is due to the propagation of cracks present in the wafer. Knowledge of crack locations and sizes is therefore needed to predict wafer breakage. A few techniques have been developed to detect and quantify cracks in wafers [58-60]. A crack will propagate if a sufficiently large in-plane tensile stress is applied normal to the crack plane (assuming Mode I fracture). Thus, it is necessary to analyze the nature, magnitude and distribution of the total stress state generated in the wafer/cell during handling or processing.

This chapter presents a systematic approach to analyze the mechanical stresses and breakage of Si wafers of various types and thicknesses during automated handling. Although this work focuses specifically on wafer handling using the Bernoulli gripper (described later), the approach is general and applies to all handling methods that induce wafer deformation. The approach relies on a combination of full-field wafer deformation measurements and non-linear finite element analysis to determine the total stress state in the wafer/cell during handling. A detailed analysis of the handling induced stress state in Czochralski (Cz), Cast and Edge-defined Film-fed Growth (EFG) crystalline silicon wafers of different thicknesses is presented. Knowledge of crack location in the wafer

and its size enables the limiting wafer breakage stress to be determined from linear elastic fracture mechanics theory. Breakage experiments on notched EFG wafers are carried out to validate this approach to determine the wafer fracture stress during handling. The relationship between the experimentally obtained crack size and fracture stress is also analyzed. Finally, the relationship between the maximum in-plane tensile stress, the corresponding critical crack length and the likelihood of wafer breakage is also discussed.

5.2 Handling Stresses

As mentioned earlier, the breakage of crystalline Si wafers during solar cell production is a function of the stress applied to the wafer during processing, the residual stress generated in the wafer in prior processing steps, and structural defects such as cracks/micro-cracks. Wafer handling and transport is a process step that induces mechanical stresses in the wafer. Assuming that the principle of linear-elastic superposition of stress holds, the total stress in the wafer can be written as:

$$\sigma_{total} = \sigma_{applied} + \sigma_{residual} \tag{5.1}$$

The applied stress depends on the process and can be mechanical or thermal while the residual stress is the stress present in the wafer after removal of loads applied during the prior process step(s) (e.g. crystal growth, wire-sawing, etc.).

In a handling operation, the applied stress is a function of the handling control variables. Mechanical, vacuum and Bernoulli based wafer handling devices are routinely used in the photovoltaic industry (PV). Of these, the Bernoulli gripper is widely used and because of its “low force” capability it is of particular interest when handling thin Si wafers. A typical Bernoulli gripper is shown schematically in Figure 4.1. The gripper is essentially an air nozzle that produces a suction force on the wafer by means of a radially

diverging decelerating air flow between the gripper and wafer. Generally, Bernoulli grippers are used as non-contact end effectors for "gentle handling" and the stand-off distance from the gripper to the handled object is fixed by equilibrium of the vacuum and the wafer weight [12, 17]. In high throughput PV applications, the Bernoulli gripper often consists of soft rubber pads that determine the stand-off distance. Friction between the wafer and pads enables faster transport speeds. When handling thin wafers (≤ 300 μm), the low pressure created by the radially diverging air flow tends to deform the wafer and generates stresses. The applied stresses are a function of the volumetric air flow rate and the stand-off distance imposed by the pads.

As far as the residual stresses are concerned, in-plane residual stress measurements on Cz, EFG and Cast Si wafers have been reported in the literature [75, 76]. At present however these measurements provide only the average through-thickness residual in-plane shear stress and not the complete residual stress state in the wafer. Hence, it is not yet possible to superpose the stresses as implied by Equation (5.1) and evaluate the relative significance of the residual stress and the applied handling stress.

In the absence of the complete residual stress state in the wafer, experimentally determined full-field wafer deformation measurements can be used to determine the *total stress state* in the wafer via a two step procedure summarized in the flowchart shown in Figure 5.1. The first step involves fitting an analytical surface to the measured wafer deformation data in order to reduce measurement noise. The second step involves calculating the handling stress distribution by solving a non-linear finite element model of the wafer with the fitted analytical surface imposed as a displacement boundary condition. Since the influence of the in-plane residual stress is captured by the out-of-plane wafer deformation, its effect on the total stress in the wafer is implicitly included in

the calculation. A similar approach is used in the Shadow- Moiré technique in [61] to extract the full-field residual stresses. These steps are detailed in the following sections.

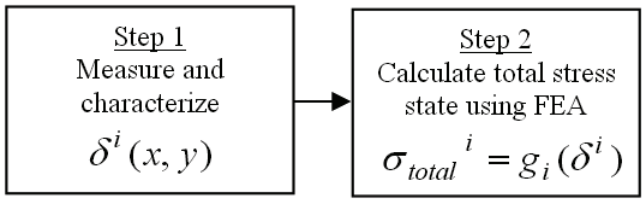

Figure 5.1: Total stress state calculation procedure from measured wafer deformation profiles

5.2.1 Wafer Deformation Measurement

The experimental setup used to measure wafer deformation consists of a 4-axis Adept® SCARA robot equipped with a Bernoulli gripper for wafer pick up and transport (see Figure 5.2). Sensors used in the setup include an air flow controller (OMEGA FMA-2610A) to measure and control the volumetric air flow rate in the gripper and a laser-based wafer deformation measurement system (Micro-Epsilon OptoNCDT 1700).

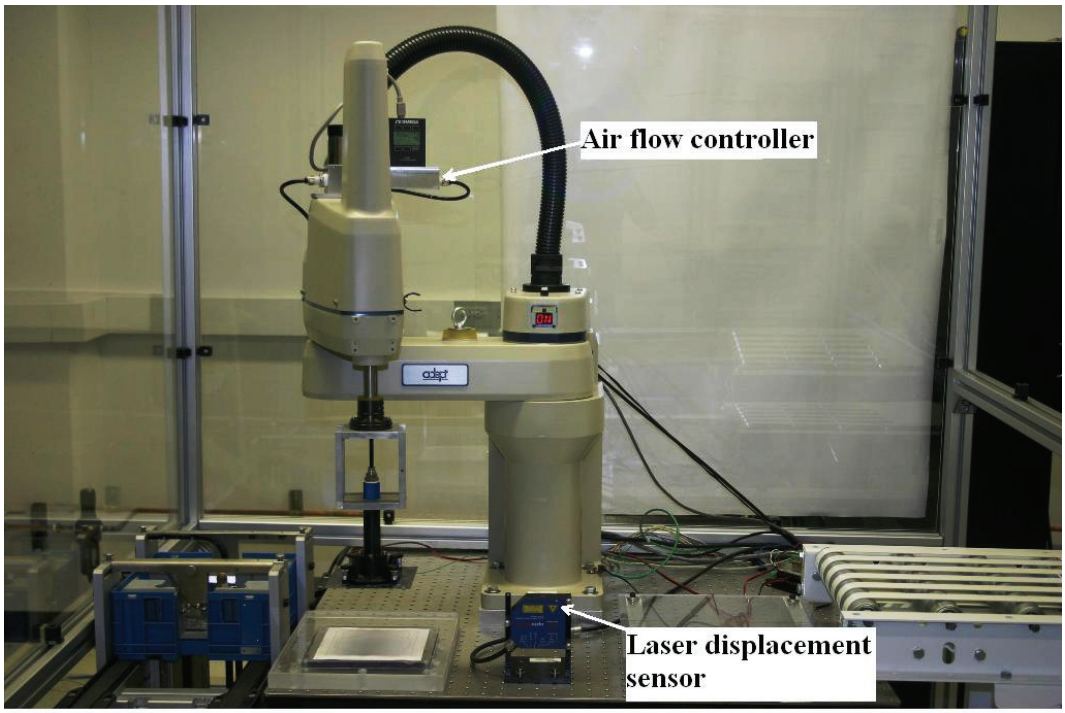

Figure 5.2: Experimental set-up

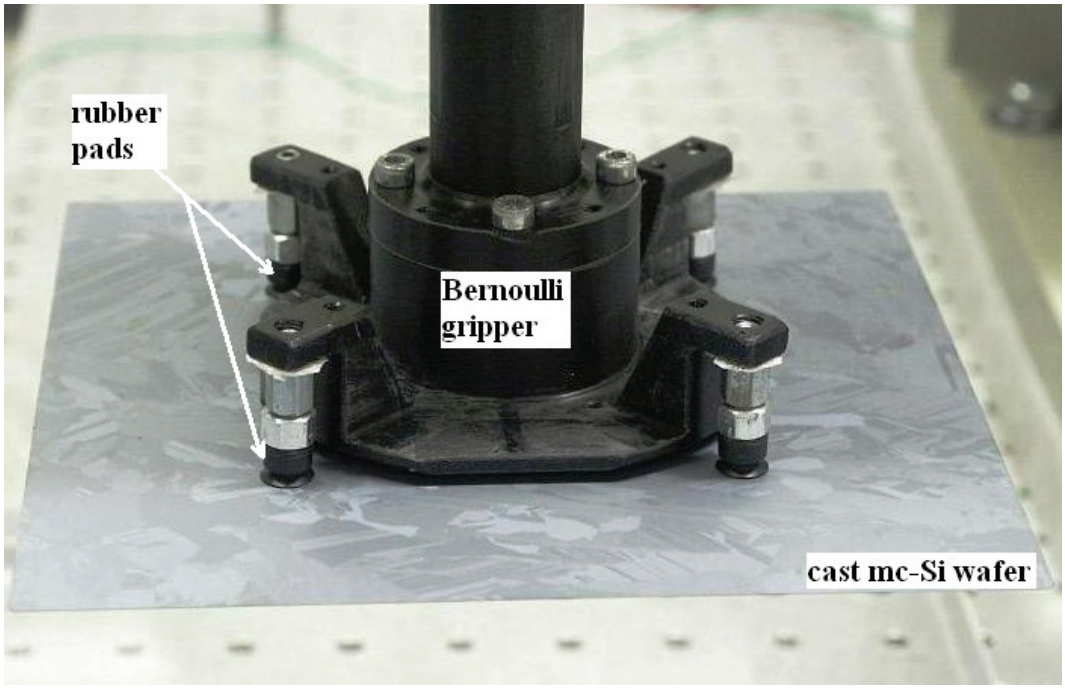

Figure 5.3: Bernoulli gripper handling a 156 mm cast wafer

The full-field wafer deformation measurement procedure using the laser-based sensor is as follows. The robot scans the gripped wafer (at a fixed air flow rate and stand-off distance) along a path defined by a specified grid while the laser sensor measures the wafer deformation. Once scanning is complete, the height between the laser and each of the four rubber pads on the Bernoulli gripper is measured and a least-squares reference plane is calculated using the pad heights. Thereafter, the full-field wafer deformation with respect to the least-squares plane is obtained from the laser data.

Table 5.1: Wafer characteristics and scan grid spacing specification

Wafer Type	Size	Average Thickness (μm)	# Samples	Grid Spacing (mm)
Cz wafer <100>	125 mm x 125 mm	219.2 ± 1.2	5	1.5
Cast wafer	125 mm x 125 mm	256.5 ± 0.5	5	1.5
Cast wafer	156 mm x 156 mm	146.0 ± 8.0	5	1.5
EFG wafer	100 mm x 100 mm	179.6 ± 1.9	5	1.5

The foregoing scanning procedure was applied to several Si wafers of different types and thicknesses listed in Table 5.1. The average wafer thickness was estimated through wafer weight measurements. The wafers used were as provided by the suppliers and included some etching to remove surface damage from wire sawing/laser cutting operations. In each experiment with a given wafer type, the volumetric air flow rate was varied from 30 to 40 liters/min. The stand-off distance between the gripper and wafer, H, was fixed at 2 mm. The measured response was the full-field wafer deformation from which the maximum wafer deformation could be extracted.

The influence of volumetric air flow rate, V, on wafer deformation at the center of the wafer (maximum deformation) is shown in Figure 5.4. It is clear that the deformation increases with air flow rate and, for air flow rates greater than 37 l/min, is greatest in the thin 156 mm cast wafer and smallest in the thick 125 mm cast mc-Si wafer. It can be also seen that an upper limit of wafer deformation exists for the thin EFG wafers as the flow rate is increased. This is largely a result of the wafer deformation approaching the maximum displacement permitted by the gripper geometry and is a function of the stand-off distance defined by the rubber pads. Another factor that contributes to the leveling of wafer deformation, especially at high air flow rates at which the top surface of the deformed wafer approaches the gripper surface, is the positive air pressure acting on the wafer around the cone mill (see Figure 4.1) as the air enters the gap between the gripper and wafer and directly impinges on the wafer surface. This positive pressure moderates the effect of negative air pressure (or vacuum) created by the radially diverging air flow.

The influence of volumetric air flow rate and wafer type on the full-field wafer deformation is shown in Figure 5.5. The deformation contours in this figure yield conclusions similar to those derived from Figure 5.4. In addition, one can see that for all wafer types there is a preferred orientation of the deformation as the volumetric air flow rate is increased. Material anisotropy cannot explain this preferred orientation since it appears to be the more or less the same for all wafer types. Careful analysis of the gripper geometry shows that the preferred orientation is due to small errors in the actual location of the rubber pads. If the rubber pads were symmetrically located around the center of the gripper, a symmetric deformation profile would be obtained. The errors in the location of the pads lead to differences in moment arms and consequently a reversed U-shape deformation pattern is obtained at high flow rates.

An analytical surface is fit to the wafer deformation data using polynomial regression in order to represent the deformed wafer by a smooth, continuous and well-defined surface. The following fourth-order polynomial regression model with two predictor variables is used for this purpose:

$$E\{\delta_i\} = \beta_0 + \beta_1 x + \beta_2 y + \beta_{12} xy + \ldots + \beta_{1111} x^4 + \beta_{2222} y^4 \qquad (5.2)$$

where x and y are the coordinates in the reference plane of the wafer (cf. Figure 5.5) and δ_i is the out-of-plane deformation. For all wafer types, the R-squared value of the surface fit obtained was close to 1 indicating a good fit (cf. Figure 5.6).

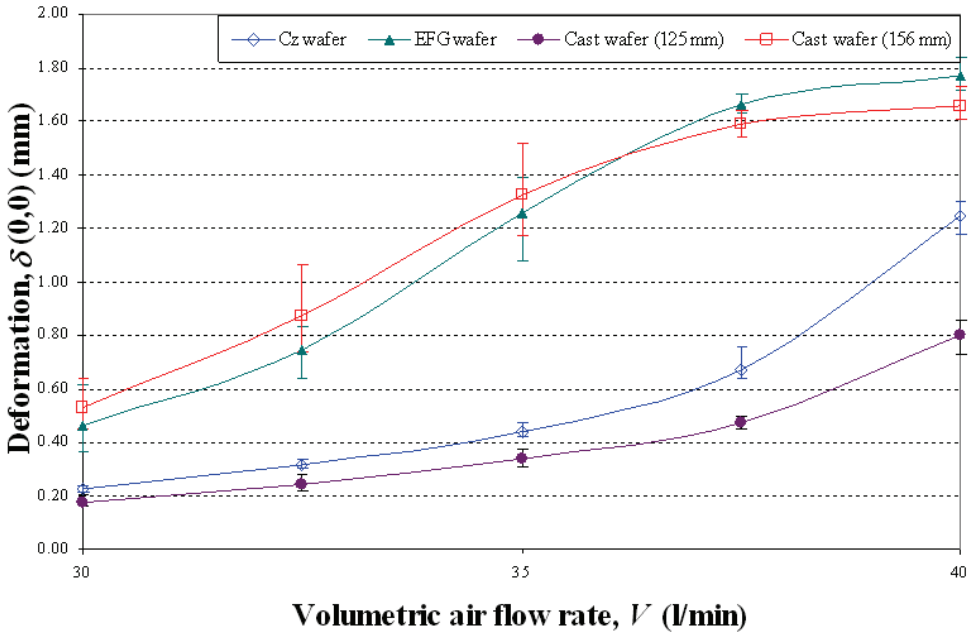

Figure 5.4: Influence of volumetric air flow rate on the out-of-plane deformation at the center of the wafer

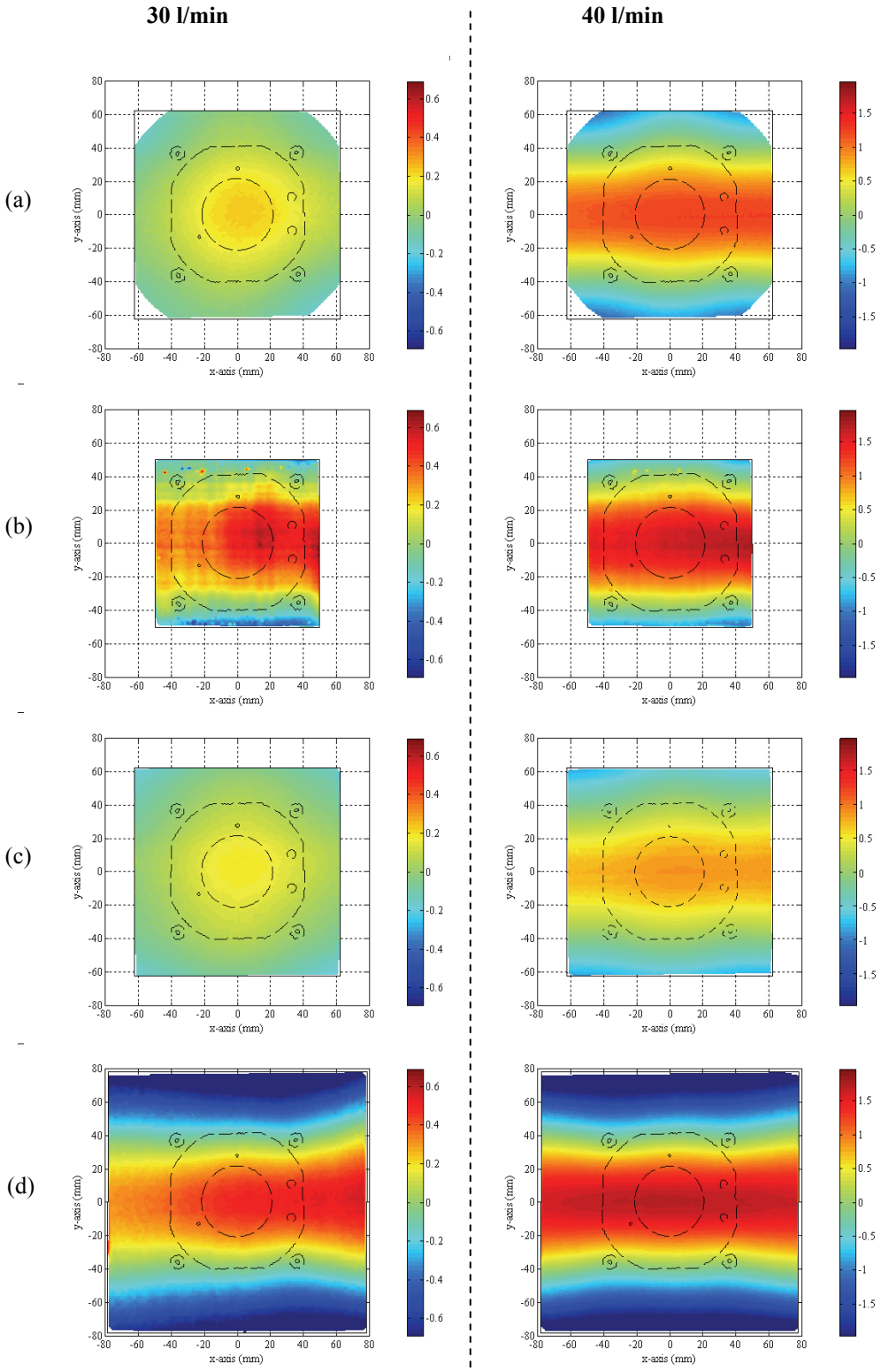

Figure 5.5: Wafer out-of-plane deformation (in mm) pattern as a function of volumetric air flow rate: (a) Cz wafer, (b) EFG wafer, (c) 125 mm cast wafer and (d) 156 mm cast wafer

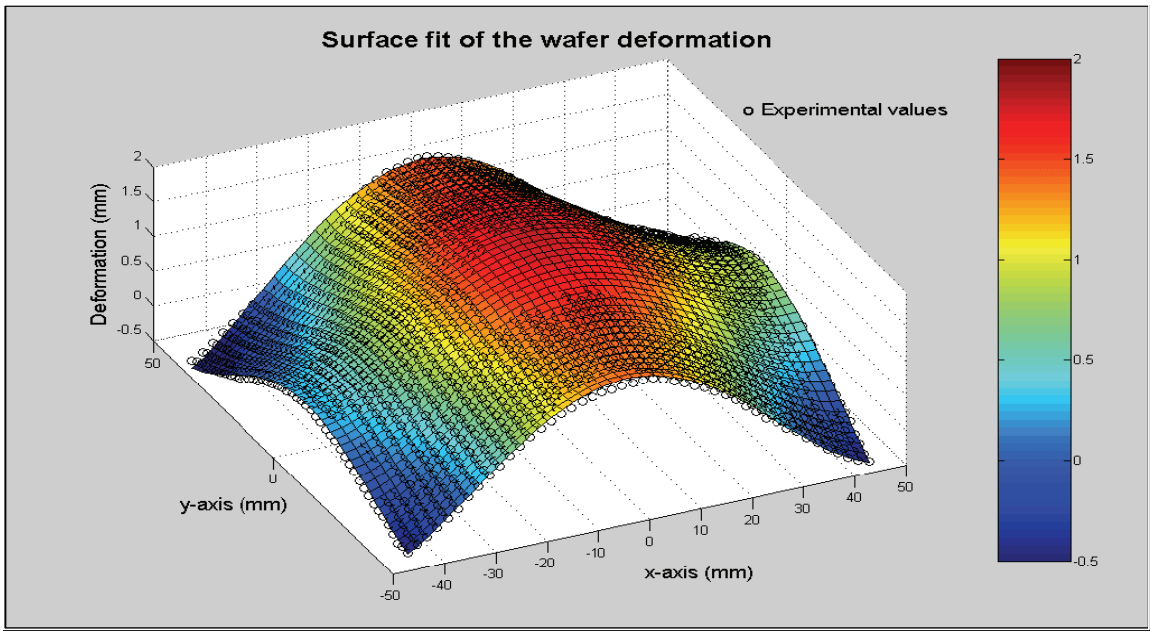

Figure 5.6: Typical surface fit of the wafer deformation and corresponding experimental values (EFG silicon wafer, *H*=2mm, *V*=40 l/min)

5.2.2 Determination of the Total Stress State

The total stress state produced in the Si wafer due to handling forces exerted by the Bernoulli gripper plus any residual stresses present in the wafer from prior processing is determined from the full-field wafer deformation data via finite element analysis. Specifically, the measured wafer deformation is imposed as a displacement boundary condition on the finite element model of the Si wafer and the model is solved to obtain the corresponding stress distribution. The finite element model for each wafer type is built and solved using standard finite element software (in this case ABAQUS®) as described next.

5.2.2.1 Model Geometry

The different Si wafer types considered in the previous experiments are modeled as thin plates of uniform thickness using 4-node general purpose thin shell elements for finite strains (type S4) in order to capture the large deformation exhibited by the wafers. The model and analysis account for the geometric non-linearity associated with large wafer deformation associated with thin wafers, which causes some of the load to be carried by membrane action rather than by bending alone. Preliminary analysis showed that the differences in the results obtained from linear and nonlinear simulations are sufficiently large to indicate that a linear simulation is not adequate for these wafers. Similar conclusions were derived in [53] when modeling the fracture twist test of Cz wafers using the finite element method. Because of the asymmetry in the wafer deformation (as seen in Figure 5.5), a full 3-D wafer model is employed.

5.2.2.2 Material Properties

The Cast mc-Si wafer is assumed to be elastic and isotropic. Values of the Young's modulus and Poisson ratio for Cast silicon reported in the literature (E=162.5 GPa; υ=0.223) are used [50]. For the other wafer types, anisotropic material properties are specified using the stiffness matrix defined in the proper coordinate system (*x, y, z*) [63]. The stiffness coefficients are obtained from known compliance coefficients for single cubic Si crystal with respect to the crystal coordinate system (*x', y', z'*).

Although EFG wafers are multi-crystalline in nature, there are known to have a predominant grain orientation due to the growth process. Specifically, the EFG wafers are characterized by a {110} surface and a <112> growth direction [65]. Therefore, the stiffness is specified using the {110} single crystal properties with the $[1\bar{1}2]$, $[\bar{1}11]$ and

[110] orientations representing the *x*, *y* and *z* axes. The resulting elastic stiffness matrix (in GPa) for the EFG wafer is given by:

$$C_{ijkl}^{EFG} = \begin{pmatrix} 203.85 & 44.83 & 44.83 & 0 & 0 & 0 \\ & 194.30 & 54.38 & -13.51 & 0 & 0 \\ & & 194.30 & 13.51 & 0 & 0 \\ & & & 60.40 & 0 & 0 \\ & & & & 60.40 & 13.51 \\ sym & & & & & 69.96 \end{pmatrix} \tag{5.3}$$

A similar approach is used for the Cz wafers. Specifically, properties of the {100} crystallographic orientation of the single crystal are used, taking [001], [010] and [100] orientations as the *x*, *y* and *z* axes. Due to its cubic symmetry, the stiffness matrix is invariant to transformation and the resulting elastic stiffness matrix (units of GPa) is given by:

$$C_{ijkl}^{Cz} = \begin{pmatrix} 165.64 & 63.94 & 63.94 & 0 & 0 & 0 \\ & 165.64 & 63.94 & 0 & 0 & 0 \\ & & 165.64 & 0 & 0 & 0 \\ & & & 79.51 & 0 & 0 \\ & & & & 79.51 & 0 \\ sym & & & & & 79.51 \end{pmatrix} \tag{5.4}$$

5.2.2.3 Boundary conditions

The boundary conditions for the model are given in Table 5.2. A Fortran® subroutine (DISP) was used to define the magnitudes of the out-of-plane displacements (U_z) at all nodes. For a given wafer type, the displacements are obtained from the corresponding analytical surface fit to the measured wafer deformation (see Equation 5.2). In-plane wafer displacements are not restrained except for the center node of the wafer that is pinned (U_x=U_y=*0*) to avoid rigid body motion of the wafer.

Table 5.2: Boundary conditions specification

Boundary conditions	Location (x,y)	Value
Wafer surface	(x_s, y_s)	• $U_z = \delta_i(x, y)$
Center	(0,0)	• $U_x = U_y = 0$

5.2.2.4 Mesh grid independence

The mesh employed for each wafer type is shown in Figure 5.7. Four node quadrilateral shell elements were used to define the two-dimensional structured grid. Due to the simple geometry, skewness of the cells was checked and was found to be adequate. An important factor governing the quality of finite element simulations is the computational grid quality. Analysis of grid independence was therefore performed. The sensitivity of the results to the grid resolution was tested for the computed stresses for eight different grids per wafer type. The number of shell elements was refined iteratively to obtain reliable results by reducing the seed size. Table 5.3 shows the number of quadrilateral shell elements, *N*, with respect to seed size. The different computational grids were compared to the finest mesh solution. The predicted stress in the *y* direction (as shown in Figure 5.5) generated by the gripper at the center node of the handled wafer on its top surface is plotted in Figure 5.8 as a function of the number of shell elements used. The relative error in the predicted stress values compared to the finest mesh solution is also plotted. It is important to note that the relative change in the predicted stress between the three finest grid models is small (less than 0.2 %). Since the simulation times for these models are reasonable (less than 1 hour on a single Pentium 2.8 GHz

processor machine) the mesh corresponding to the 2 mm seed size was considered to be adequate for all simulations.

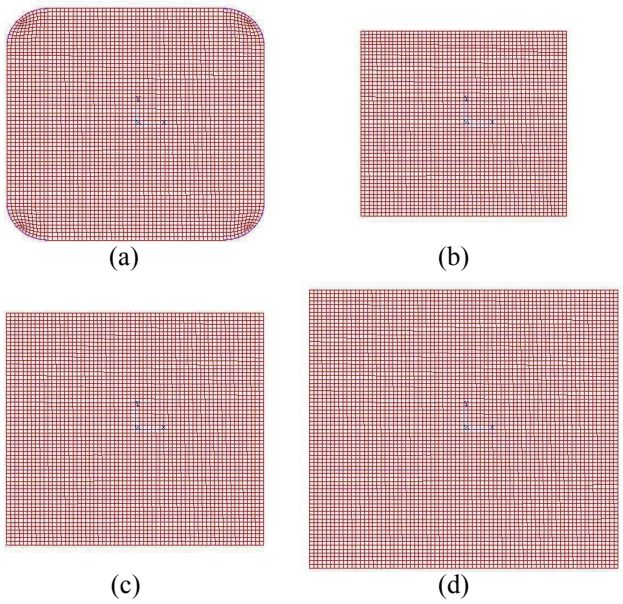

Figure 5.7: Mesh for the different wafer types with 2mm seed size: (a) Cz wafer, (b) EFG wafer, (c) Cast wafer 125mm and (d) Cast wafer 156mm

Table 5.3: Different grids used for the grid independence check and their corresponding number of elements

Seed size	(mm)	1	1.5	2	2.5	3	4	5	6
N (Cz)	(#)	15400	6770	3828	2484	1748	988	572	396
N (EFG)	(#)	10000	4422	2500	1600	1122	576	400	256
N (Cast 125 mm)	(#)	15500	6972	3844	2500	1764	992	576	400
N (Cast 156 mm)	(#)	22500	10000	5476	3600	2500	1444	900	576

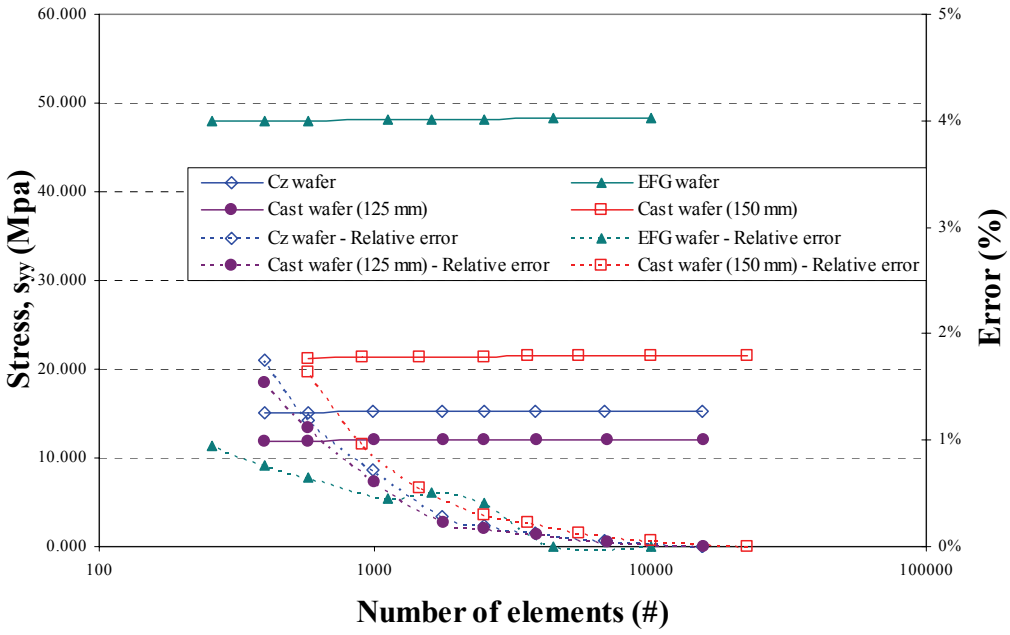

Figure 5.8: Total stress value, s_{yy}, at the center on the top surface of the wafer as a function of the number of shell elements used in the different models (V=40 l/min for Cz wafer and Cast wafers; V=37.5 l/min for the EFG wafer)

5.2.3 Analysis of the Total Stress State

The maximum in-plane principal tensile stresses acting on the top surface of the wafer, σ_{max}, obtained from the finite element simulations are summarized in Table 5.4. The location in the table refers to the location of the maximum principal tensile stress in the wafer. As expected, irrespective of wafer type, an increase in the volumetric air flow rate leads to an increase in the tensile stress. At the highest air flow rate, the principal tensile stress levels are quite high for all wafer types, with the thin EFG wafer exhibiting the highest value.

In the absence of knowledge of the location and orientation of cracks in the wafer, σ_{max} provides a metric based on which a conservative estimate of the limiting crack size

for fracture during handling can be determined from linear elastic fracture mechanics theory. In other words, breakage will not occur if the actual crack sizes are smaller than the critical crack size irrespective of their orientation and location.

Table 5.4: Max in-plane principal tensile stress

	V (l/min)	σ_{max} (Mpa)	Location
Cz wafers (219 μm)	30	5.4	Center
	35	10.9	Cener
	40	41.9	Edge
EFG wafers (180 μm)	30	16.1	Center
	35	40.2	Center
	40	62.9	Edge
Cast wafers 125 mm x 125 mm (256 μm)	30	4.5	Center
	35	9.1	Center
	40	29.4	Edge
Cast wafers 156 mm x 156 mm (146 μm)	30	14.5	Edge
	35	39.2	Edge
	40	54.5	Edge

Figures 5.9 and 5.10 show the maximum in-plane principal stress distribution on wafer surface as a function of volumetric air flow rate for the EFG and cast (125 mm), respectively. The tensile stress distribution is seen to change significantly with an increase in the air flow rate. Specifically, the location of σ_{max} shifts from the center of the wafer to the edge. As demonstrated in the previous chapter this change in location is due to the preferred orientation of the wafer deformation resulting from imperfections in the gripper geometry and more specifically to the differences in the location of the rubber pads.

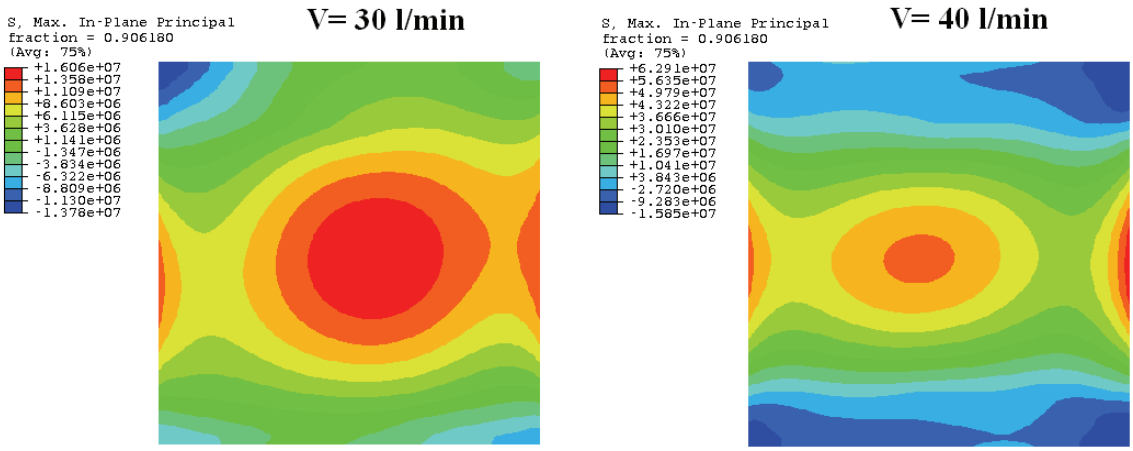

Figure 5.9: Typical maximum in-plane principal stress distribution (Pa) for EFG wafer at 30 l/min and 40 l/min air volumetric flow rates

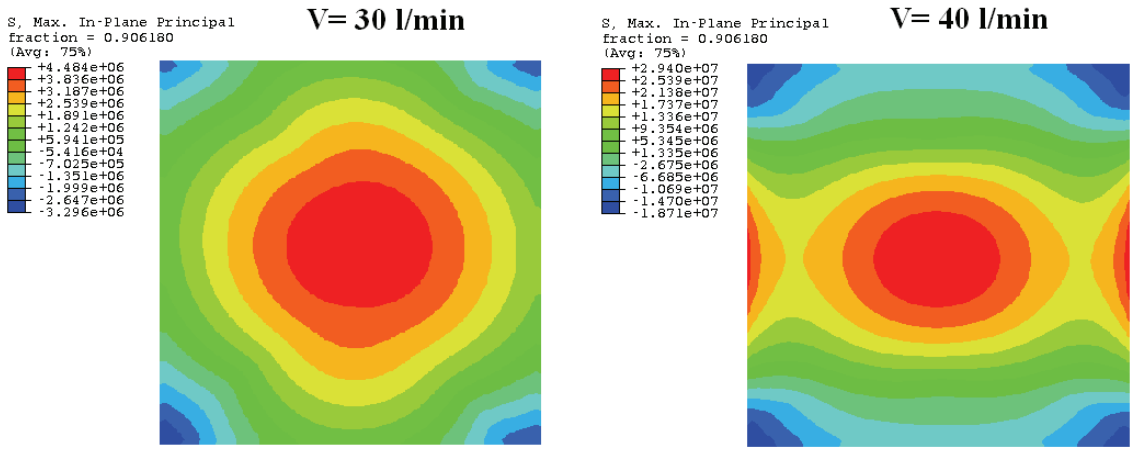

Figure 5.10: Typical maximum in-plane principal stress distribution (Pa) for cast (125 mm) wafer at 30 l/min and 40 l/min air volumetric flow rates

5.3 Wafer Breakage Analysis

Having determined the total stress state in the wafer during handling, it is of interest to determine if the wafer will break under the handling forces acting on the wafer. Alternatively, I would be useful to know the limiting crack size in the wafer that will lead to wafer breakage under the applied handling forces. Answers to these questions can be obtained from the application of linear elastic fracture mechanics theory as follows. Assuming that mode I fracture is the predominant mode and if a crack is located in an area of tensile stress, its propagation depends on the following factors:

- magnitude of the far field tensile stress acting perpendicular to the crack plane,
- crack geometry (size and shape), and
- fracture toughness K_C of the material.

From linear elastic fracture mechanics theory, the stress intensity factor for an edge crack of length, l, under a far field tensile stress, σ_∞ , is given by [77]:

$$K_I = Y\sigma_\infty\sqrt{\pi l} \tag{5.5}$$

where Y is the shape factor for an edge crack in a specimen with finite width, w, and is computed as:

$$Y = 1.122 - 0.231\left(\frac{l}{w}\right) + 10.550\left(\frac{l}{w}\right)^2 - 21.710\left(\frac{l}{w}\right)^3 + 30.382\left(\frac{l}{w}\right)^4 \tag{5.6}$$

A crack will propagate when the stress intensity factor K_I equals the fracture toughness K_C (also known as the Griffith criterion). The critical tensile (or fracture) stress is then given by:

$$\sigma_f = \frac{K_C}{Y}(\pi l)^{-1/2} \tag{5.7}$$

For single crystal silicon (sc-Si) and EFG wafers, inherent material anisotropy will lead to different values of K_C depending on the crystal orientation. For Cast mc-Si wafers, anisotropy at the wafer level is absent and K_C may be assumed to be independent of crystallographic orientation. Table 5.5 shows the fracture toughness values of Si wafers with different orientations (for sc-Si) reported in the literature. Note the large variation in the K_C values for the {111} cleavage plane, mainly due to differences in the test methods employed. Chen and Leipold [78] used four-point bending to evaluate the effect of crystal orientation on the fracture toughness of silicon. More recently, Ebrahimi and Kalwani [79] have used indentation to analyze the anisotropic behavior of the fracture toughness in single crystal silicon.

Table 5.5: Fracture toughness of silicon [79, 80]

Material	Cleavage Plane	K_C (MPa √m)	Ref.
sc-Si	{100}	0.95	[78]
sc-Si	{110}	0.90	[78]
sc-Si	{111}	0.82	[78]
		1.31±0.09	[79]
mc-Si	N/A	0.75±0.06	[78]

5.3.1 Determination of Wafer Breakage Stress During Handling

The approach used for determining the wafer breakage stress during Bernoulli gripping is summarized in Figure 5.11. The first step in the approach consists of experimentally characterizing the influence of volumetric air flow rate (V) on wafer deformation, δ. Equation (5.8) describes this influence for every wafer i and is established through full-field wafer deformation measurements described earlier.

$$\delta^i(x,y) = f_i(V) \tag{5.8}$$

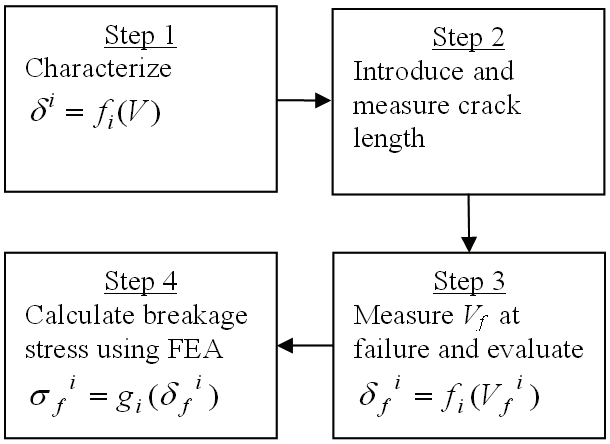

Figure 5.11: Flowchart of the approach

As discussed earlier and specified in Equation (5.2), for a given air flow rate, the function f_i can be represented by a fourth order polynomial regression model.

The second step consists of artificially introducing a crack in the Si wafers using micro indentation. As mentioned earlier, the EFG wafers are known to have a predominant {110} grain orientation and <112> growth direction due to the crystal growth process [66]. A Knoop indenter (elongated diamond pyramid) is used to generate a small notch on the wafer edge perpendicular to the growth direction and initiate a relatively straight through-thickness crack in the growth direction. Figure 5.12 illustrates schematically the location and orientation of the notch/crack produced in the wafer. The crack length, *l*, is not controlled and is measured using an optical microscope. A typical crack generated in this manner is shown in Figure 5.13. The notch size being much smaller than the crack length, its influence on wafer fracture is neglected. The specific

crack orientation is chosen to create {111} cleavage planes thus avoiding transgranular fracture of the wafer.

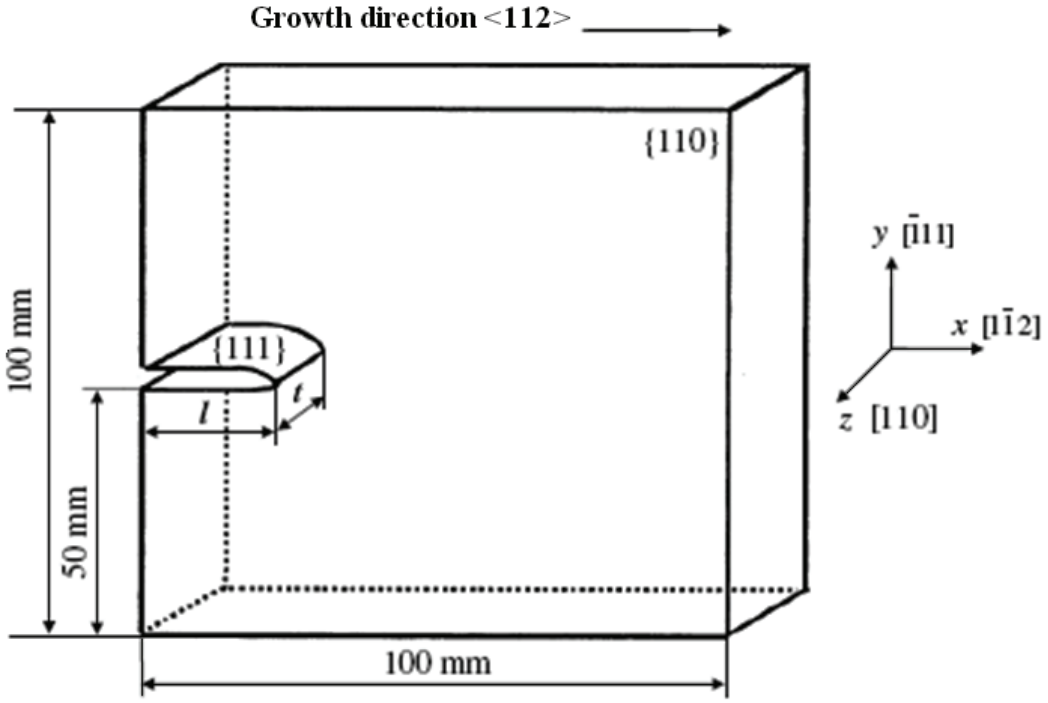

Figure 5.12: Schematic of the through-thickness crack in EFG wafer

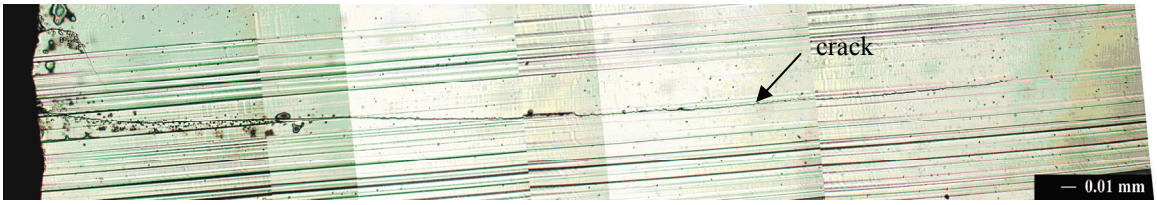

Figure 5.13: Optical microscope picture of 0.60 mm crack (sample #4)

Breakage experiments are then carried out using the Bernoulli gripper where it is important to keep the same wafer orientation as in the first step due to the asymmetry in wafer deformation (see Figure 5.5). The air flow rate is increased slowly at a rate of 0.2

L/min till wafer breakage occurs. From Equation (5.8) and the air flow rate at failure, V_f, the wafer deformation at fracture is obtained as follows:

$$\delta_f{}^i(x,y) = f_i(x,y,V_f) \tag{5.9}$$

Since the crack sizes are relatively small compared to the wafer width, it is assumed here that the presence of the crack does not affect significantly the wafer deformation profile obtained from the un-cracked wafer. Therefore, Equation 5.9 can be used to estimate the wafer deformation at fracture.

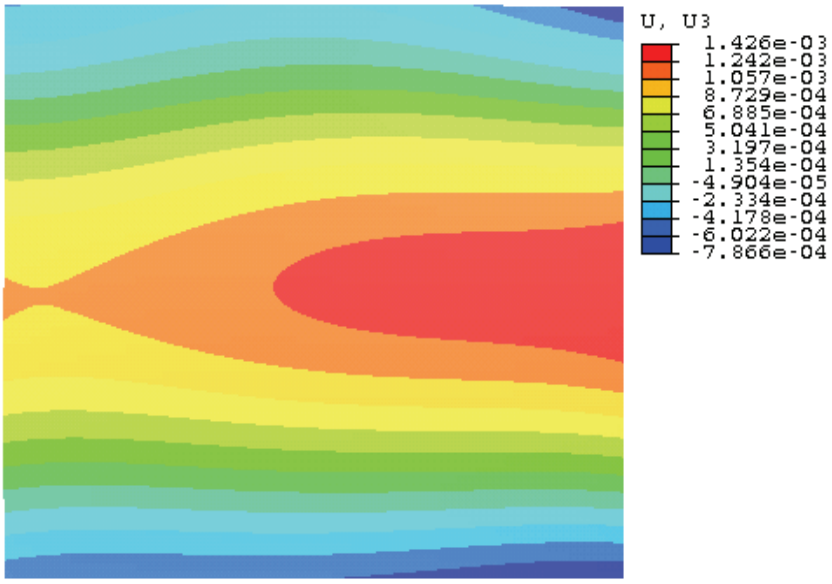

Figure 5.14: Wafer deformation profile at failure calculated using Equation 5.3 (sample #4)

Figure 5.14 shows an example of the wafer deformation at fracture. As mentioned before, it can be seen that the deformation is not perfectly symmetric due to imperfections in the gripper geometry. In addition, microscopic observation of the crack plane after fracture reveals that the EFG wafer is inherently thicker at the edges normal to the growth direction and thinner at the center.

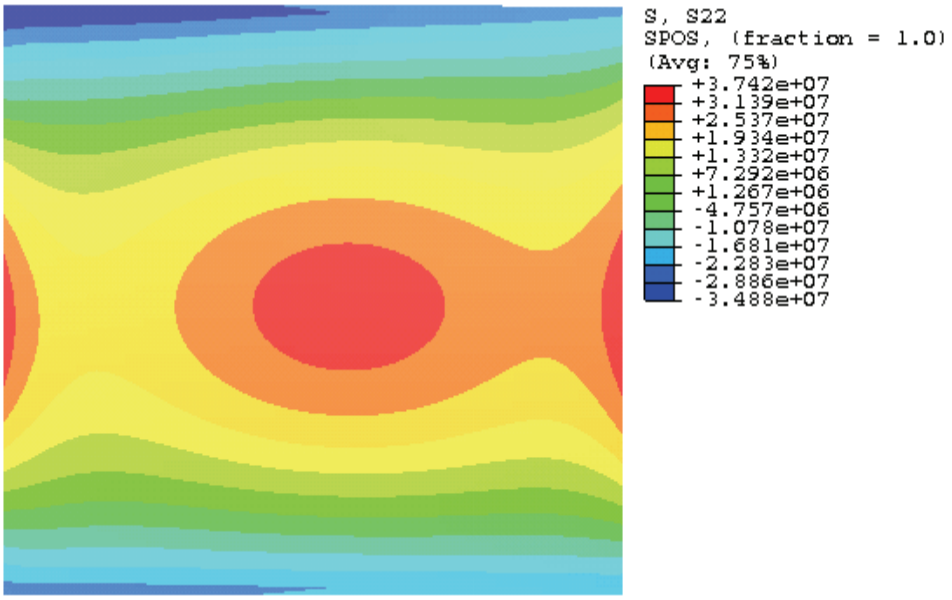

Figure 5.15: Total stress distribution, s_{yy}, on the wafer surface (sample #4)

Finally, the total stress state at breakage is obtained from non-linear finite element analysis (FEA) with the wafer deformation at fracture (Equation 5.9) imposed as the displacement boundary condition on the model. Figure 5.15 shows a typical stress distribution obtained from FEA on the top surface of the wafer perpendicular to the crack plane. Note that the average tensile stress along the crack direction over the whole wafer width is extracted from the finite element simulation and used as an estimate of the far-field stress acting on the crack plane at breakage. The resulting wafer breakage stress is denoted as follows:

$$\sigma_f{}^i = g_i(\delta_f{}^i) \tag{5.10}$$

5.3.2 Validation of Wafer Breakage Stress Approach

Wafer breakage experiments were carried out to validate the forgoing wafer breakage stress determination approach. As-received 100 mm x 100 mm EFG wafers were selected from the same batch for the experiments. The wafers were etched by the supplier in two groups to remove surface damage from laser cutting operations. The average thickness ($t_{\{111\}}$) of these groups was determined from weight measurements and found to be 180 μm and 160 μm, respectively. The test setup shown earlier in Figure 5.2 was used. As before, the wafer stand-off distance between the Bernoulli gripper and the EFG wafer was fixed at 2 mm. Before introducing a crack in each wafer, the full-field wafer deformation was obtained (Step 1 in Figure 5.11) by varying the volumetric air flow rate from 27.5 to 40 liters/min.

Table 5.6 summarizes the results for the EFG wafers that survived the indentation process. This process yielded 14 unbroken wafers of which 3 wafers had crack sizes above 16 mm or were not properly oriented and were consequently not used in the breakage tests. As mentioned earlier, the thickness variation on the cleavage plane was measured after wafer fracture and found to exhibit an average total thickness variation (TTV) of ±13% in the wafer growth direction. The wafer thickness on the cleavage plane, $t_{\{111\}}$, the crack size l, the volumetric air flow rate, V_f, and the failure stress, σ_f, are listed in Table 5.6 for the 11 wafers. The observed thickness variation is related to the control of the pulling rate during the EFG wafer growth process. The effect of this variation was accounted for in the finite element simulations by running three simulations for each wafer at the measured average, maximum, and minimum thickness of the cleavage plane (listed in Table 5.6).

Table 5.6: Calculated failure stress for EFG wafers

Wafer (#)	$t_{\{111\}}$ (μm)	l (mm)	V_f (l/min)	σ_f (MPa)
1	163 ± 21	0.33	39.1	44.3
2	115 ± 21	0.40	34.0	33.6
3	135 ± 13	0.45	33.0	30.9
4	169 ± 16	0.60	35.5	32.6
5	134 ± 19	1.15	31.4	18.1
6	159 ± 26	1.70	34.3	24.5
7	164 ± 30	2.62	30.1	6.5
8	151 ± 20	2.95	31.6	16.0
9	168 ± 12	3.13	32.1	10.1
10	161 ± 19	4.11	31.8	6.5
11	163 ± 23	6.19	30.6	11.9

The wafer breakage stress determined from Equation (5.10) is plotted as a function of the crack length in Figure 5.16 (labeled as "Experiment"). The figure also contains a plot of the theoretical fracture stress determined from Eqs. (5.6)-(5.7) for two values of fracture toughness for sc-Si wafers along the {111} cleavage plane reported in the literature [78, 79]. The experimental breakage stress values are seen to be in fairly good agreement with the theoretical values. Although some scatter is evident in the experimental failure stress values, most of them fall within the range of the theoretical values. When the experimental breakage stress is plotted as a function of the inverse square root of the crack length as shown in Figure 5.17, a strong proportional relationship is found as indicated by linear elastic fracture mechanics theory (see Equation 5.7 which assumes a nearly constant shape factor). This further validates the breakage stress calculation using the FEA method outlined in Figure 5.11.

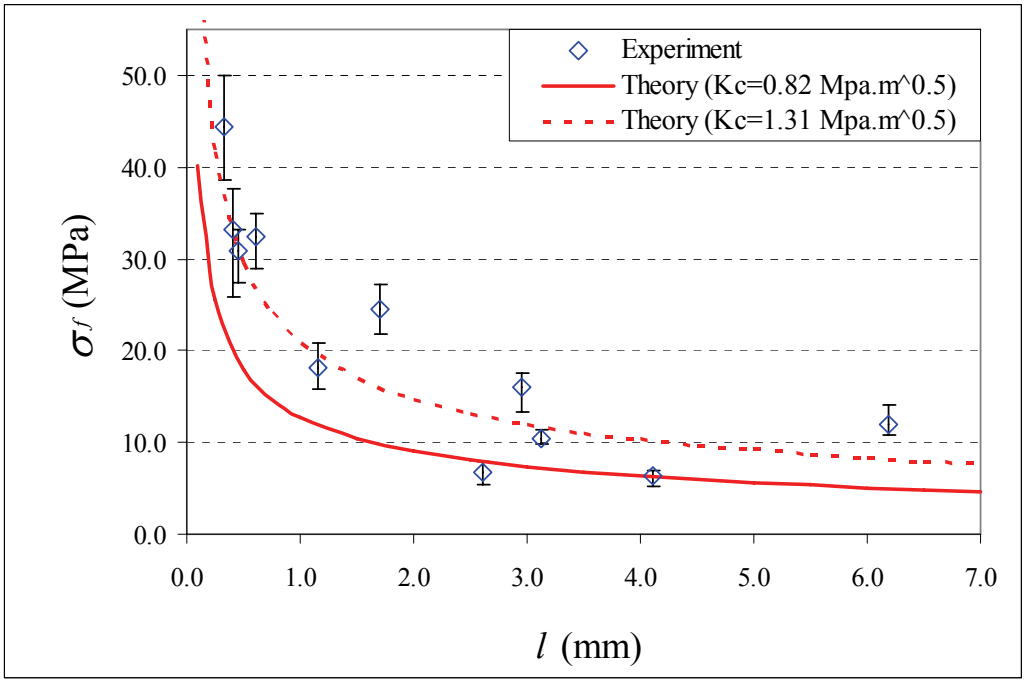

Figure 5.16: Experimental and theoretical failure stresses as a function of the crack length

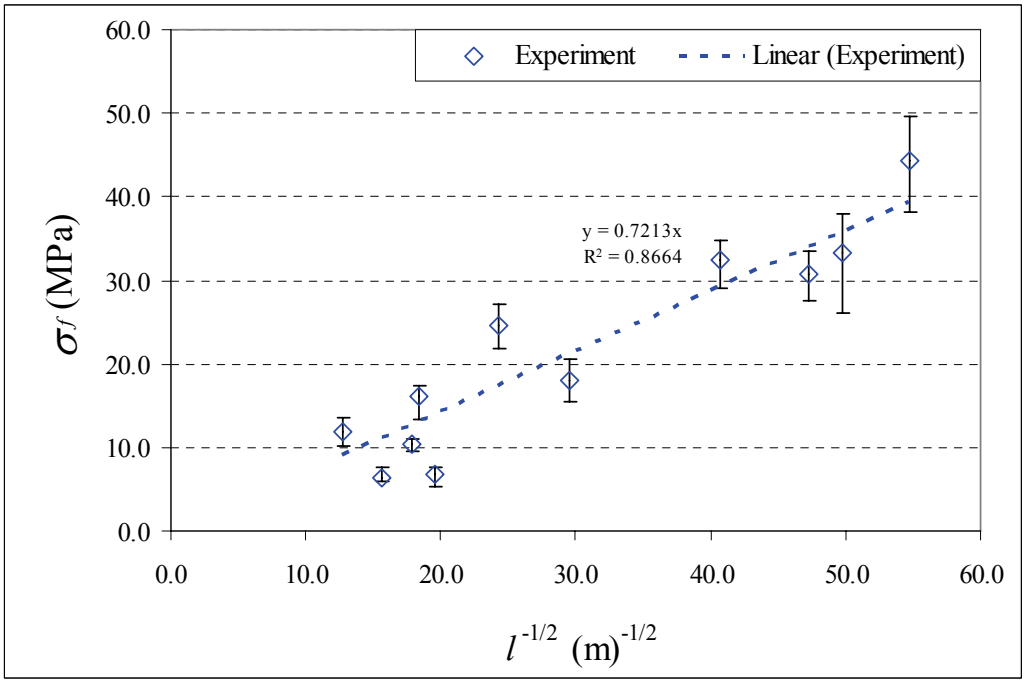

Figure 5.17: Experimentally determined failure stress as a function of the (crack length)$^{(-1/2)}$

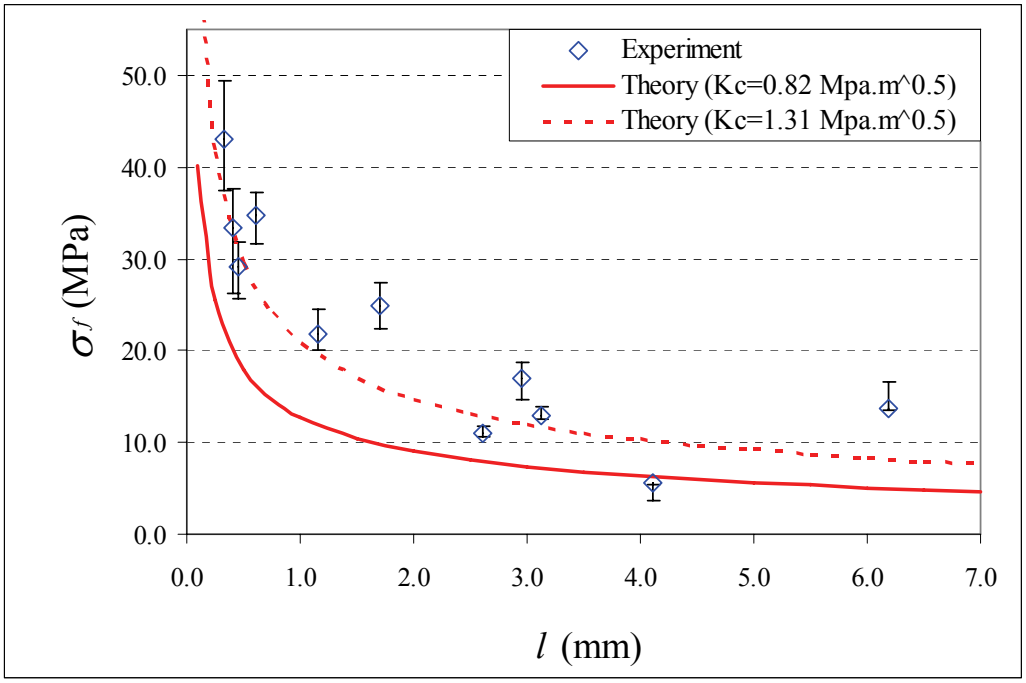

Figure 5.18: Experimental and theoretical failure stresses as a function of the crack length (half wafer width analysis)

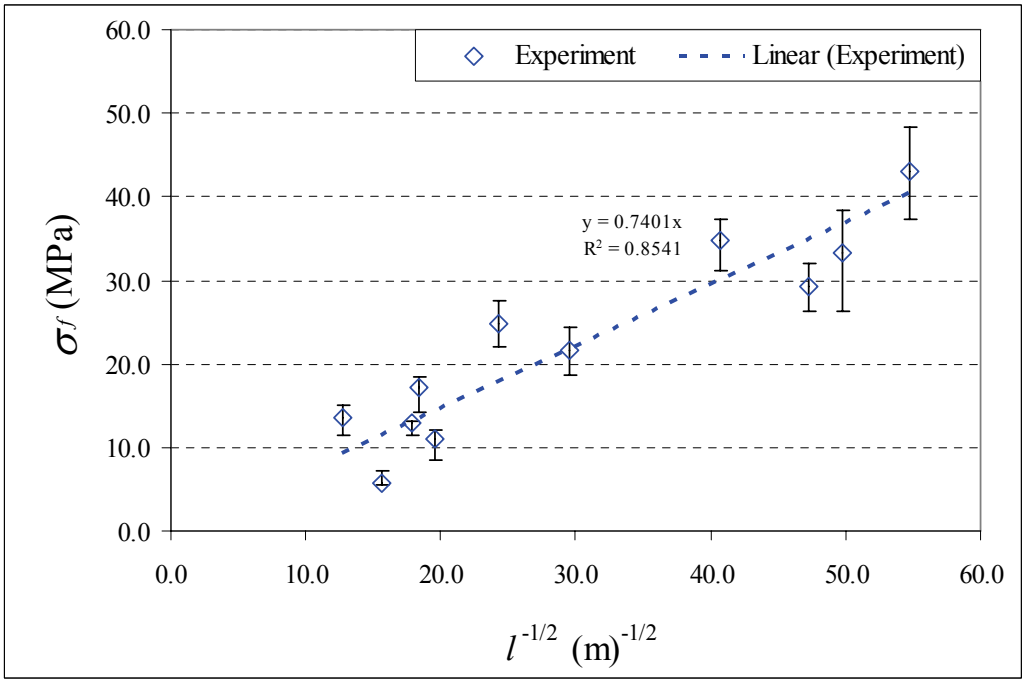

Figure 5.19: Experimentally determined failure stress as a function of the (crack length)$^{(-1/2)}$ (half wafer width analysis)

In Figures 5.16 and 5.17, the far-field stress was evaluated as the average tensile stress along the crack direction over the full wafer width (cf. Equation 5.10). A more localized approach has also been tried where only half the wafer width was used to determine the far-field stress. Figures 5.18 and 5.19 show the results obtained, which are found to be similar to those obtained previously.

Since the widths of the different wafer types tested are much larger than the corresponding crack sizes, the shape factor, Y, is nearly constant. Consequently, the fracture toughness values can be obtained from the slopes in Figures 5.17 and 5.19. The calculated values thus obtained are 1.43 and 1.47 MPa $\sqrt{m}$, respectively. These values are large compared to the values for silicon reported in the literature (see Table 5.5). This can be explained by the influence of the sample thickness on the fracture toughness. It is well known that for thick samples the fracture toughness is thickness independent (plain strain situation). However, with decrease in sample thickness the fracture toughness tends to increase [80]. In addition, since the failure stress is predicted here from deformation profiles obtained from un-cracked wafers, this approach may be overestimating the failure stress.

5.3.3 Practical Use of the Wafer Breakage Analysis

5.3.3.1 When Measured Deformation Profiles are Available

Note that the wafer breakage analysis approach presented in this chapter assumes prior knowledge of crack size, location and orientation in the wafer. If this information is available, for instance using one of the crack detection methods discussed in the literature [58-60, 74], then the approach can be used to determine if the selected handling device control variables (e.g. volumetric air flow rate and stand-off distance in the case of the Bernoulli gripper) will cause wafer breakage. The total stress state in the wafer can be

obtained from the full-field wafer deformation just before breakage and, using the approach outlined in step 4 of the breakage stress determination procedure (Figure 5.10), the breakage stress during handling can be compared to the theoretical fracture stress (Equation 5.7). This will allow determination of how close to wafer breakage the current handling conditions are. If the actual stress is close to the failure stress, handling control variables such as the air flow rate could be reduced to avoid breakage.

Alternatively, the maximum in-plane principal tensile stress in the wafer extracted from the finite element simulation for a given volumetric air flow rate and stand-off distance can be used as an estimate of the wafer breakage stress and by combining it with Equation (5.7) a limiting crack length for breakage during handling under the chosen conditions can be established. This crack length value will be admittedly conservative but can still be useful for screening out defective wafers. Table 5.7 lists the critical crack lengths calculated using this approach for the samples listed in Table 5.1.

Table 5.7. Calculated critical crack sizes from measured deformation profiles

	K_C	V	σ_{max}	l_c
	Mpa.m$^{0.5}$	(L/min)	(Mpa)	(mm)
Cz wafers	0.82	30	5.4	7.14
		35	10.9	1.75
		40	41.9	0.12
EFG wafers	0.82	30	16.1	0.80
		35	40.2	0.13
		40	62.9	0.05
Cast wafers 125 mm x 125 mm	0.75	30	4.5	9.40
		35	9.1	2.30
		40	29.4	0.22
Cast wafers 156 mm x 156 mm	0.75	30	14.5	0.90
		35	39.2	0.12
		40	54.5	0.06

5.3.2.2 When Measured Deformation Profiles are Unavailable

When wafer deformation measurements are not available, the modeling approach presented in Chapter 4 can be really useful for determining the critical crack lengths. If the full residual stress state in the wafer is known, the total stress state can be calculated by superposing the residual stress on the handling stresses predicted by the iterative approach presented in Chapter 4 (see Figure 4.2). The critical crack lengths can then be obtained in a manner similar to that used to obtain the results shown in Table 5.7.. Results obtained using this procedure are given in Table 5.8, where the residual stresses were assumed to be negligible compared to the handling stresses. The maximum in-plane principal stresses listed in the table are extracted from Figures 4.23 and 4.24 for cast and EFG silicon wafers, respectively.

Table 5.8. Calculated critical crack sizes from predicted handling stresses

	K_C	V	σ_{max}	l_c
	Mpa.m$^{0.5}$	(L/min)	(Mpa)	(mm)
EFG wafers	0.82	30	16.1	1.06
		40	62.9	0.13
Cast wafers	0.75	30	4.5	3.83
		40	29.4	0.12

In addition, if the crack location, size and orientation are known a priori, the handling stress prediction model presented in Chapter 4 can be used in conjunction with linear elastic fracture mechanics theory and knowledge of the residual stresses to determine the volumetric air flow rate and/or the stand-off distance that will prevent wafer breakage.

5.4 Summary

This chapter presented a systematic approach for the analysis of the total stress state produced in sc-Si and mc-Si wafers during handling and the relationship to wafer breakage. Although the chapter focused on a specific wafer handling method, namely Bernoulli gripping, the overall approach is general and applicable to all handling devices that induce wafer deformation and consequently stresses. It is shown that the air flow rate, wafer type and thickness have a significant effect on the magnitude and distribution of handling stresses. For all wafer types, results showed a transition in the maximum in-plane principal tensile stress location from the center to the wafer edge as the air flow rate is increased. Based on knowledge of the total stress state and crack size and location, an approach to determine the breakage stress was presented. The results showed that the proposed approach yields breakage stress values that are consistent with linear elastic fracture mechanics theory. The experimental results also show that the wafer breakage stress determined using the approach is proportional to the inverse square root of the crack length as expected from linear elastic fracture mechanics, hence validating the in-plane tensile stress calculation. This work confirms the capability of predicting wafer breakage during handling using the total stress state provided the crack size, location and fracture toughness are known. Alternately, the approach can be used to determine a conservative estimate of the critical crack length for a given handling condition. Wafers with cracks less than the critical value will not break under the given handling condition.

CHAPTER VI

CONCLUSIONS AND RECOMMENDATIONS

This chapter summarizes the main contributions and conclusions of this thesis, and suggests related areas for further exploration.

6.1 Main Contributions

The main contributions of this work can be summarized as follow:

- Development of models for analysis of thin wafer handling using a Bernoulli device.
- Fundamental understanding of the nature and magnitude of stresses generated by Bernoulli handling for different handling device variables.
- Understanding of the influence of substrate flexibility on the equilibrium lifting force, pressure distribution and stresses.
- A systematic approach to breakage analysis of crystalline silicon wafers during handling via analysis of the total stress state produced in the wafer is presented and demonstrated of being able to predict wafer breakage.

6.2 Main Conclusions

The main conclusions of this thesis are as follows:

6.2.1 Modeling of the Air Flow Generated by a Bernoulli Gripper on a Rigid Flat Object

A computational fluid dynamics model of the flow generated by a Bernoulli gripper used for low-force handling of small and large rigid and non-rigid materials has been developed. The model predicts the air flow, pressure distribution and lifting force

generated by the gripper on a rigid and flat substrate. A turbulent Reynolds stress model is used in a finite volume Reynolds-Averaged Navier-Stokes solver implemented in the general purpose CFD software FLUENT®. The following specific conclusions summarize this work:

- The model explicitly considers the non-steady characteristics of the air flow generated in the gripper and represents an enhancement over prior work in this area. The flow behavior reveals interesting features such as the flow separation region and the recirculation around the nozzle exit.
- A turbulent-to-laminar transition in the airflow was found with a Reynolds number of ~7200 close to the nozzle exit at the highest mass flow rate and laminar flow at the outer edge of the gripper. Therefore, a turbulent model is justified.
- For the gripper modeled in this work, Mach numbers at the nozzle exit were found to increase from ~0.3 to ~0.8 with an increase in the mass flow rate from 1 to 3 g/s. Consequently compressibility effects are important and were considered in the model.
- Even though the measured pressure deformation profiles were not perfectly symmetric due to imperfections in the actual gripper geometry, the axi-symmetry fluid model was able to provide adequate predictions of the pressure distribution and lifting force.
- The fluid model is shown to yield predictions of the pressure distribution on the handled object that are in good agreement with the measured envelope of the experimental pressure distribution measurements.

- The lifting force generated by the gripper was generally predicted within 12% of the measured values for most cases. The error was highest (18%) at the minimum stand-off distance and maximum flow rate (H=2mm, V=40 l/min).
- From the experimental validation, the stand-off distance, H, and volumetric air flow rate, V, were found to have a significant influence on the pressure distribution and lifting force generated by the Bernoulli gripper.

The model developed can be used to evaluate the lifting force and pressure distribution on the rigid and flat handled object as a function of the volumetric air flow rate and stand-off distance. When handling thin brittle wafers for example, the output of this model can be used as an input to a wafer deformation/stress model to calculate the wafer handling stresses generated by the gripper.

6.2.2 Effect of Substrate Flexibility on the Air Pressure and Handling Stresses

Modeling and analysis of the effect of substrate flexibility, and hence deformation, on the equilibrium pressure distribution and handling force generated by a Bernoulli gripper were developed. An iterative fluid-structure interaction model was solved using CFD and non-linear finite element analysis in order to elucidate the effect of substrate deformation. The model was analyzed and experimentally verified for Bernoulli handling of thin silicon wafers used as substrates in PV solar cell manufacture. The following specific conclusions summarize the work:

- The modeling approach is shown to yield predictions that are in good agreement with the measured equilibrium wafer deformations for both cast and EFG silicon wafers over a range of volumetric airflow rates. Specifically,

prediction errors smaller than 7% were obtained for the cast silicon wafers while a larger average error of around 15% was obtained for the EFG wafers.

- At high airflow rates with the 180 μm thick EFG wafer, the model was shown to accurately capture the leveling-off trend in the maximum wafer deformation due to the competing effects of low air pressure created by the radially diverging airflow and the direct impingement of air on the wafer surface in the vicinity of the nozzle.
- The effect of substrate/wafer flexibility on the radial air pressure distribution and lifting force was found to be significant at higher volumetric airflow rates for both wafer types. Up to 32% difference in the predicted lifting force compared to the rigid substrate solution was found for the cast wafers at 40 l/min airflow rate. For the EFG wafers, the maximum influence of wafer flexibility on the lifting force was 39% at 35 l/min. Overall the effect of wafer deformation on the air pressure is to increase the vacuum level in the center region for both wafer types. For the thinner EFG wafer, the counteracting effect of direct air impingement is significant at the higher airflow rates. A similar effect is predicted for the lifting force and handling stresses.
- The model presented here is able to predict the handling stresses as a function of the handling control variables. It is shown that the airflow rate has a significant effect on the magnitude and distribution of the handling stresses. The magnitude of the maximum in-plane principal stress at the center of the wafer increases by 5.7 times and 4.5 times when going from 30 l/min to 40 l/min airflow rate for the cast wafer and EFG wafers, respectively.

- In addition, a transition in the maximum in-plane principal tensile stress location from the center to the wafer edge is predicted by the model with increase in the air flow rate.

The results obtained from this model can be used to evaluate the lifting force acting on any air impermeable flexible substrate as a function of the gripper variables such as the volumetric airflow rate and stand-off distance. Also, optimization of the gripper design and more particularly the location of the rubber pads can be carried out to minimize the wafer deformation and consequently the handling stresses when handling thin brittle materials such as silicon wafers. This optimization can help to reduce incidents of wafer breakage during handling operations.

6.2.3 Analysis of the Total Stress State and Breakage of Crystalline Silicon Wafers during Handling

A systematic approach for the analysis of the total stress state produced in sc-Si and mc-Si wafers during handling and the relationship to wafer breakage has been presented. The approach relies on a combination of full-field wafer deformation measurements and non-linear finite element analysis to determine the total stress state in the wafer/cell during handling Although the focus was on a specific wafer handling method, namely Bernoulli gripping, the overall approach is general and applicable to all handling devices that induce wafer deformation and consequently stresses. The specific conclusions are as follows:

- It is shown that the air flow rate, wafer type and thickness have a significant effect on the magnitude and distribution of the handling stresses. For all wafer types, results showed a transition in the maximum in-plane principal tensile

stress location from the center to the wafer edge as the air flow rate is increased.

- Based on knowledge of the total stress state and crack size and location, an approach to determine the breakage stress was presented. The results showed that the proposed approach yields breakage stress values that are consistent with linear elastic fracture mechanics theory. The experimental results also show that the wafer breakage stress determined using the approach is proportional to the inverse square root of the crack length as expected from linear elastic fracture mechanics, hence validating the in-plane tensile stress calculation.
- Critical crack sizes can be estimated from the breakage analysis presented in this thesis. For given handling control variables, breakage free handling can be realized by sorting out wafers with crack sizes larger than the critical crack size.

The results obtain from this work confirm the capability of predicting wafer breakage during handling using the total stress state provided the crack size, location and fracture toughness are known.

6.3 Further Investigations

Related areas for further research include the following:

- Prediction of the handling stresses generated by other handling devices from handling control variables is needed. This will allow comparison of different handling technologies.
- In the case of Bernoulli handling, using the tools developed in this work, the actual geometry of the gripper and handling variables could be optimized for a specific wafer size and type, and knowledge of structural defects (crack size, preferred location, density).
- Knowledge of the complete residual stress state in the wafer is needed to obtain the total stress state in the wafer. This will enable a first principle approach to the prediction of the total stress state, and therefore breakage, by superposing the handling stress distribution predicted by the iterative procedure developed in this thesis on the residual stress state.

REFERENCES

[1] J. Kalejs, M. Schroth, M. and S. Danyluk. A National Photovoltaic Industry Assessment for the USA: Needs, Corporate Structure and Building Blocks, *Proceedings of the 4th IEEE World Conf. on Photovoltaic Energy Conversion*, May 7-12, Waikoloa, HI, USA, 2:2520-2523, 2006.

[2] H.J. Moller, C. Funke, M. Rinio, and S. Scholz. Multicrystalline Silicon For Solar Cells, *Thin Solid Films*, 487(1-2):179-87, 2005..

[3] National Solar Technology Roadmap: Wafer-Silicon PV, http://www1.eere.energy.gov/solar/solar_america/pdfs/41733.pdf, August 29, 2008.

[4] P.S. Dominguez and J.M. Fernandez. Introduction of Thinner Monocrystalline Silicon Wafers in an Industrial Cell-Manufacturing Facility, *Proceedings of the 19th European Photovoltaic Solar Energy Conference*, Paris, France, 2004.

[5] L.E. Teschler. Next Big Challenge for PV Makers: Wafer Handling, *Machine Design*, July 8, 2008.

[6] R. Kolluru, K.P. Valavanis, S.S. Smith and N. Tsourveloudis. An overview of the University of Louisiana robotic gripper system project. *Transactions of the Institute of Measurement and Control*, 24(1):65-84, 2002.

[7] R. Kolluru, K.P. Valavanis, S.S. Smith and N. Tsourveloudis. Design fundamentals of a reconfigurable robotic gripper system. *IEEE Transactions on Systems, Man, and Cybernetics Part A: Systems and Humans.*, 30(2):181-187, 2000.

[8] B. Ozcelik and F. Erzincanli. A non-contact end-effector for the handling of garments. *Robotica*, 20(4):447-450, 2002.

[9] B. Ozcelik and F. Erzincanli. Examination of the movement of a woven fabric in the horizontal direction using a non-contact end-effector. *International Journal of Advanced Manufacturing Technology*, 25(5-6):527-532, 2005.

[10] G. Seliger and J. Stephan. Flexible garment handling with adaptive control strategies, *Proceedings of the 29th ISR, Birmingham*, United-Kingdom, pages 483-487, 1998.

[11] G. Seliger, F Szimmat, J Niemeier and J Stephan. Automated handling of non-rigid parts. *CIRP Annals - Manufacturing Technology*, 52(1):21-24, 2003.

[12] J.A. Paivanas and J.K. Hassan. Air film system for handling semiconductor wafers. *IBM Journal of Research and Development*, 23(4):361-75, 1979.

[13] D.P. Baumann. Touchless wafer handling. *Solid State Technology*, 16(3):45-49, 1973.

[14] B. Musits and R. Wernikowski. Wafer handling system. *IBM Technical Disclosure Bulletin*, 17(10):2904, 1975.

[15] A.F. Johnson. Jr., Contamination-free wafer handling and identification. *Western Electric Engineer*, 20(2):42-49, 1976.

[16] J.K. Hassan and J.A. Paivanas. Minimum cost concept for contactless air film handling of wafer sizes larger than 3-1/4 inches [8.25 cm]. *IBM Technical Disclosure Bulletin*, 22(4):1474-5, 1979.

[17] J.A. Paivanas and J.K. Hassan. Attraction force characteristics engendered by bounded, radially diverging air flow. *IBM Journal of Research and Development*, 25(2-3):176-86, 1981.

[18] H. Tokisue and K. Matsuoka. Development of non-contact handling system for semiconductor wafers. *Proceedings of IEEE/CHMT IEMT Symposium*, Nara, Japan, pages 246-249, 1989.

[19] A.S. Koh, R. Ford, and T. Seshadri. Wafer handling with levitation. *Journal of Electronics Manufacturing*, 2(3):101-7, 1992.

[20] H. Tokisue and H. Inoue. Particulate-contamination-free wafer-handling systems for gas, liquid and vacuum environments used in a 64 Mbyte dynamic random-access memory process. *Wear*, 168(1-2):115-120, 1993.

[21] K. Asano, F. Hatakeyama, and K. Yatsuzuka. Fundamental study of an electrostatic chuck for silicon wafer handling. *Conference record of IEEE Industry Applications Conference*, New Orleans, LA, USA, 3:1998-2003, 1997.

[22] K. Asano, F. Hatakeyama, and K. Yatsuzuka. Fundamental study of an electrostatic chuck for silicon wafer handling. *Conference record of IEEE Transactions on Industry Applications*, 38(3):840-5, 2002.

[23] K. Yatsuzuka, F. Hatakeyama, K. Asano and S. Aonuma. Fundamental characteristics of electrostatic wafer chuck with insulating sealant. *IEEE Transactions on Industry Applications*, 36(2):510-516, 2000.

[24] F.A.T. Schraub. Automated handling of ultra-thin silicon wafers. *Solid State Technology*, 45(9):59-60, 2002.

[25] R. Wilson, H.S. Gamble, and A.S. Hudson. Novel technique for the production of thin devices. *Microelectronic Engineering*, 19(1-4):157-160, 1992.

[26] S. Pinel, J. Tasselli, J.P. Bailb, A. Marty; P. Puech and D. Estve. Mechanical lapping, handling and transfer of ultra-thin wafers. *Journal of Micromechanics and Microengineering,* 8(4):338-342, 1998.

[27] A. Singh, D.A. Horsley, M.B. Cohn, A.P. Pisano and R.T. Howe. Batch transfer of microstructures using flip-chip solder bonding. *Journal of Microelectromechanical Systems*, 8(1):27-33, 1999.

[28] T. Suga, M.M.R. Howlader, T. Itoh, C. Inaka, Y. Arai and A. Yamauchi. A new wafer-bonder of ultra-high precision using surface activated bonding (SAB) concept. *Proceedings of the IEEE ECTC*, Orlando, FL, USA, pages 1013-1018, 2001.

[29] J. Bagdahn, H. Knoll M. Wiemer, M. Petzold. A new approach for handling and transferring of thin semiconductor materials. *Microsystem Technologies*, 9(3):204-9, 2003.

[30] V. Dragoi, C. Schaefer, P. Lindner, M. Wimplinger and S. Farrens. Temporary bonding technology improves thin wafer handling. *Solid State Technology*, 47(3):61-62, 2004.

[31] A. Binder and G. Kroupa. Novel technology for handling very thin wafers. *Solid State Technology*, 46(10):64-66, 2003.

[32] M. Matschitsch, et al., Bernoulli and vacuum combined gripper. *European Patent*, EP1091389, 2001.

[33] J.M. Benjamin and N.J. Brick Town. Pneumatic probe for handling flat objects. *US Patent*, 3425736, 1969.

[34] W.K. Mammel. Pickup device for supporting workpieces on a layer of fluid. *US Patent*, 3431009, 1969.

[35] A.R. Safabakhsh. Non-contact pick-up head. *US Patent*, US5169196, 1992.

[36] L. Kiesewetter and H. Grutzeck. Downscaling of grippers for micro assembly. *Microsystem Technologies*, 8(1):27-31, 2002.

[37] F. Erzincanli, J.M. Sharp, and S. Erhal. Design and operational considerations of a non-contact robotic handling system for non-rigid materials. *International Journal of Machine Tools & Manufacture*, 38(4):353-361, 1998.

[38] F. Erzincanli and J.M. Sharp. Development of a non-contact end effector for robotic handling of non-rigid materials. *Robotica*,15(3):331-335, 1997.

[39] B. Ozcelik, F. Erzincanli, and F. Findik. Evaluation of handling results of various materials using a non-contact end-effector. *Industrial Robot*, 30(4):363-369, 2003.

[40] S. He. Near-Infrared photoelasticity of polycrystalline silicon and its relation to in-plane residual stresses. Ph.D. Thesis. *Georgia Institute of Technology*. 2005.

[41] M.H. Leipold and C.P. Chen. Fracture behavior in silicon. *Proceeding of the 5th E.C. Photovoltaic Energy Conference*, Kavouri, Greece, pages 1014-1018, 1983.

[42] Cook, R.F., Strength and sharp contact fracture of silicon. *Journal of Materials Science*, 41(3):841-872, 2006.

[43] S.M. Hu. Critical stress in silicon brittle fracture, and effect of ion implantation and other surface treatments. *Journal of Applied Physics*, 53(5):3576-80, 1982.

[44] J.C. McLaughlin and A.F.W. Willoughby. Fracture of silicon wafers. *Journal of Crystal Growth*, 85(1-2):83-90, 1987.

[45] S.-M. Jeong, S.-E. Park, H.-S. Oh and H.-L. Lee. Evaluation of damage on silicon wafers using the angle lapping method and a biaxial fracture strength test. *Journal of Ceramic Processing Research*, 5(2):171-174, 2004.

[46] K. McGuire, S. Danyluk, T.L. Baker, J.W. Rupnow and D. McLaughlin. The influence of backgrinding on the fracture strength of 100 mm diameter (111) p-type silicon wafers. *Journal of Materials Science*, 32(4): 1017-24, 1997.

[47] W. Weibull. A theory of fatigue crack propagation in sheet specimens. *Acta Metallurgica*, 11:745-752, 1963.

[48] D.Y.R. Chong, W.E. Lee, J.H.L. Pang, T.H. Low and B.K. Lim. Mechanical failure strength characterization of silicon dice. *Proceedings of the IEEE EPTC*, Singapore pages 600-605, 2003.

[49] C.P. Chen and M.H. Leipold. Fracture strength of GaAs solar cells as a function of manufacturing process steps. *Proceedings of the IEEE Photovoltaic Specialist Conference*, Las Vegas, NV, USA, pages 310-316, 1985.

[50] C. Funke, E. Kullig, M. Kuna, H.J. Moller. Biaxial fracture test of silicon wafers. *Advanced Engineering Materials*, 6(7):594-598, 2004.

[51] G. Coletti, C.J.J. Tool, and L.J. Geerligs. Mechanical strength of silicon wafers and its modelling. *Proceeding of the 15th NREL Workshop on Crystalline Silicon Solar Cells & Modules*, Vail, CO, USA, 2005.

[52] P.A. Wang. Industrial Challenges For Thin Wafer Manufacturing. *Proceedings of the 4th IEEE World Conference on Photovoltaic Energy Conversion*, Waikoloa, HI, USA,1:1179-1182, 2006.

[53] C.C. Chao, R. Chleboski, E.J. Henderson, C.K. Holmes, and J.P. Kalejs. Fracture Behavior of silicon cut with high power laser, *Mat. Res. Soc. Symp. Proc*., 226:363-368, 1991.

[54] H. Behnken, M. Apel, and D. Franke. Simulation of mechanical stress during bending tests for crystalline wafers. *Proceedings of the 3rd IEEE World Conference on Photovoltaic Energy Conversion*, Osaka, Japan, 2:1308-1311 2003.

[55] X.K. Sun, X.J. Xin, and Z.J. Pei. Finite element analysis of die-strength testing configurations for thin wafers. *Journal of Electronic Packaging*, Transactions of the ASME, 127(2):189-192, 2005.

[56] B. Cotterell, Z. Chen, J.-B. Han and N.-X. Tan. The strength of the silicon die in flip-chip assemblies. *Journal of Electronic Packaging*, Transactions of the ASME, 125(1):114-119, 2003.

[57] C. Bohm, T. Hauck, A. Juritza and W.H. Muller. Weibull statistics of silicon die fracture. *Proceedings of the IEEE EPTC*, Singapore, pages 782-786, 2004.

[58] P.S. Raghavan, Y. Wan, and C.P. Khattak. Crack Detection in Photovoltaic Quality Control, *Proceedings of the 16th NREL Workshop on Crystalline Silicon Solar Cells and Modules*, Denver, CO, pages 125-128, 2006.

[59] T. Trupke, R.A. Bardos, M.D. Abbott, F.W. Chen, J.E. Cotter, and A. Lorenz. Fast Photoluminescence Imaging of Silicon Wafers. *Proceedings of the 4th IEEE World Conference on Photovoltaic Energy Conversion*, Waikoloa, HI, 1:928-931, 2006.

[60] S. Ostapenko, W. Dallas, D. Hess, O. Polupan, and J. Wohlgemuth. Crack Detection and Analysis Using Resonance Ultrasonic Vibrations in Crystalline Silicon Wafers, *Proceedings of the 4th IEEE World Conference on Photovoltaic Energy Conversion*, Waikoloa, HI, USA, 1:920-923, 2006.

[61] I. D. Vrinceanu. Analysis of the Residual Streses in Silicon Wafers using Shadow Moiré Technique. Ph.D. Thesis. *Georgia Institute of Technology*. 2002.

[62] J.F. Nye. Physical Properties of Crystals. *Oxford University Press*, London, United Kingdom, 1957.

[63] R. Hull. Properties of Crystalline Silicon. *INSPEC*, EMIS Datareviews Series No. 20, London, United Kingdom, 1999.

[64] J.J. Wortman and R.A. Evans. Young's Modulus, Shear Modulus, and Poisson's Ration in Silicon and Germanium, *Journal of Applied Physics*, 36(1):153-156, 1965.

[65] J. Turley and G. Sines. The anisotropy of Young's modulus, shear modulus and Poisson's ration in cubic materials, *Journal of Physics D: Applied Physics*, 4:264-271, 1971.

[66] K.V. Ravi. The Growth of EFG Silicon Ribbons, *Journal of Crystal Growth*, 39:1-16, 1977.

[67] X.F. Brun and S.N. Melkote. Evaluation of Handling Stresses Applied to EFG Silicon Wafer Using a Bernoulli Gripper, *Proceedings of the 4th IEEE World Conference on Photovoltaic Energy Conversion, IEEE*, 2:1346-1349, 2006.

[68] J. Blazek. Computational Fluid Dynamics: Principles and Applications, Elsevier Science, 2001.

[69] M.M. Gibson and B.E. Launder. Ground Effects on Pressure Fluctuations in the Atmospheric Boundary Layer, *Journal of Fluid Mechanics*, 86(3):491–511, 1978.

[70] B.E. Launder. Second-Moment Closure: Present .... and Future?, *International Journal of Heat and Fluid Flow*, 10(4):282–300, 1989.

[71] B.E. Launder, G.J. Reece, and W. Rodi. Progress in the Development of a Reynolds-Stress Turbulence Closure, *Journal of Fluid Mechanics*, 68(3):537–566, 1975.

[72] FLUENT, User's Guide, Version 6.2, *Fluent Inc*., 2005.

[73] X.F. Brun and S.N. Melkote. Modeling and Prediction of the Flow, Pressure and Holding Force Generated by a Bernoulli Handling Device, *Proceedings of the ASME MSEC*, Evanston, IL, USA, 2008.

[74] B. Sopori, P. Sheldon, and P. Rupnowski. Wafer Breakage Mechanism(s) and a Method for Screening "Problem Wafers", *Proceedings of the 16th NREL Workshop on Crystalline Silicon Solar Cells and Modules*, Denver, CO, pages 129-138, 2006.

[75] S. He, T. Zheng, and S. Danyluk. Analysis and Determination of the Stress-Optic Coefficients of Thin Single Crystal Silicon Samples, *Journal of Applied Physics*, 96(6):3103-3109, 2004.

[76] F. Li, V. Garcia, and S. Danyluk, Full Field Stress Measurements In Thin Silicon Sheet, *Proceedings of the 4th IEEE World Conference on Photovoltaic Energy Conversion*, Waikoloa, HI, 1:1245-1248, 2006.

[77] H. Tada, P.C. Paris and G.R. Irwin, G.R. The Stress Analysis of Cracks Handbook, *ASME Press*, New York, pages 52-53, 2000.

[78] C.P. Chen and M.H. Leipold. Fracture Toughness of Silicon, *Am. Ceram. Bull*., 59:469-472, 1980.

[79] F. Ebrahimi and L. Kalwani. Fracture Anisotropy in Silicon Single Crystal, 268(1): 116-126, 1999.

[80] K. B. Broberg. Cracks and Fracture, *Academic Press*, 1999.